Universitat
de les Illes Balears

Doctoral Thesis

Study on the general applicability of the collector efficiency model to solar process heat collectors

Julian David Hertel

2019

Universitat
de les Illes Balears

Doctoral Thesis

Study on the general applicability of the collector efficiency model to solar process heat collectors

Julian David Hertel

2019

Doctoral program in physics

Supervisors:

Dr. Víctor Martínez Moll

Dr. Ramón Pujol Nadal

Tutors:

Dr. Eduard Cesari Aliberch

Declaration

I hereby declare that except where specific reference is made to the work of others, the contents of this dissertation are original and have not been submitted in whole or in part for consideration for any other degree or qualification in this, or any other University. This dissertation is the result of my own work and includes nothing which is the outcome of work done in collaboration, except where specifically indicated in the text.

Place, Date	Julian Hertel
Víctor Martínez Moll	Ramón Pujol Nadal

Acknowledgements

Firstly, I would like to express my sincere gratitude to my advisors Prof. Víctor Martínez Moll and Prof. Ramon Pujol Nadal for their continuous support of my PhD study and related research, for their patience, motivation, and immense knowledge. Their guidance helped me in all the time of research and writing of this thesis. I could not have imagined having better advisors and mentors for my PhD study.

To the rest of our research group, including Dr. Andreu Moiá Pol, Dr. Vicente Canals Guinand and Francesc Bonnín Ripoll, for their collaborative support.

My sincere thanks also go to Dr. Ulrike Jordan and Dr. Klaus Vajen from the University of Kassel for coordinating the SHINE project. Assuming responsibility and taking charge of all the paperwork can be very tedious and is usually not appreciated enough.

To Prof. Matthias Rommel, Dr. Mercedes Rittmann-Frank and Dr. Bastian Schmitt, thank you for coordinating our regular Work Package meetings and for helping out with our dissemination tasks.

Talking of Work Package Two I want to sincerely thank my SHINE PhD colleagues Jana and Steve for the mutual support of each other's research and our time together.

To all the other SHINE PhD students, including Nico, Federico Bava, Federico Leonardi, Artem, Alireza, Yoann, Simione, Martin, Boa Nam and Kristijan, thank you for the collaborative support and the good moments we shared.

Of course, I would also like to thank my family: my parents and to my brothers for supporting me spiritually throughout writing this thesis and my life in general.

It should also be mentioned that this thesis emerged within the framework of the SHINE project, an international PhD education program and network gratefully funded by the European Union (call FP7-PEOPLE-2012-ITN, grant number 317085). This study was further be supported by the Spanish Ministry of Economy and Competitiveness (MINECO) as well as the European Funds for Regional Development (ERDF) (ENE2015-68339-R)

Abstract

According to several studies, the installed capacity of solar thermal collectors to provide heat for industrial processes is going to increase significantly during the next decades. The great variety of designs and large range of operating temperatures of solar process collectors make their performance assessment challenging. Although the quasi-dynamic testing procedure has been designed for most types of collectors, it shows limitations or vagueness when dealing with medium-scaled collectors. This thesis analyzes some limitations, focusing mainly on the optical efficiency assessment.

A powerful ray-tracing algorithm has been developed for the optical analyses in this thesis. The algorithm was used to carry out a sensitivity analysis of a Fresnel collector to achieve a better understanding of the most influential parameters in ray-tracing simulations. Two observations were made: First, spectral simulations are not relevant for solar thermal applications unless mirror scattering shows a very high dependency on the wavelength. Second, defining the incidence angle dependency of optical materials is crucial to produce accurate results.

In the case of biaxial concentrating collectors, the incidence angle modifier factorization model is commonly applied. This model inherently introduces errors by factorizing the underlying non-factorizable functions. The error was characterized for four different collector geometries by comparing factorization with ray-tracing simulations. Results have been presented as a function of geographical latitude. Factorization in the θ_i-θ_T-space performed best in nearly all cases.

Four different collector geometries were submitted to ray-tracing simulations in order to analyze the thermal dependency of the factorization error. It is shown that the relative error generally increases with higher operating temperatures, but within the economically viable temperature range it stays fairly constant. With higher temperatures the collector gradually stops operating beginning with moments when sun angles are least favorable for factorization.

Resum

Segons diversos estudis, la capacitat instal·lada de captadors solars tèrmics pel subministrament de calor en processos industrials s'incrementarà significativament en els propers anys. La gran diversitat de dissenys i temperatures de treball d'aquest tipus de captador fa difícil l'avaluació dels seus rendiments. Encara que el mètode experimental quasi dinàmic s'ha desenvolupat per la major part de models de captador, segueix tenint limitacions o imprecisions a l'hora d'avaluar captadors específics per calor de procés. Aquesta tesi analitza algunes d'aquestes limitacions, centrant-se principalment en l'avaluació de l'eficiència òptica.

Per l'anàlisi òptica, en aquesta tesi s'ha desenvolupat un algoritme avançat de ray-tracing. L'algoritme ha servit per realitzar una anàlisi de sensibilitat d'un captador Fresnel, que ha permès conèixer quins son els paràmetres que tenen una major influència en la qualitat dels resultats obtinguts en les simulacions de ray-tracing. S'ha arribat a dues conclusions: En primer lloc, simulacions espectrals no son rellevants per aplicacions solars tèrmiques, a no ser que la dispersió del mirall depengui significativament de la longitud d'ona. En segon llos és imprescindible especificar al dependència de l'angle d'incidència dels materials òptics per generar resultats acurats.

En el cas de captadors concentradors biaxials, s'aplica el model de factorització del modificador d'angle d'incidència. Aquesta factorització te sempre associat un cert error, ja que l'IAM no és en general factoritzable. S'ha caracteritzat l'error per quatre geometries de captadors diferents, comparant el models de factorització amb les simulacions ray-tracing. Els resultats s'han presentat en funció de la latitud geogràfica. La factorització a l'espai θ_i-θ_T es la que ofereix més bons resultats en gairebé tots els casos analitzats.

Quatre geometries diferents de captador foren analitzades per determinar la dependència amb la temperatura de l'error de factorització. S'ha demostrat que a mesura que s'incrementa la temperatura de treball, s'incrementa l'error relatiu del la factorització, malgrat això, dins del rang de temperatures econòmicament viables, l'error es manté constant. Això és degut a que a mesura s'incrementa la temperatura, es redueixen les hores de treball, i per tant també les hores on el captador treballa sota els angles més desfavorables per la factorització.

Resumen

Según varios estudios, la capacidad instalada de captadores solares térmicos para proveer calor en procesos industriales se va a incrementar significativamente a lo largo de las próximas décadas. La gran variedad de diseños y temperaturas de este tipo de captadores hace complicada la evaluación de sus rendimientos. Aunque el métdodo experimental quasi-dinámico ha sido diseñado para la mayoría de modelos de captadores, sigue teniendo limitaciones o imprecisiones a la hora de evaluar captadores de mediana escala. Esta tesis analiza algunas de dichas limitaciones, centrándose principalmente en la evaluación de la eficiencia óptica.

Para el análisis óptico en esta tesis se ha desarrollado un algoritmo avanzado de ray-tracing. El algoritmo ha servido para realizar un análisis de sensibilidad de un captador Fresnel, para conseguir con ello un mayor conocimiento de los parámetros más influyentes en las simulaciones ray-tracing. Se ha llegado a dos conclusiones: En primer lugar, simulaciones espectrales no son relevantes para aplicaciones solares térmicas, a no ser que la dispersión del espejo dependa significativamente de la longitud de onda. En segundo lugar, es imprescindible especificar la dependencia del ángulo de incidencia de los materiales ópticos para generar resultados precisos.

En el caso de captadores concentradores biaxiales, se aplica el modelo de factorización del 'incidence angle modifier'. Por defecto, este modelo introduce errores factorizando funciones que no son factorizables. Se ha caracterizado el error para cuatro geometrías de captadores diferentes comparando el modelo de factorización con las simulaciones ray-tracing. Los resultados han sido presentados como función de la latitud geográfica. La factorización en el espacio θ_i-θ_T ha demostrado los mejores resultados para casi todos los casos.

Cuatro geometrías diferentes fueron sometidas a simulaciones de ray-tracing para analizar la dependencia térmica del mismo error de factorización. Se ha demostrado que a medida que aumenta la temperatura del proceso, aumenta también el error relativo de factorización, sin embargo, dentro del rango económicamente viable de temperaturas, el error se mantiene constante. Esto se debe a que a medida se incrementa la temperatura, el captador deja de operar primero en los momentos de ángulos más desfavorables para la factorización.

Table of contents

List of figures

List of tables

Published articles

Peer-reviewed

[1] J. D. Hertel, F. Bonnín-Ripoll, V. Martinez-Moll, and R. Pujol-Nadal, "Incidence-Angle and Wavelength-Resolved Ray-Tracing Simulations of a Linear Fresnel Collector Using the In-House Software OTSUN," Solar Energy Engineering **140**, 034502 (2018).

[2] J. D. Hertel, V. Martínez-Moll, and R. Pujol-Nadal, "Influence of thermal losses on the incidence angle modifier factorization approach," Solar Energy **135**, 50–58 (2016).

[3] J. D. Hertel, V. Martínez-Moll, and R. Pujol-Nadal, "Estimation of the Influence of Different Incidence Angle Modifier Models on the Biaxial Factorization Approach," Energy Conversion and Management **106**, 249–259 (2015).

Conferences

[1] T. Osório, P. Horta, M. Larcher, R. Pujol-Nada, J. Hertel, and D. W. Van Rooyen, "Ray-tracing software comparison for linear focusing solar collectors," AIP Conference Proceedings **1734**, 020017 (2016).

[2] J. D. Hertel, V. Martínez-Moll, R. Pujol-Nadal, X. Olano-Martiarena, A. García de Jalón, and F. Sallaberry, "Comparison between the Experimental and the Extrapolated Stagnation Temperature – A Data Base Evaluation," pp. 8–12 (2015).

[3] J. D. Hertel, V. Martínez-Moll, R. Pujol-Nadal, and F. Bonnín, "State of the art of radiation-matter interaction models applied for the optical characterization of concentrating solar collectors," in "Proceedings of the EuroSun 2016 Conference," (Palma de Mallorca, 2016).

[4] R. Pujol-Nadal, V. Martínez-Moll, A. Moià-Pol, G. Cardona, J. D. Hertel, and F. Bonnin, "OTSun Project: Development of a Computational Tool for High-resolution Optical Analysis of Solar Collectors," in "Proceedings of the EuroSun 2016 Conference," (Palma de Mallorca, Spain, 2016).

[5] R. Pujol-Nadal, F. Bonnín-Ripoll, J. D. Hertel, V. Martínez-Moll, and G. Cardona, "OTSun: An Open Source Code for the Optical Analysis of Solar Thermal Collectors and PV Cells," Proceedings of the EuroSun 2018 (2018).

Nomenclature

Roman Symbols

ε_0	Permittivity of free space	$\mathrm{F/m}$
μ_0	Permeability of free space	$\mathrm{H/m}$
A	Surface absorptivity	–
a_1	Thermal loss coefficient	$\mathrm{W/(m^2\,K)}$
a_2	Temperature dependence of the heat loss coefficient	$\mathrm{W/(m^2\,K^2)}$
A_{ref}	Reference surface of the collector	$\mathrm{m^2}$
AM	Air mass	–
c_1	Heat loss coefficient	$\mathrm{W/(m^2\,K)}$
c_2	Temperature dependence of the heat loss coefficient	$\mathrm{W/(m^2\,K^2)}$
c_3	Wind speed dependence of the heat loss coefficient	$\mathrm{J/(m^3\,K)}$
c_4	Sky temperature dependence of the heat loss coefficient	–
c_5	Effective thermal capacity	$\mathrm{J/(m^2\,K)}$
c_6	Wind dependence in the zero loss efficiency	$\mathrm{s/m}$
d_r	Physical thickness of the rth layer in a thin film coating	m
d_y	Day of the year	–
E_0	Extraterrestrial irradiance	$\mathrm{W/m^2}$
E_L	Long wave irradiance	$\mathrm{W/m^2}$

f	Probability density function of scattering	–
G	Global horizontal irradiance	$\mathrm{W/m^2}$
K	Incidence Angle Modifier	–
K_σ	Weighting factor of the superposition of two Gaussian curves	–
L	Total length of the collector	m
l_{focal}	Focal length of the collector	m
N	Refractive index	–
n	Real refractive index	–
Q	Heat flux	$\mathrm{W/m^2}$
R	Surface reflectance	–
R_h	Hemispherical reflectance	–
R_s	Spectral reflectance	–
T	Surface transmittance	–
u	Wind speed	m/s
Y	Optical admittance	S
Z_0	Optical impedance of free space	Ω

Greek Symbols

α	Absorption coefficient of a medium	–
α_0	Overall collector absorptivity at normal incidence	–
η	Collector efficiency	–
η_0	Optical efficiency at normal incidence	–
η_{gain}	Heat gains of a solar collector	–
η_{loss}	Heat losses of a solar collector	–
κ	Imaginary refractive index	–

λ	Wavelength	m
λ_0	Vacuum wavelength	m
$\mathbf{e}_{1/2/3}$	Cartesian unity vectors	–
Ω	Solid angle	sr
ω	Polar grid interval	–
ϕ_L	Latitude	rad
ρ_0	Overall collector reflectance at normal incidence	–
σ	Variance of scattering function	mrad
σ_ϕ	Equivalent-roughness of reflective surface	m
σ_B	Stefan-Boltzmann constant	$\mathrm{W/m^2\,K^4}$
τ_0	Overall collector transmittance at normal incidence	–
θ	Solar incidence angle on the collector aperture	rad
θ_i	Angle between the sun vector and the transversal plane of the collector	rad
θ_L	Longitudinal angle	rad
θ_S	Zenith angle of the sun	rad
θ_T	Transversal angle	rad
φ	Scattering angle	rad
φ_r	Phase factor	–
φ_S	Azimuth angle of the sun	rad
ϑ_a	Ambient temperature	°C
ϑ_m	Mean temperature of the collector	°C
F'	Heat removal factor	–
K_σ	Superposition factor	–
M_p	Characteristic matrix of a thin-film assembly	–

Subscripts

$\parallel$	With respect to p-polarized radiation
$\perp$	With respect to s-polarized radiation
b	Beam radiation
d	Diffuse radiation
n	With normal incidence on plane
T	On tilted plane

Acronyms / Abbreviations

AR	Antireflection
BRDF	Bidirectional Reflectance Distribution Function
CAD	Computer Aided Design
CCD	Charge-Coupled Device
COSY	Coordinate system
CPC	Compound Parabolic Collector
CR	Concentration Ratio
CSR	Circumsolar Ratio
DNI	Direct Normal Irradiance
DT	Dynamic Testing
ETC	Evacuated Tube Collector
FMSC	Fixed Mirror Solar Collector
FPC	Flat Plate Collector
GHI	Global Horizontal Irradiance
HR	High-Reflectance
IAM	Incidence Angle Modifier

IEA International Energy Agency

IR Infrared radiation

IWEC International Weather for Energy Calculations

LFC Linear Fresnel Collector

MLR Multiple Linear Regression

PDF Probability Density Function

PTC Parabolic Trough Collector

PV Photovoltaic

PVT Photovoltaic Thermal Collector

QDT Quasi-Dynamic Testing

SST Steady State Testing

ST Solar Thermal

SWEC Spanish Weather for Energy Calculations

TIS Total Integrated Scattering

TMY Typical Meteorological Year

WLS Weighted Least Square fit

Chapter 1

Introduction to solar heat for industrial processes

Solar thermal collectors convert the energy carried by electromagnetic waves of solar irradiance into usable heat by transferring it to a heat transfer fluid such as water. In the domestic sector these collectors have proved to be a mature and reliable technology to provide renewable energy for space heating and hot water supply, but they are still hardly used in the industrial sector. This section provides some arguments in favor of solar heat for industrial processes (SHIP).

1.1 What is a solar process heat collector?

In a nutshell, a solar process heat collector is a solar thermal collector which provides heat for industrial processes. Conventional collectors for domestic applications usually provide heat at about 60 °C. This heat could easily be used to run low-temperature industrial processes, making the conventional collector a process heat collector, so there does not seem to be a clear distinction between the two concepts.

One key difference with the domestic sector is that industrial processes often run at much higher temperatures, which imposes new technical challenges on collector technology. For example, at temperatures more than 100 °C the system must be either pressurized, produce direct steam, or use a thermal oil as an heat transfer fluid, but most of all, the collector needs to be designed in such a way that its heat losses are small and its efficiency still reasonably high. The latter can be achieved by better insulating conventional designs. Some examples include the CPC-EVT collector, the honeycomb collector, or the vacuum flat plate

collector. Another possibility to guarantee high efficiencies at elevated temperatures is to use small-scale concentrating technologies such as the parabolic trough collector (PTC), linear Fresnel collector (LFC), or solar dish collectors, which have already been used for a long time in the electricity sector ($\approx 400\,^{\circ}\mathrm{C}$). Apart from that, completely new collector designs are often developed to meet very specific industry demands such as limited space. In this context, it is worth mentioning the CCStaR collector as an example. The CCStaR is a concentrating collector developed at the University of the Balearic Islands (UIB), which moves the receiver along a circular trajectory to track sunlight [1]. This means that its base construction, consisting of slightly parabolically shaped mirrors, is static, allowing for straight-forward rooftop installation. Figure 1.1 illustrates typical working temperature ranges for some common solar thermal collectors [2–4].

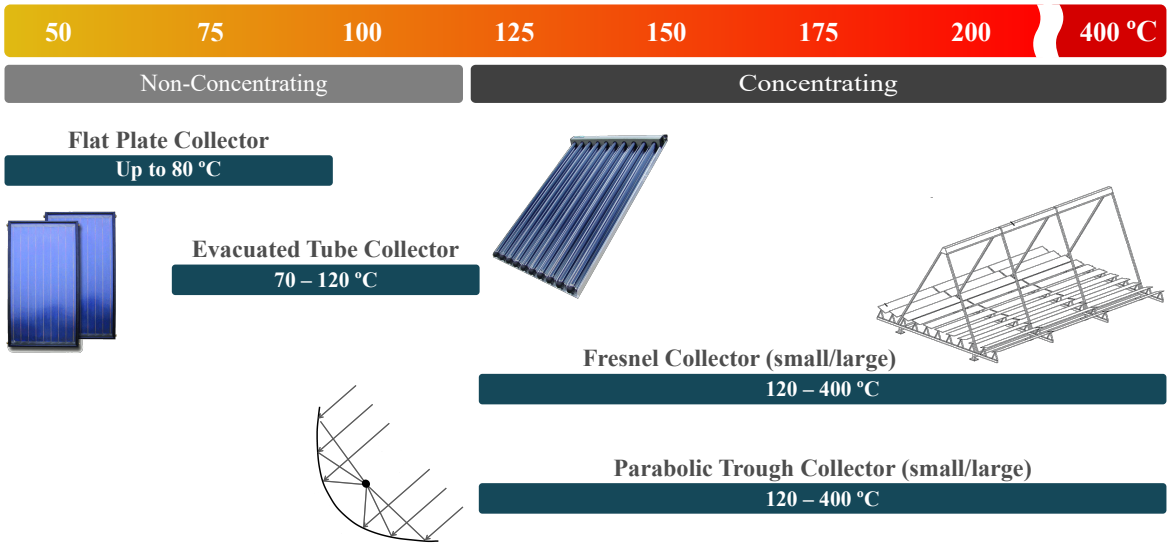

Fig. 1.1 Different collector designs and their respective operating temperature ranges.

Apparently, solar process heat collectors fill the gap between the more traditional domestic sector (low temperatures) and the electricity sector (high temperatures), which is why they are sometimes also referred to as medium-temperature collectors. As has been mentioned before, this is not entirely true, since industrial processes cover a much wider range of temperatures, including low-temperature processes, but it gives extra credit to the multiple technical challenges and designs that come into play with elevated temperature levels. As can be seen in the literature, the term "medium temperature" itself is not well defined. A summary of temperature range definitions according to different sources is found in Table 1.1.

In practice, the output temperature alone is not a reliable reference point to characterize a collector as a low, medium, or high-temperature collector. In fact, even a poorly insulated flat plate collector (FPC) can reach stagnation temperatures of above $100\,^{\circ}\mathrm{C}$. However, in this

Table 1.1 Definition of the medium-temperature range according to different sources.

References	Temperature range [°C]
Solrico [5], IRENA [6]	$150 < T < 400$
IEA [7]	$100 < T < 300$
Kalogirou [2, 8]	$80 < T < 240$
Schweiger [9]	$80 < T < 250$
Lauterbach [10], IEA Task 49 [11]	$100 < T < 250$

case, the performance of the collector would be zero. Task 49 tried to acknowledge this fact by establishing a more accurate definition, which defines medium-temperature collectors as those with an output above 300 W per square meters gross area at the following conditions [11]:

- $1000\,\mathrm{W/m^2}$ hemispherical irradiance
- 15 % diffuse fraction
- 20 °C ambient temperature
- $T > 100\,°\mathrm{C}$ (medium-temp collector), $T > 250\,°\mathrm{C}$ (high-temp collector)

In conclusion, it can be said that the term solar process heat collector does not necessarily have to relate to an elevated output temperature, but can also be interpreted as referring to the large variety of collector designs and a field that has not yet been greatly explored.

1.2 Potential and outlook

In 2014, the industry sector had the highest share of final energy consumption worldwide according to the IEA energy statistics [12]. As seen in Fig. 1.2, 74 % of this share was actually due to heat demand, which equaled a total of $85\,\mathrm{EJ/a}$. Only 9 % of this energy was provided by renewable technologies. In the framework of the solar payback project [5] it was estimated that about half (52 %) of this heat demand is required to run processes below 400 °C, for example, boiling, washing, and dyeing. Solar thermal collectors are expected to first penetrate the market in the low- and medium-temperature sector, which is why the energy share of processes at those temperatures are of particular interest.

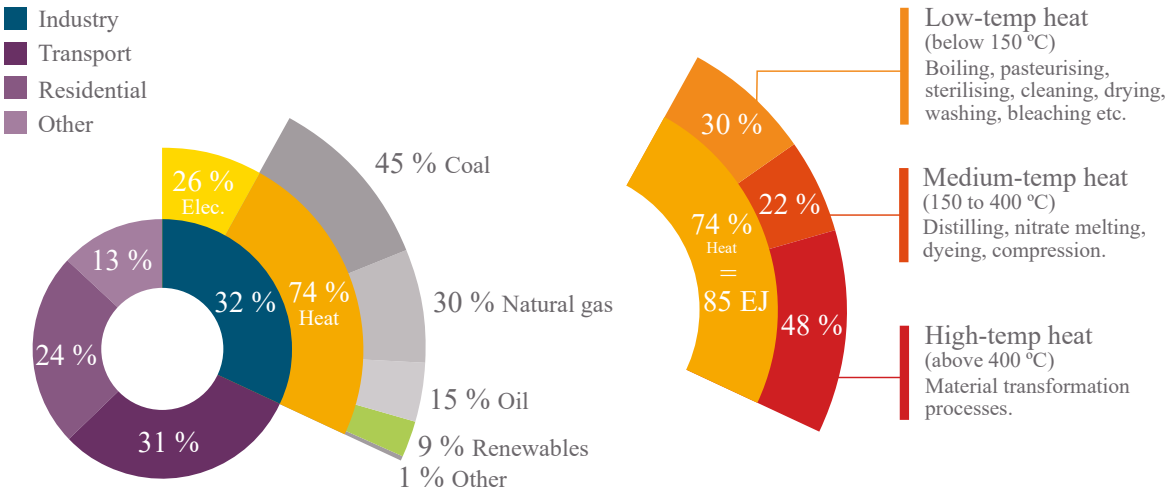

Fig. 1.2 World final energy share 2014. Adapted from Solrico [5].

In Figure 1.3, the overall heat demand share of different sectors is shown for various regions. These regions have been classified according to their economic strength. The diagrams provide an idea of the local importance of the industrial sector. Looking at the European Union countries, for example, the share of industrial heat demand is below the global average. Obviously, this is because of a comparably high share of residential heating rather than a poorly developed industrial sector. The latter would be true in the case of the African continent, which shows the lowest share of industrial heat. The highest share can be found for the non-OECD American countries, which have a developed industrial sector, but at the same time little residential heat demand due to a warmer climate.

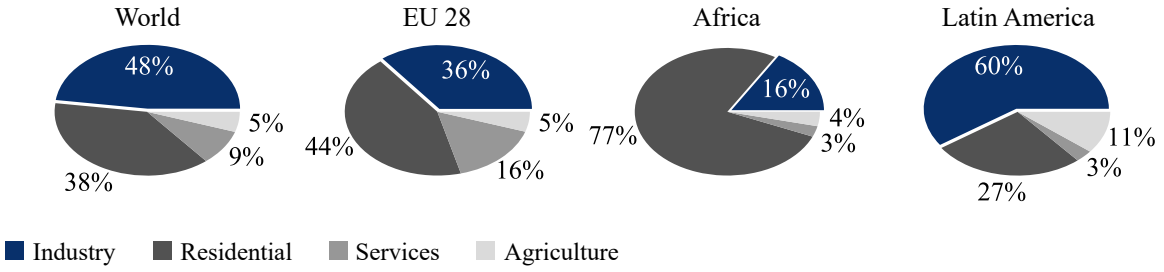

Fig. 1.3 Sectoral heat share by region. Results are based on IEA statistics from 2015 [12].

In the end, the potential for SHIP depends strongly on the industry sector. A worldwide perspective of Deger Saygin [5] has shown that the chemical and petrochemical sector and the food and beverage sector have the highest heat demands for temperatures below 400 °C (Fig. 1.4). This is followed by the machine, mining, and textile sector. In contrast, in the case of Germany, the study of Lauterbach [10] shows the highest heat demand to be in the chemical and food sectors and that the motor and vehicle industry plays a more important role than

it does on a global scale. An IEA report [7] also emphasizes the importance of a country's industry sector profile. The difference can be seen in the much more optimistic projection of SHIP development in China in comparison to India. While China has a relatively high share of low-temperature process heat, India, despite counting on plenty of solar resources, has a more pronounced high-temperature cement, iron, steel, and aluminum industry.

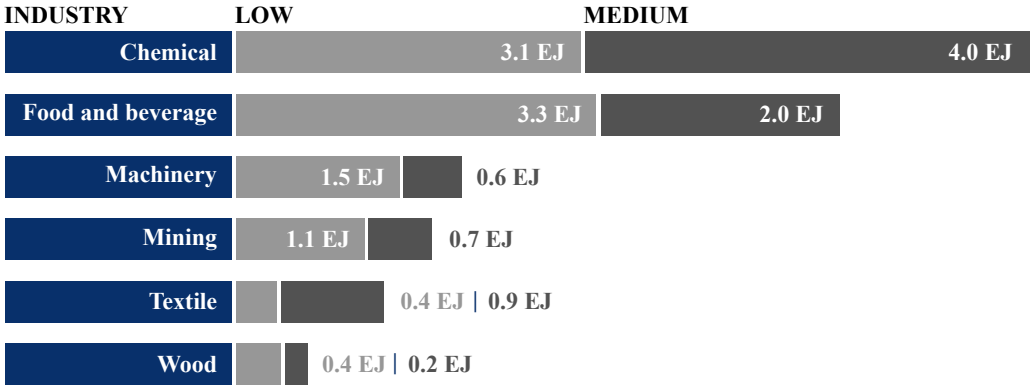

Fig. 1.4 Heat demand by industrial sector. Evaluation by Deger Saygin based on data from IEA statistics [13]. Adapted from Solrico [5].

Many studies have attempted to assess the technical potential of SHIP based on the overall heat demand and industry sector breakdown of the target region. Most of them were carried out in Europe, including Spain and Portugal [9], the Netherlands [14], Cyprus [2], Sweden [15], Austria [16], Italy [17], and Germany [10]. Results are either based on a bottom-up or top-down approach. The bottom-up approach, such as conducted by Schweiger et al. [9], consists of surveying a large number of companies and subsequently extrapolating the results. The top-down approach, such as that chosen by Müller et al. [16], attempts to draw a picture by initially filtering the official energy balance figures of the country and further reducing them by empirical factors to a technically more realistic figure. For example, Müller et al. [16] and Lauterbach [10], after discarding unsuitable sectors, applied in their calculations a factor of 0.15 for the renewable share, a factor of 0.6 to account for possible prior efficiency measures, and another solar fraction factor of 0.4, which comprises practical boundaries such as collector efficiency and available irradiance or space. The estimated technical potentials of all European studies are quite similar, as seen in Fig. 1.5.

These studies represent the foundation for the Task 49 extrapolated estimate [19], which assumed a European average of 4 % multiplied by the worldwide industrial heat demand resulting in a technical potential of 3.9 EJ/a at that time. This value is very likely to underestimate the actual technical potential for two reasons: First, unlike the European market, which mainly focuses on non-concentrating technologies, other regions might have an additional potential for concentrating collectors, in this way also providing heat for high-

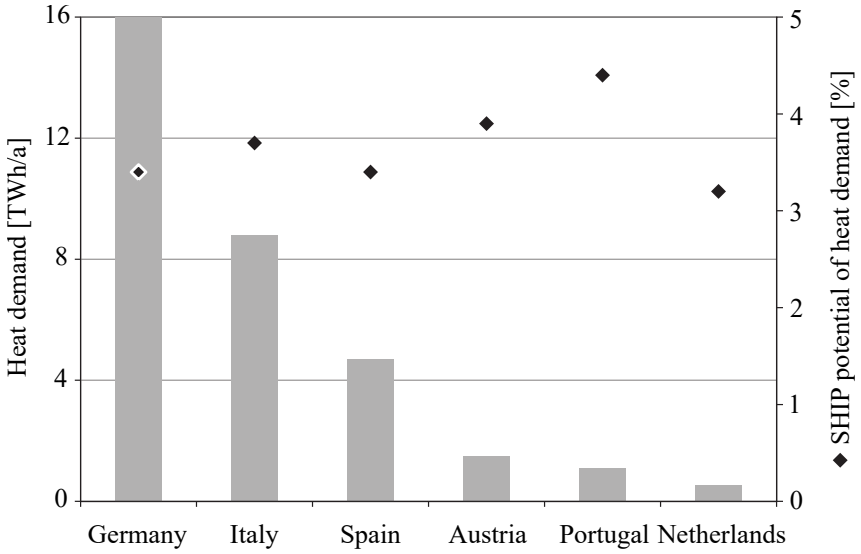

Fig. 1.5 Representative potential of SHIP for Europe. Reprinted from Lauterbach et al. [18].

temperature processes. Second, it is possible that in other countries there is more space available than in populated Europe. After all, the lack of rooftop space was the limiting factor in the study of Schweiger et al. [9]. In many cases, the lack of space might also be a deciding factor in favor of solar thermal (ST) over the rapidly developing photovoltaics (PV), since the former is able to harvest up to three times more energy per square meter [5]. Apart from the previous examples, there are some more recent studies outside Europe. Examples include Chile [20], Egypt/Pacistan/Marocco [21], and South Africa [19]

Outlook

One of the most comprehensive studies on the development of SHIP is IRENA [6]. According to this report, the industrial heat demand will increase at an annual average rate of 1.7 %, reaching 87 EJ/a by 2030[1]. Forty-nine percent of this demand is expected to be due to processes below 400 °C.

IRENA [6] predicts the realizable technical potential of SHIP to be at 14.9 EJ/a (about 850 GW_{th}) by 2030[2]. This is much higher than the estimation of Task 49 [19], but is nonetheless consistent, since 700 of the 850 GW_{th} capacity is expected to be installed in non-OECD countries [22]. More than half of the 14.9 EJ/a would be due to the chemical and petrochemical industry, a sector in which two-thirds of existing capacity will reach

[1] Without efficiency measures industrial heat demand would be 113 EJ/a by 2030.
[2] Does not take into account the realizable technical potential.

end-of-life before 2030 and which requires more than 50 % of its heat demand at low and medium temperatures.

When considering an optimistic development of the prices and learning curve of the technology as well as the competition with other renewable alternatives, the technical potential of solar process collectors decreases to a realizable economic potential of about 2.6 EJ/a in 2030[3] (Fig. 1.6). This yield could amount to 3 % of the total industrial heat demand or 9 % of renewable share in industry, with the latter potentially rising to 27 %–34 %[4]. Although the development of SHIP is admirable, it is far behind that of biomass, with a highest potential of 21.6 EJ/a. This is mainly because biomass is less complicated to integrate into existing structures and because it represents the only renewable alternative for many high-temperature applications.

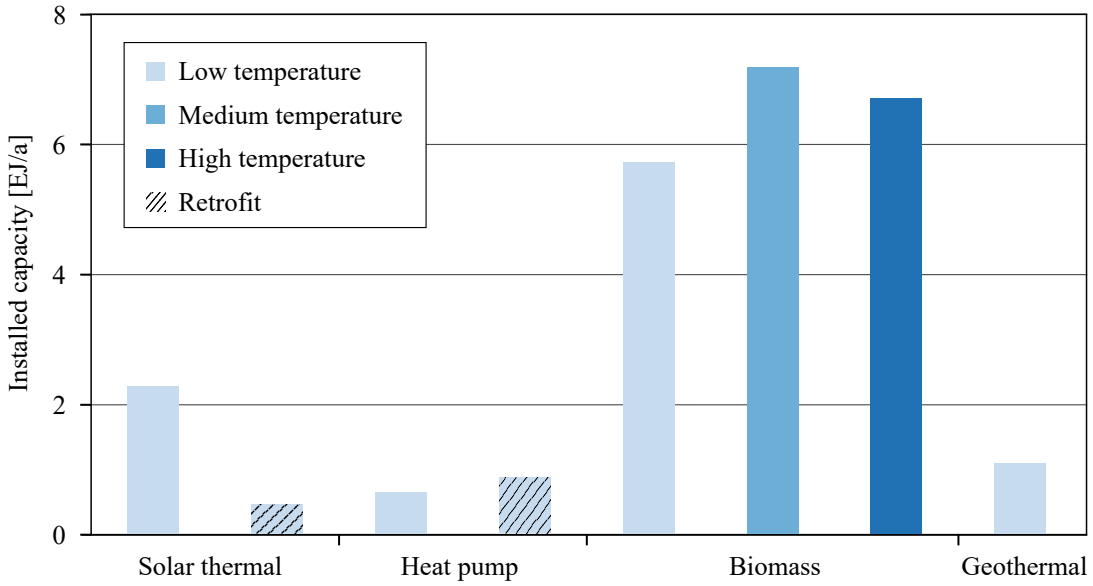

Fig. 1.6 Estimated newly installed capacity of different renewable technologies in industries by 2030. According to IRENA, the overall installed capacity could reach 28 EJ, which would represent a renewable energy share of up to 27 %–34 %. Adapted from IRENA [6].

When looking at other studies, the share of SHIP will continue to grow considerably until the year 2050. The most moderate projection by Taibi et al. [23] estimates an overall yield of 5.62 EJ/a, when the high-temperature chemical sector is omitted. The UNIDO study [24] takes Taibi's results as a reference but is more optimistic about the development of the chemical sector. The steep learning curve for concentrating technologies could raise the SHIP yield to 8 EJ/a. This would accord fairly well with the predictions of the IEA

[3] 2.3 EJ/a newly installed 0.3 EJ/a retrofitted
[4] Compared to 9 % in 2014

technology roadmap [7], which estimates an overall yield of 7.2 EJ/a by 2050. Table 1.2 gives an overview of the estimated development of SHIP according to the different studies.

Table 1.2 Estimated development of SHIP according to the different studies.

Study	Target year	Yield [EJ/a]	Area [mio m^2] [5]
IRENA [6]	2030	2.6 (2.3 + 0.3)	1505
Taibi [23]	2050	5.62	3252
UNIDO [24]	2050	8	4630
IEA [25]	2050	7.2	4167
Task 49 [19]		3.9	2257

As expected, the extrapolated results from the European projection by Task 49 seem to underestimate the potential of SHIP. Ultimately, all studies agree that most development is taking place in non-OECD countries, led by China.

1.3 Current situation and research

The assessment of the current status of SHIP worldwide is difficult, as there is no global authority for documentation. In a first attempt to report on such projects, a database targeting SHIP plants [26] all over the world was created in the framework of the IEA Task 49 [27]. The database is maintained by AEE INTEC, which also publishes regular updates on its status [28–30].

Although the database seems to constantly draw more attention, it does not give the whole picture of the solar process heat market. This has been demonstrated recently by the latest survey conducted by Solrico[6] [31] as part of the Solar Payback program [5]. In their survey they received feedback from 71 companies (manufacturers and contractors) on the number of turnkey projects they have installed to date. After matching the results with the Task 49 database they concluded that a minimum of 525 plants exists, with an area of at least 416 414 m^2 worldwide in 2017. The overall capacity of these installations is approximately 291.49 MW_{th}[7]. It can further be assumed that the overall yield could reach about 720 TJ/a, given an annual specific yield of 1200 KWh/(m^2 a) and an efficiency of 0.4

[6] Solrico is a German market research agency

[7] Assuming a conversion factor of 700 W/m^2 [29]

[19][8]. Comparing this yield with the global process heat demand of 84.82 EJ/a in 2014 [12], shows clearly that at this point the predicted potential of SHIP is nearly untapped.

Despite the fact that solar process heat is still far from being an established alternative to fossil fuels, some operating plants already prove its viability and profitability. Figure 1.7 shows some examples from the Task 49 database of how different collector technologies can provide solutions to specific problems. The SHIP plant of the copper mining company Cadelco in the Atacama Desert in Chile is the largest in the world. It uses about 43 920 m^2 of Arcon FPCs to provide heat at about 50 °C for mining processes. A 4300 m^3 storage tank makes it possible to reach a solar fraction of 80 %. The textile company Ruyi in China uses 39 300 m^2 of evacuated tube collectors (EVTs) to run low-temperature processes at around 60 °C. To reach higher temperatures of 190 °C, the Lesa dairy in Switzerland installed 115 m^2 of PTCs from NEP Solar for the pasteurization process. In South Africa, the mobile network operator Mobile Telecom Network uses 484 m^2 of LFCs from Industrial Solar, which provide heat at 185 °C, to operate an absorption chiller for the cooling network of the company.

Fig. 1.7 Different examples of SHIP plants: A flat plate collector plant for mining (Chile), an evacuated tube collector plant for the textile industry (China), parabolic trough collectors for milk processing (Switzerland) and LFCs for cooling (South Africa).

Even though the above-mentioned projects show that solar heat can be an interesting option for industry, there are still many problems to overcome in order to make the technology

[8] This is in accordance with the estimation of [30], which assumed a total yield of 0.001 EJ in 2011.

more competitive. Low market penetration is due not only to technical but also economic reasons. On the technical side there is certainly a need for further collector development and optimization. Most importantly, however, planning and installation costs have to be reduced significantly by establishing simplified and standardized solutions for the selection of the collector technology on the supply level as well as the detection of integration points and integration concepts on the process level. These were the challenges Task 49 dealt with and which resulted in the publication of updated guidelines and comprehensive deliverables [27].

On the economic side, a lack of awareness and confidence has to be tackled. For example, in the Solrico survey many solar thermal sellers reported being more successful when offering heat supply contracts or guaranteed solar yields instead of selling the technology itself. It would also be more favorable for solar thermal technologies if companies were convinced to regard the internal rate of return or the net present value respectively, rather than the payback period. The fact that companies often demand payback periods to be fewer than five years makes it even harder for solar thermal to prevail on the market. In addition, there seems to be a need for financing models from credit institutions in order to handle high investment costs. Finally, there would be a responsibility for decision makers in politics to implement environmental regulations regarding the still low fossil fuel prices, which seem to be the principle hurdle for SHIP projects.

1.4 Objectives of this thesis

This thesis focuses entirely on collector technology and does not consider system design or characteristics such as the storage dimension, load profile, or integration points. More precisely, the contributions of this work are specifically to the performance assessment of solar thermal collectors. The focus is thereby on the challenges that emerge when extending the boundaries of testing procedures to elevated output temperatures commonly found in process heat applications and when facing a great variety of collector designs. The core part of the analysis therefore is the collector model discussed in Section 2.1.1. The objectives are:

- Development of a ray-tracing program
- Identification of key parameters for ray-tracing simulations
- Comparison of incidence angle modifier (IAM) factorization models
- Influence of thermal losses on the factorization error
- Awareness raising about efficiency curve limits at higher temperatures

Chapter 1: This chapter provides a general overview of the definition, current state, and prospects of SHIPs.

Chapter 2: This chapter is short summary of the current practices in collector testing and characterization. The theoretical framework is defined by presenting the underlying terminology and explaining the fundamental equations of collector testing and yield predictions.

Chapter 3: This chapter describes the further development of the in-house ray-tracing program OTSun. Monte Carlo ray-tracing algorithms are a common tool for determining the optical efficiency of a collector. Many new models have been implemented in the existing code, as common open source programs were lacking essential features required to carry out the studies presented in Sections 4 to 6.

Chapter 4: The study presented in this chapter makes use of the ray-tracing program of Chapter 3. A sensitivity analysis is carried out to analyze the inaccuracies introduced by modeling the performance of an exemplary LFC with constant optical input parameters, rather than their surface-quality-dependent, wavelength-dependent, and angle-dependent properties

Chapter 5: The study presented in this chapter characterizes the error that is introduced by factorization of a biaxial IAM. The error is determined by comparing the IAM based on ray-tracing with the IAM based on factorization. Results are presented in a practically relevant way, showing the error as a function of latitude.

Chapter 6: This study builds on that presented in Chapter 5. Chapter 5 assesses the optical error introduced by the factorization approximation, while Chapter 6 also takes into account the influence of operating temperature. It is examined how larger thermal losses due to higher operating might possibly amplify the optical error.

Chapter 7: This chapter covers the only study of this thesis that is not related to optical simulations. It rather considers the thermal part of the efficiency equations. The evaluation of the data bases of two well-known testing laboratories provides a first clue about extrapolation errors in the high-temperature region of a collector's efficiency curve.

Chapter 2

Collector performance assessment

The previous chapter showed that the process heat sector has to deal with two characteristic phenomena which cannot be found in the domestic sector: First, process heat collectors come in a great variety of new and often complex collector designs, including both concentrating or non-concentrating types, tracked or non-tracked technologies, and small- or large-scale versions. Second, the operation at elevated temperatures could lead to new physical phenomena, which would need to be explored in more detail.To put existing and possibly emerging process heat collectors on a comparative basis, collector performance testing standards have to accommodate all these issues accordingly .

Essentially, the objective of this thesis is to make contributions to improve collector performance assessment and hence facilitate the comparison between different technologies. Although collector performance assessment is undoubtedly one of the most important factors regarding the economic comparability of collectors, it should be mentioned that it is far from being the only criterion. Functional testing also plays an important role. This can include internal pressure tests, leakage tests, high-temperature resistance tests, exposure tests, thermal shock tests, rain penetration tests, freeze resistance tests, mechanical load tests, and impact resistance tests.

Fig. 2.1 roughly illustrates the common collector performance assessment procedure, which is divided into three parts that are covered in this section. Section 2.1 deals with standardized collector performance characterization, while special attention is paid to the optical characterization of the collector in Section 2.2 (and later on in Chapter 4 to 6). Section 2.3 emphasizes the importance of the previous two steps for collector annual yield simulations, which are paramount for further economic analyses and decision makers.

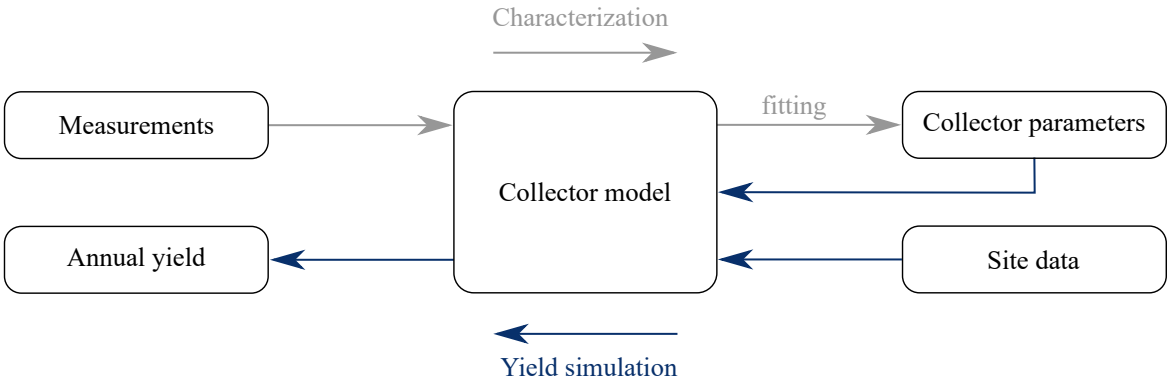

Fig. 2.1 Standard procedure for collector parameter characterization and annual yield analysis.

The Task 49 deliverable A 3.1 [32] phrases the general idea of collector performance characterization as follows: "In a broader sense, the aim of any efficiency testing procedure is to offer the possibility to predict the expected energy yield of the product at any position in the world using its respective set of weather data. To be able to do so, a generally valid and comprehensive parameterization of the collector is required."

2.1 Standardized testing procedure

In previous years there were mainly two standards of global outreach, which give thorough instructions on how to conduct collector performance measurements: The European EN 12975-2:2006 [33] and the American ASHRAE 93:2010 [34]. The most recent international standard, ISO 9806:2013 [35], comprises most parts of both the American and European versions and, after acknowledging the European standard amendment EN 12975-2:2006-A1:2011 for concentrating collectors, additionally addresses the challenges of collectors which operate at elevated temperature levels of up to 185 °C [32]. It is therefore the most interesting standard for solar process heat applications and is valid for almost all currently available designs. The collector testing standards are constantly being developed. An example of this is IEA Task 57 [36] which is dedicated to addressing shortcomings and newly arising problems in standardized methods.

At the heart of collector testing procedures lies the “collector model” – a mathematical description with characteristic physical parameters (or independent parameters), which correlate the collector output with environmental influences. In order to characterize the collector, different environmental and operational parameters, to which the collector is exposed, are measured. These parameters can, for example, include solar irradiance, wind speed, ambient temperature, and input and output temperature. The exact parameters to be

acquired depend on the particular collector model under consideration. Next comes the curve fitting. Here, the design parameters are adjusted in such a way that they minimize the error between the observations and the analytical model. This step is illustrated in Fig. 2.2 for the steady state collector model, which is described in more detail in Section 2.1.1. The Weighted Least Square (WLS) or standard Multiple Linear Regression (MLR) approach are recommended by the ISO 9806, mainly because of their popularity. However, Fischer et al. [37] also highlight the flexibility of non-least square fits over MLR. Once the characteristic parameters of the collector have been determined, they allow collector output for any other location and process-specific parameters to be calculated. For example, the required data could be taken from a Typical Meteorological Year (TMY) file database and from a heat consumption log-file of the manufacturer. The result obtained from such an annual yield simulation is essential for determining the most economically viable collector design that best fits the needs of each respective investor.

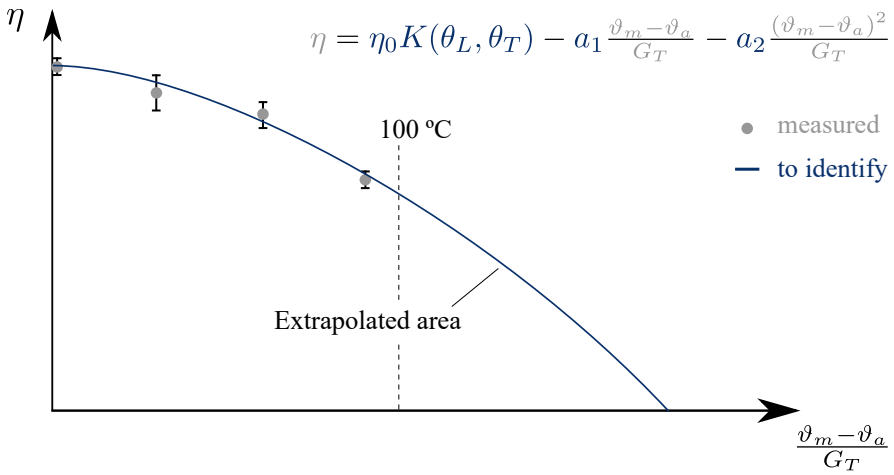

Fig. 2.2 Schematic example of the collector parameter characterization using WLS-fitting in the case of a steady state collector model (Eq. (2.1)).

2.1.1 Collector models and testing methods

As previously mentioned, the collector model plays a pivotal role in the characterization of a solar thermal collector. It is the efficiency equation that describes the principle optical and heat transfer mechanisms that occur in the collector. This equation can take different forms depending on the number of physical effects that are taken into account. This section briefly discusses the three most predominant collector models with their respective requirements regarding the testing procedure: steady state (SST), quasi-dynamic (QDT), and dynamic testing (DT).

Steady state model: Eq. (2.1) shows the steady state model, which is part of a standardized testing method described in ISO 9806:2013 [35]:

$$\eta = \underbrace{\eta_0 K(\theta_L, \theta_T)}_{\eta_{gain}} - \underbrace{a_1 \frac{\vartheta_m - \vartheta_a}{G_T} - a_2 \frac{(\vartheta_m - \vartheta_a)^2}{G_T}}_{\eta_{loss}} \tag{2.1}$$

where ϑ_a is the ambient temperature, ϑ_m is the arithmetic mean temperature $(\vartheta_{out} - \vartheta_{in})/2$ and G_T is the global irradiance on the collector plane. η_0, a_1, a_2 are the characteristic independent parameters for the MLR fitting (see also Fig. 2.2). η_0 is called the optical efficiency at normal incidence, a_1 the thermal loss factor, and a_2 the temperature-dependent thermal loss factor. Eq. (2.1) can be derived from a simple energy balance at the absorber surface, as derived in Duffie and Beckman [38]. Comparing Eq. (2.1) with the version of Duffie and Beckman reveals that η_0, a_1, and a_2 include the heat removal factor F'. Although these design parameters do have some solid physical background, the quadratic function they represent is of a rather empirical nature and is primarily valid for conventional low-temperature collectors [32]. $K(\theta_L, \theta_T)$ is referred to as the incidence angle modifier IAM, which is explained in more detail in Section 2.1.3.

To avoid quickly fluctuating collector output, operational parameters in Eq. (2.1) must be kept within a fairly narrow margin during the testing period, since the model does not consider other influential parameters. This is why the steady state method is mainly applied in indoor testing of FPCs and ETCs. There is a modified version of Eq. (2.1) which distinguishes between a direct beam and diffuse IAM and would in principle allow steady state testing to be applied to concentrating collectors. However, in this case the QDT method would be recommended [39].

Quasi-dynamic model: The QDT efficiency equation as shown in Eq. (2.2) is the second model and testing method offered by ISO 9806:2013.

$$\begin{aligned}\eta =& \eta_{0,b} K_b(\theta_L, \theta_T) G_{bT} + \eta_{0,b} K_d G_{dT} - c_6 u G - c_1 (\vartheta_m - \vartheta_a) - c_2 (\vartheta_m - \vartheta_a)^2 \\ & - c_3 u (\vartheta_m - \vartheta_a) + c_4 \left(E_L - \sigma_B T_a^4\right) - c_5 \frac{d\vartheta}{dt}\end{aligned} \tag{2.2}$$

It takes into account the absorbed energy fraction of direct beam G_{bT} and diffuse G_{dT} separately. This is essential to the testing of concentrating collectors. As with SST, the QDT efficiency equation can be derived from a one-node model, where the entire capacity of the collector is grouped together in one point. As a still linear equation regarding its characteristic parameters c_1 through c_6, it is perfectly suited for MLR. Unlike SST, the

QDT model additionally includes the terms u for the influence of wind and, c_4 for thermal irradiance (mostly for unglazed collectors), and $c_5 \cdot d\vartheta_m/dt$ for transient capacitance.

The QDT model is suitable for almost all types of commercially available collectors. It was also successfully tested for small-scale and medium-size concentrating collectors [40–42]. The constraints of maintaining certain margins for the testing parameters of Eq. (2.2) are less strict than for Eq. (2.1), as the former describes the response of a collector to more realistic environmental influences. The only condition is a relatively stable inlet temperature and mass flow rate. This is also why the QDT method can not cope very well with large-scale collectors or collector fields. The heating power required to provide the inlet temperature of such high thermal masses is often unfeasible. Only a few studies can be found for QDT of large collectors or fields [39], which is another indication that it is not suitable for such systems.

Dynamic model: The full dynamic model that describes the transient behavior of a collector aims to remove any remaining restrictions on the measurement of testing parameters. Such a dynamic model would allow in-situ measurements of large-scale systems or fields to be carried out. In many studies, the feasibility of a dynamic model has been tested under real weather conditions [39]. At this point, ISO 9806:2013 does not consider a dynamic model, despite the obvious advantages which DT offers. This is mainly due to a lack of consensus about what standardized dynamic collector equations should look like exactly [32]. What is clear, is that it is necessary to move to a more accurate representation of the collector's capacitance in order to better mirror the collector output under rapidly changing environmental conditions. There are different ways to do so. Kong et al. [43] and Xu et al. [44] describe the possibility of considering the capacitance of the fluid and absorber separately in a two-node transfer function method. Another common method results from discretizing the heat transfer element along the flow-direction and solving the one-node capacitance model for each one of the n elements and the simplified Navier-Stokes equations between the elements. Of course, it would also be possible to combine the two previous versions to a $2 \times n$-model as used, for example, in the simulation environment, ColSim [42, 45], which includes an Euler equation solver for the fluid flow. It has further been attempted to model the solar collector by means of neural networks, as in Fischer et al. [46].

In Hofer et al. [39], the authors present the results of a comprehensive literature review on testing standards and methods applied to different collector technologies and scales (Fig. 2.3). As can clearly be seen, QDT covers a much wider range of collector technologies, while the testing of fields has only been successfully reported using the DT method, with a corresponding standardized procedure yet to come.

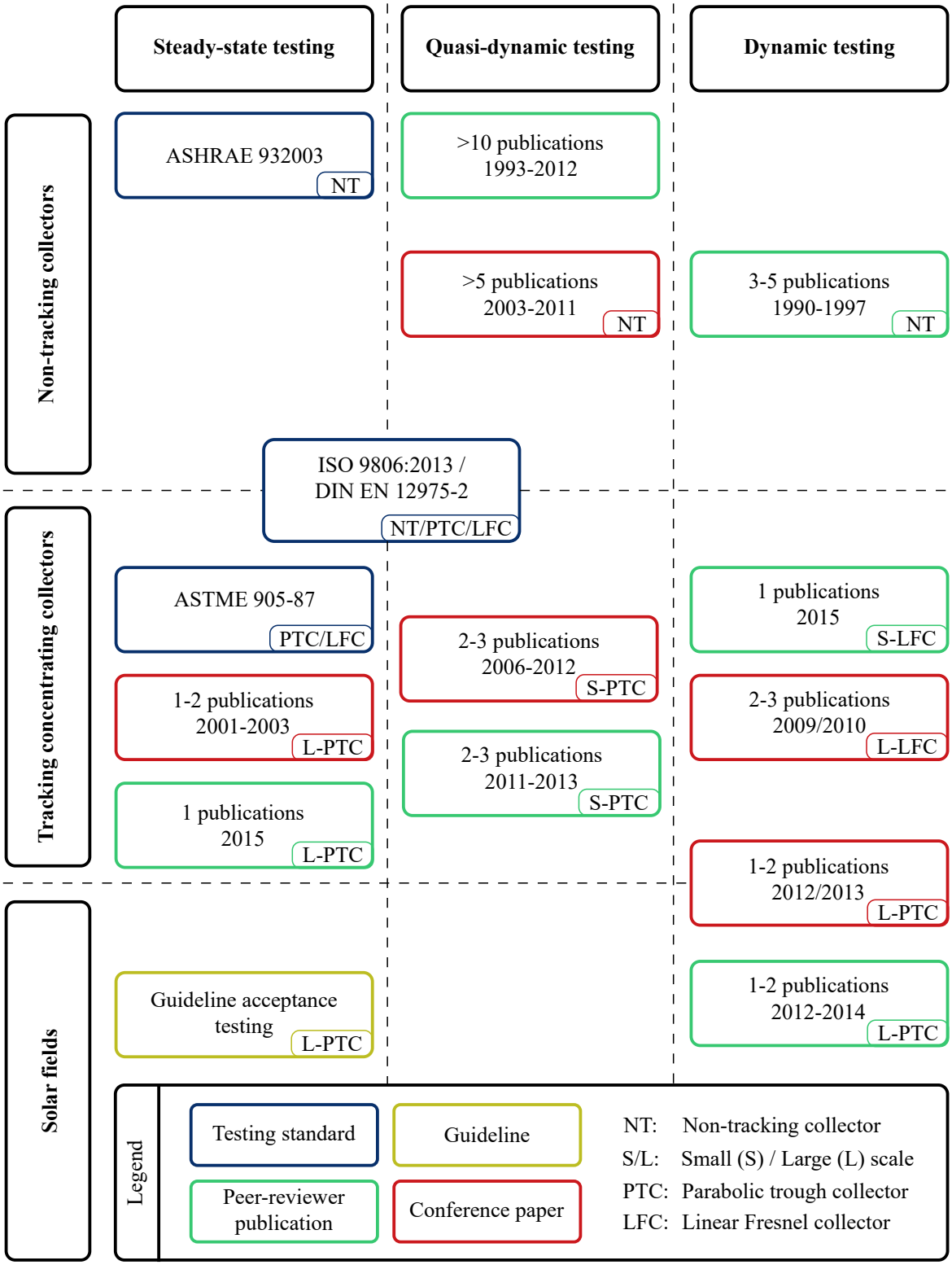

Fig. 2.3 Summary of published testing and evaluation procedures with focus on concentrating solar collectors. Adapted from Hofer et al. [39].

2.1.2 Solar irradiance: definitions and conventions

The collector efficiency is the fraction of incident solar energy that is converted into usable heat. Depending on the respective model, the efficiency equation refers to different parts of irradiance, which this section explains briefly.

Solar irradiance reaches the earth at a fairly constant rate of about $1361\,\mathrm{kW/m^2}$. This extraterrestrial irradiance is also referred to as solar constant and is usually listed in TMY-files. It is the impact of the atmosphere, which depending on the sky and ground conditions by scattering, absorption, and reflection produces a characteristic hemispherical irradiance profile above the collector aperture area on the ground. This hemispherical irradiance is typically measured for a horizontally oriented reference area so that its global horizontal irradiance G (GHI), can be roughly divided into a direct beam and diffuse part, as indicated in Eq. (2.3).

$$G = G_b + G_d \tag{2.3}$$

G_d is the diffuse irradiance, which reaches the observer from the surroundings of the solar disc. The part closer to the disc, expressed by the circumsolar ratio (CSR), has a higher intensity and is the result of mostly Mie scattering, while far away from the disc Rayleigh scattering is dominant. Diffuse irradiance can be measured with a Pyranometer and a shading ball. G_b is the direct beam horizontal irradiance and is defined as the part that reaches the earth close to or directly from solar disc. It is directly related to the direct normal irradiance (DNI) G_{bn}, which would be the radiation intercepting on a plane oriented directly towards the sun. It can be calculated by taking into account the cosine effect (Eq. (2.4))

$$G_b = G_{bn} \cos\theta_S \tag{2.4}$$

where θ_S is the zenith angle of the sun on a horizontal plane. Figure 2.4 illustrates the different parts of direct and diffuse irradiance. While on earth the solar disc appears to have a size of about 0.53°, the definition of what is to be regarded as direct beam ultimately depends on the aperture area of the measuring device. DNI is typically measured with a Pyrheliometer (Fig. 2.4), which has an aperture area of 5° to 6°. TMY files normally contain DNI values based on a 6° aperture area [47].

For annual yield simulations what is most significant is the irradiance profile on the tilted collector area. As shown in Eq. (2.5), the global irradiance on the tilted surface G_T can be split into a direct beam G_{bT} and diffuse part G_{dT}.

$$G_T = G_{bT} + G_{dT} \tag{2.5}$$

Additionally to the previously described sky diffuse part G_{sT}, the total diffuse irradiance on a tilted collector also contains a ground diffuse part G_{rT} (Eq. (2.6)).

$$G_{dT} = G_{sT} + G_{rT} \tag{2.6}$$

This is the part which is reflected by the ground and nearby buildings or other objects, and it depends highly on the situation. Ground reflection is characterized by the albedo coefficient.

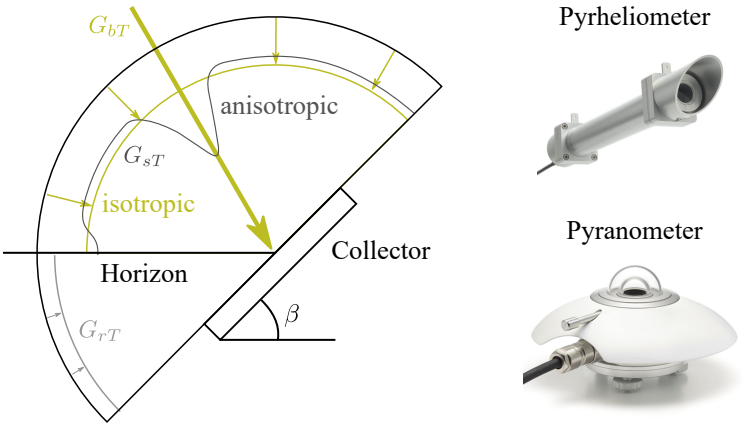

Fig. 2.4 Different types of irradiance and their respective measuring devices.

2.1.3 Incidence Angle Modifier

The IAM K in Eq. (2.2) is one of the key parameters for the annual performance predictions of the model, which is stressed in Section 2.3. IAM comprises the incidence angle dependencies of the collector's optical efficiency. According to ISO 9806:2013 [35], the IAM is defined as:

$$K(\theta) = \frac{\eta_0(\theta)}{\eta_0(\theta_{def})} \tag{2.7}$$

where θ is the solar incidence angle on the collector aperture, $\eta_0(\theta_{def})$ is the optical efficiency at a predefined angle of incidence (usually the normal incidence), and $\eta_0(\theta)$ is the optical efficiency at an arbitrary angle of incidence. Efficiency values in the ISO standard are based on direct solar irradiance G_{bT}.

Various phenomena explain the dependency of the collector efficiency on the incidence angle, the most significant ones being:

- Cosine losses
- End losses

- Angular dependency of optical properties
- Blocking and shading
- Multiple reflections (e.g., in compound parabolic collectors (CPCs))

To reduce the effort of assessing the efficiency of a solar collector according to the standard test regulations, IAM itself is described by a single mathematical model, which is usually fitted to a set of experimental node points using a linear regression approach. A one-dimensional model was proposed by Souka and Safwat [48] for basic rotationally symmetric collectors such as FPCs or line-tracked collectors. This model can be completely defined by a single node point measured for an incidence angle of 50° [35].

In particular, solar collectors for industrial applications are often more complicated in design and are not rotationally symmetric. Examples for this are CPCs, FPCs, or the MaReCo photovoltaic thermal hybrid (PVT) collector. These types of collectors cannot be properly characterized by a single IAM-curve but only by an IAM-surface. Assessing the entire surface experimentally would be tedious or unfeasible. An accepted and more efficient approach for geometries that are not rotationally symmetric around the collector normal (e.g., most concentrating collectors or ETCs) is the semi-experimental factorization approach proposed by McIntire [49]:

$$K(\theta_L, \theta_T) = K(\theta_L, 0)K(0, \theta_T) \tag{2.8}$$

where θ_T and θ_L are the incidence angle projections onto the transversal and longitudinal planes of the collector, respectively (Fig. 2.5). Instead of experimentally obtaining data for the entire hemisphere over the collector aperture, IAM is measured only for a finite set of incidence angles along the two symmetric planes [35]. The IAM surface is then constructed by multiplying the transversal and longitudinal IAM values sorted in a matrix of (θ_T,θ_L).

2.2 Optical efficiency assessment

So far, Chapter 2 has covered the performance assessment of a solar collector in general. This thesis makes contributions mainly in the field of optical simulations (Chapters 4, 5 and 6). To appreciate this fact, the focus in this section is on solar materials, collector components, and the optical characterization of solar collectors. The results of material and component testing serve as input to optical simulations, so the two fields are directly linked and have been accommodated under the term "optical efficiency assessment."

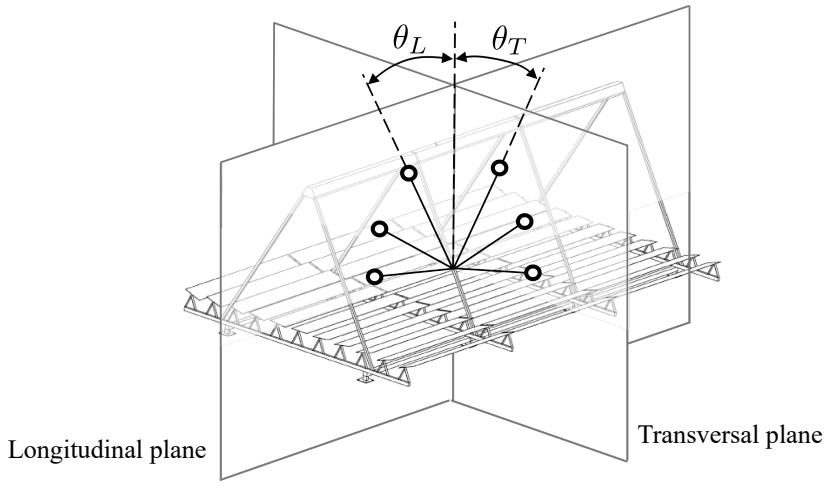

Fig. 2.5 McIntire factorization: The IAM at an arbitrary sun position on the collector equals the product of the IAMs at the respective angle projections θ_T and θ_L.

2.2.1 Solar energy materials

This section provides a general overview on commonly used materials and those materials that show potential for use in the near future. Since the focus is on concentrating solar collectors, materials are divided into the following groups: "transparent and semi-transparent", "reflective", "absorptive," and "coatings."

Transparent and semi-transparent

Transparent and semi-transparent materials are mainly used as covers for protection and heat loss reduction. Doubtlessly, such covers come at the cost of a lower optical efficiency, which makes it even more important to model this part of the collector adequately.

At this point, the most employed material for covers is solar/optical glass, which is made of borosilicate with a low iron content. One conventional example for such a glass is the Schott BK-7 type [50]. While solar glass was previously the main choice for solar covers, it has become more popular recently to employ semi-transparent polymeric materials. The advantages are manifold: low costs, less weight, and almost no restrictions on the design. When it comes to essential optical properties such as transmittance, polymers still perform poorly in comparison to glass. However, due to their good mechanical properties, polymer covers can be made extremely thin, which makes this drawback less significant. A good example for such an application is the PTC prototype of Bader et al. [51]. French et al. [52] and Köhl et al. [53] give an overview of promising polymeric materials for use in solar thermal applications.

Reflective

Reflective material is used for mirrors. To be used in concentrating solar collectors, they need to be stable, stretch- and soil-resistant, durable, and highly reflective in the range of short wavelengths of the solar spectrum. As for the base material of the mirror, there are three different types commercially available: glass mirrors, polymer mirrors, and aluminum mirrors.

Glass mirrors are the most common type of mirror. They usually have a 4 mm thick solar glass layer with a thin reflective silver layer underneath. A paint layer protects the silver from environmental impacts such as corrosion. This type of mirror is very resistant and durable, but comparably expensive and heavy. Moreover, the 4 mm glass substrate reduces the mirror's reflectance. To improve optical performance there are versions with a 1 mm substrate, which, however, come at the cost of reduced rigidity. An additional metal sheet on the back side of this mirror can compensate this loss.

Polymer mirrors come as a thin foil and use transparent polymers as a substrate. The core part of the mirror is a reflective silver or aluminum layer protected by a copper layer on the back side. Finally, a thin polymer film at the front and back side further protects the metal stack from environmental impacts. Polymer mirrors are extremely light, flexible, and cheap, but also less durable and less resistant than glass mirrors. Bader et al. [51] use MyLar polymer mirrors for their PTC.

Aluminum mirrors start from an anodized aluminum substrate that has either a pure aluminum or a silver layer on top for reflection. To protect the reflection layer from corrosion and abrasion, the mirror is also covered with a reflectance enhancing, protective coating. The advantage of aluminum mirrors is a comparably low weight at a still high rigidity. The overcoat of the mirror plays an important role for the optical performance and is explained in more detail in the following paragraphs.

Absorptive

Solar absorbers are mostly made of stainless steel, copper, ceramics (solar towers), or less common types of polymeric material (pool collectors or, rarely, in FPCs) [53]. The substrate of the absorber has to guarantee a high heat transfer coefficient. The most important part of the absorber is, however, its selective overcoat. This should show high absorption in the short wavelength region (UV-Vis) but low absorption/emission in the long wavelength region (infra-red thermal radiation (IR)). According to Kirchhoff's law, a low absorption is equivalent to a low emission, which allows making use of most of the energy of the incident

irradiance. The other main requirements for a selective coating are thermal stability at the operating range, good adhesion to the absorber substrate, and resistance to corrosion. In fact, commercially available coatings are designed for a specific temperature range [54].

Coatings

All of the above-mentioned material types are accompanied by some sort of surface treatment to improve their optical properties. Absorbers have a selective overcoat to allow better energy use of the incident solar spectrum; antireflection layers on covers reduce their reflectance and simultaneously enhance transmittance, and mirrors have a high-reflectance coating to improve reflectance, sometimes to an even greater extent than the pure metal, while also protecting the reflective layer. Today's processing methods allow coatings to be processed with a high degree of accuracy, providing significant freedom to their property design.

In Fig. 2.6 it can be seen how antireflection (AR) and high-reflectance (HR) coatings work. While AR coatings are applied to reduce surface reflectance, HR coatings try to achieve exactly the opposite. Despite their contrary effects, their underlying principle is the same. These coatings consist of one or multiple thin layers[1]. As an electromagnetic wave propagates through the thin-film assembly, it is partially reflected at the layer interfaces according to the Fresnel equations (3.2) and (3.3). Given a specific refractive index for each layer, their thickness can be adjusted for a specific wavelength, such that interference of the reflected light is either destructive (AR coating) or constructive (HR coating). The resulting overall reflectance of the stack is then low or high. Absorption within the thin-film assembly is not desired, which is why they consist of dielectrics.

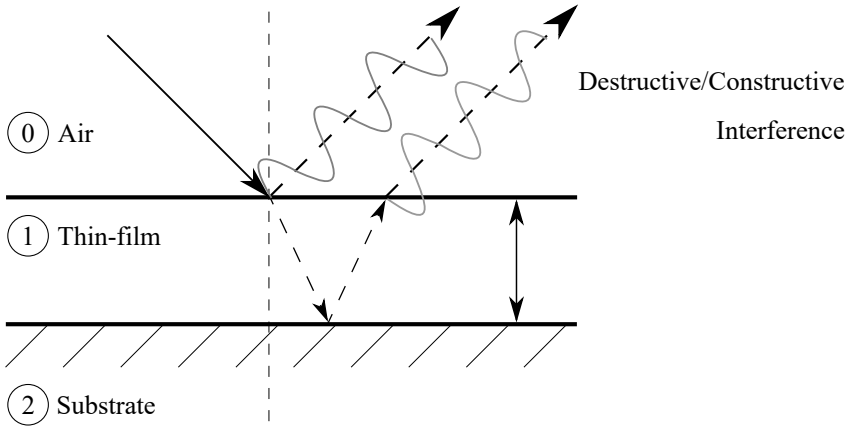

Fig. 2.6 Principle of antireflection and high-reflectance coatings.

[1] Of the same magnitude as the wavelength of the incident light.

The simplest version of an AR coating is a single MgF_2 layer with the thickness of a quarter of the target wavelength. When constructing a single HR layer on a metal surface it should be noted that the complex part of the refractive index of the substrate material can not be neglected [55].

Coatings only perform well in the range around the wavelength and incidence angle they were designed for. The use of multiple quarter-wavelength layers of alternating low (L) and high (H) refractive indices is one approach among others to produce broadband AR or HR coatings. Commonly used dielectric materials are MgF_2, SiO_2, TiO_2 [56–58], HfO_2, Si_2N_4, Al_2O_3 or ZnO [55, 59]. Other increasingly popular low-refractive materials are sol-gels. The sol-gel process allows the manufacture of porous layers with an almost tailor-designed refractive index [60–63].

Selective coatings show low reflectance in the short wavelength range and high-reflectance (low emission) in the long wavelength range. Most coatings incorporate metal, which functions as an infra-red reflector, while the dielectric matrix substrate mainly absorbs in the UV-Vis spectrum. Four types of selective surfaces can be distinguished: intrinsic, metal-semiconductor tandem, metal-dielectric composite (e.g., cermets), or textured surfaces [54, 60, 64] (Fig. 2.7). To reduce reflection losses, selective coatings often also have an AR coating on top. The principle of textured surfaces differs from the other methods in such a way that short wavelength radiation is "trapped" in a complex structure and finally absorbed after multiple reflections.

The most widely used concepts are composites or dielectric-metal multi-layers [54]. Selective coatings are designed for a narrow operation range. High-temperature coatings are often based on Al_2O_3 as a dielectric due to its high thermal resistance. Other dielectric matrix materials are AlN, SiO, and MgO [54]. Also possible for high-temperature resistant selective coatings is the assembly of the metallic-like TiAlN with the semiconductor TiAlON on top of a metallic IR reflective layer or directly on the substrate [65–67] or composites of $MoSi_2$ (conductor) and Si_2N_4 (dielectric)[68].

Another positive effect of coatings is to make materials more resistant to soiling. In this light, TiO_2 needs to be highlighted as a dielectric material with a number of additional favorable properties. Not only does it show high scratch resistance, but its photocatalytic properties also accelerate the decomposition of organic particles, which leads to a self-cleaning effect [59, 60].

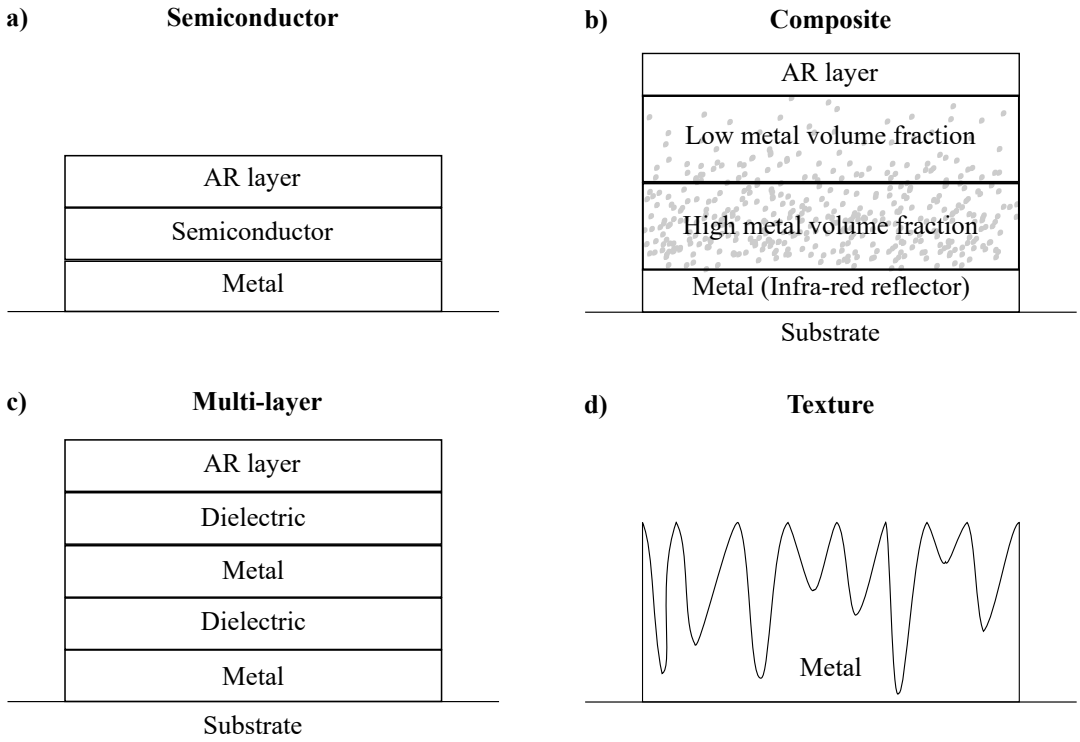

Fig. 2.7 Structures of selective coatings: a) semiconductors b) dielectric-metal-composites c) dielectric-metal multi-layers d) textured surface.

2.2.2 Material and component testing

When a solar collector is to be simulated, the accuracy of the results highly depends on how much information is available about the optical and structural properties of its materials and components. In this respect, the terms "materials" and "components" refer to two different ways of carrying out experiments.

One way of obtaining experimental results would be to analyze an entire assembled collector unit such as a receiver tube. The advantage of this approach is that not only optical, but also structural, geometrical, and even thermal characteristics can be assessed at once. For example, in practice a receiver unit is never ideal. Its optical properties are not perfectly distributed, it is not perfectly straight, and it has impurities or damage, supporting elements, and thermal dependencies. All of this influences the overall optical efficiency of the tube, which is why some collector units are often analyzed as a whole on a specialized test bench. The Task 49 deliverable [32] mentions three basic collector components worth analyzing: The receiver, the reflector, and the tracking system. At this point, only the importance of reflector shape deviation measurements shall be stressed, as it is an input parameter paramount for accurate optical simulations. There are several techniques to determine the deviation of

mirror shape from the perfect shape it is supposed to have. Such deviations partially occur during the manufacturing process but are mainly introduced during the assembly due to less than ideal placement of the mirror facets or tight screws, which deform the mirror. Popular methods to determine the shape deviation are deflectometry, photogrammetry, laser techniques, or derived versions of these approaches. Some examples for reflector shape characterization are given in Prahl et al. [69], Jones et al. [70], and Ulmer et al. [71].

Another way to conduct experiments would be to obtain the more general optical properties of a neutrally shaped sample, such as a small, flat piece of the manufacturer's mirror, absorber, or transparent material, which can easily be placed in a standard laboratory device like a spectrophotometer, for example. The advantage of this method is that results are more general and more suitable for ray-tracing simulations, but they do not account for flaws and effects introduced by the assembly and shape when used in a collector component. In ray-tracing simulations there exists a commonly acknowledged way to use the general optical properties of the materials while, at the same time, accounting for structural effects. This approach is presented in Chapter 3.

For now, this section focuses on the second approach and explains the most important optical parameters to characterize a material sample, as it plays a more important role for the ray-tracing analyses presented in the following chapters. In general, when an electromagnetic wave is incident on a material surface there are only two possible ways it can interact: It can be either reflected or transmitted. Furthermore, if the light passes through to the next medium with a higher refractive index, it will be absorbed gradually. So, in total when light traverses an optical medium with a different refractive index, all energy fractions add up to 1.

$$R(\theta,\lambda)+T(\theta,\lambda)+A(\theta,\lambda)=1 \tag{2.9}$$

where R is the reflectance, T the transmittance, and A the absorptance of the volume. All coefficients depend on the wavelength, the incidence angle, and the polarization of the incident light. Given Eq. (2.9), it is possible to derive three different material classes typical for solar thermal applications: reflective materials ($R \gg$, $T = 0$), absorptive materials ($R \ll$, $T = 0$), and refractive materials ($A \ll$).

While Eq. (2.9) is an energetic balance, it is important to note that due to the material's surface texture, the reflected or transmitted wave will in practice not be perfectly specular, but will rather show a characteristic distribution over the sample's hemisphere. This phenomenon is called scattering and can be described by a bidirectional reflectance distribution function (BRDF). Usually, integrating spheres, which detect incident light in all possible directions from $-90°$ to $90°$, are used to deal with scattering from a material sample.

Some experimental setups for the measurement of the reflectance or transmittance of different materials are found in Fig. 2.8. Measuring specular reflective materials can be especially challenging. In concentrating solar thermal applications, mirrors are expected to reflect most of the incident light within a certain tolerance cone around the specular direction. The more the reflected image of a mirror is scattered, the higher the efficiency losses. This means that both the overall amount of reflected light (hemispherical reflectance) and the amount reflected near the specular direction (specular reflectance) need to be determined in order to characterize solar reflectors properly. It is still subject to definition up to what degree around the specular direction the reflectance should be called "specular". Manufacturer data for R_s usually refers to an acceptance angle of $\varphi = 25\,\text{mrad}$ (1.4°) [72, 73].

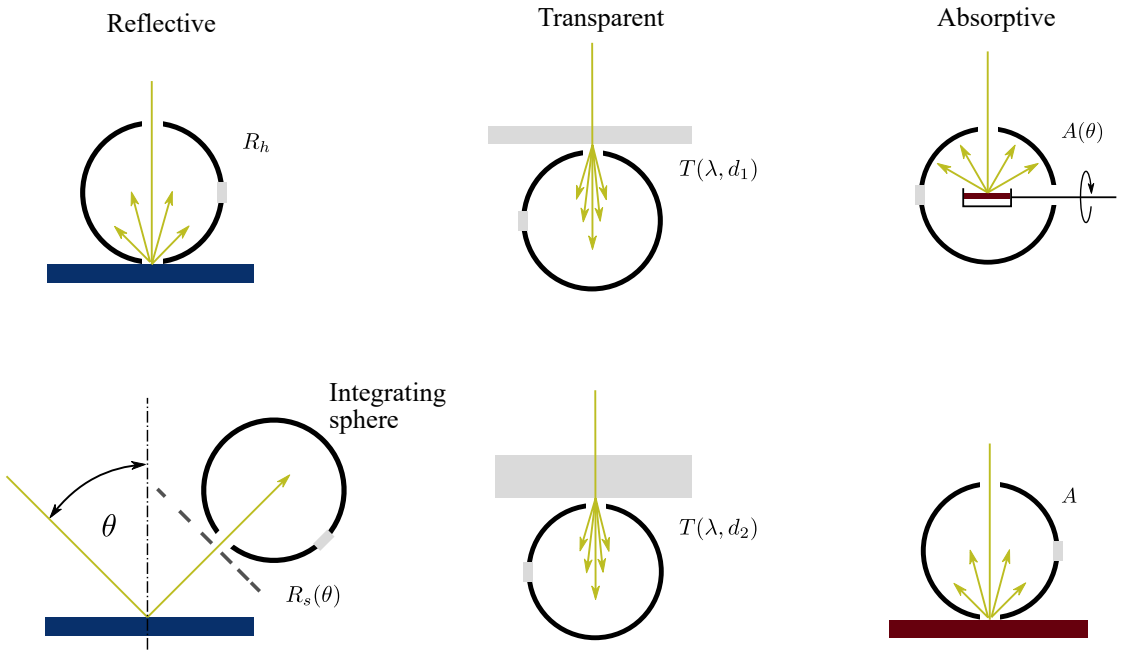

Fig. 2.8 Experimental setup to measure the optical properties of different materials using integrating spheres.

To measure the hemispherical reflectance, the mirror sample is placed directly below the integrating sphere, as shown in Fig. 2.8 (left). In order to obtain good results for optical simulations, this step should be repeated for different angles of incidence and, preferably, for different wavelengths. Figure 2.9 also shows the experimental setup to determine specular reflectance. During measurements, the sample is exposed to collimated light, which after being reflected is focused by a precise low-scatter parabolic mirror or lens. The integrating sphere is placed right at the focus to detect the signal [74, 75]. Alternatively, in some studies a CCD sensor is used in place of the integrating sphere (such as in Good et al. [76] and Heimsath et al. [77]).

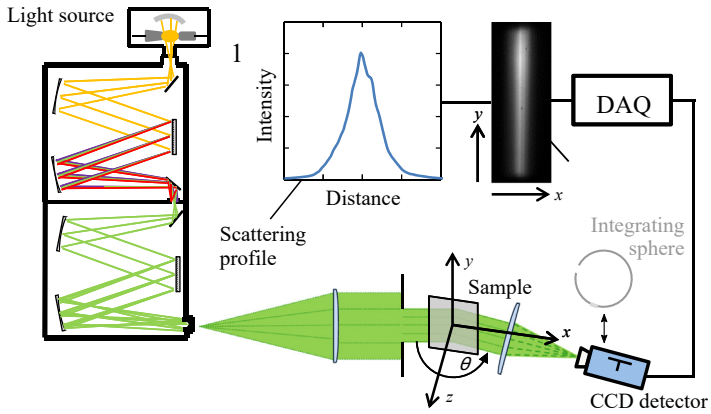

Fig. 2.9 Experimental setup to measure the specular reflectance of a mirror sample by means of a CCD-sensor. Reprinted from Good et al. [76].

In the case of highly specular solar mirrors, the scattered light is generally supposed to correspond to a Gaussian profile (see also Section 3.4). An exception to this is Montecchi's study [75], which suggests that an exponential total integrated scatter (TIS) relationship would be more realistic and beyond that would allow the derivation of the spectral dependency of scattering. However, the majority of literature and measurement standards as well as current indicative references such as the SolarPACES group III reflectance guideline advocate the original Gaussian profile approach [74, 78–80].

If a CCD sensor is used, a Gaussian profile is fitted to the detected density profile. In the case of an integrating sphere, at least three different aperture areas in the range of $0 < \varphi < 20\,\text{mrad}$ are used, and a Gaussian curve is again fitted to the different observations. So far, little attention has been paid to the fact that not only does the hemispherical reflectance depend on the incidence angle and wavelength, as implied by Eq. (2.9), but also the specular reflectance. There exist only a few studies which fully analyze the incidence angle and wavelength-dependent behavior of scattering, among them, Heimsath et al. [77] and Good et al. [76], with the latter being the only one that provides an analytical relationship (see Chapter 4).

The principle of measuring the transparency of refractive material according to Fig. 2.8 (center) can be similar to that of a mirror [52]. When light passes through transparent material it is scattered and partially absorbed. The overall transparency or haze value of the sample depends on both its surface texture and its thickness, and is also measured by means of an integrating sphere. With this typical setup of an integrating sphere and a spectrophotometer it is not difficult to provide the transparency values and their dependency on the wavelength. As shown in Section 3.6, it is especially challenging to reconcile the typical results of measurements for transparent materials with the required input for ray-tracing simulations.

Solar absorbers are often not as thoroughly assessed as, for example, mirrors. Typically, the manufacturer provides a solar absorption and thermal emission coefficient measured at near normal incidence. It is also possible to obtain the spectral reflectance curve at this given angle, but usually there is no data available about the incidence angle dependency, let alone about the scattering characteristics of the reflectance of an absorber. An example of a study that assesses the incidence angle dependent absorptance coefficient of solar absorbers is Tesfamichael and Wäckelgård [81]. The lack of more accurate information can make it difficult to carry out optical simulations.

2.2.3 Monte Carlo ray-tracing analysis

Ray-tracing simulations are an elegant approach to determine the optical efficiency of a solar thermal collector. The algorithm traces rays as they propagate through the collector domain (Fig. 2.10). After a chain of intersections and interactions with different materials, the ray finally either hits the absorber and is absorbed, which results in an increasing surface temperature, or becomes lost during the process. These algorithms are often based on the Monte Carlo principle, which means that each ray is generated as a random instance with properties derived from probability density functions. With an increasing number of emitted rays, the fraction of absorbed photons with respect to the total number of emitted photons will converge towards a constant value corresponding to the optical efficiency of the collector.

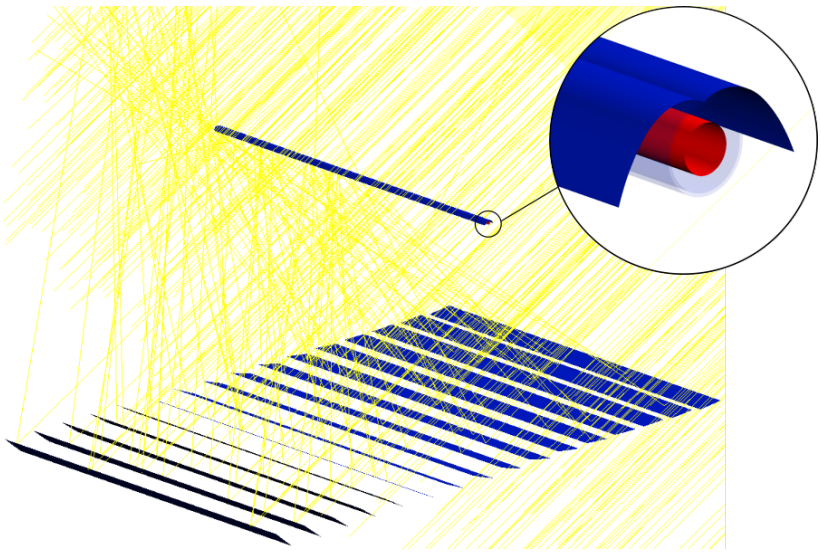

Fig. 2.10 Ray-tracing simulations: The algorithm traces rays as they propagate through the collector domain and interact with its materials.

The Monte Carlo ray-tracing approach is very efficient and needs comparatively few resources given the geometrical complexity of the problem it is used on, which makes it very suitable for solar thermal applications. However, it is also important to be aware of the limitations and underlying simplifications of the ray-tracing approach. These algorithms apply geometrical optics. They provide solutions to the simplified Maxwell equations for plane wave propagation and homogeneous, isotropic optical material properties. As such, they do not take into account interference or diffraction effects, nor any other effects caused by in-homogeneously distributed optical properties within a material. In some cases, there are workarounds for some of these limitations. Moreno et al. [82], for example, successfully simulate the holographic effect of a transparent cover with variant refractive index along one axis. Some commercial ray-tracing programs also allow interference patterns to be derived based on Gaussian beam and matrix analysis for standardized optical components. In general, if the problem is more complex, computational optics should be the preferred choice.

A list of some commercial, open source, or in-house ray-tracing programs that are available can be found in Table 2.1. Usually, commercial tools can be used to simulate many problems, including setups of high-precision optical lenses, whereas open source and in-house programs have been developed by the scientific community with the purpose of analyzing solar thermal collectors, and thus they only have a limited set of optical models implemented. The question arises, especially for open source programs, whether their rather simplified models are also applicable to newly developed surface-treated solar materials as discussed in the previous section and whether the allowed parameter input is flexible enough to render the increasingly more accurate data provided by the manufacturers. This subject is covered in Chapter 4.

Table 2.1 Examples of existing ray-tracing software.

Software	Developer	License
ASAP [83]	Breault Research Organization	Commercial
OptiCAD [84]	OptiCAD cooperation	Commercial
RayTrace3D [85]	Fraunhofer ISE	In-house
SimulTrough [86]	ENEA	Open source
SolTrace [87]	NREL	Open source
SPRAY [88]	DLR	In-house
Tonatiuh [89]	CENER	Open source
TracePro [90]	LAMBDA	Commercial

2.3 Annual yield simulations

All of the previously mentioned subjects on standardized collector testing and optical efficiency assessment represent merely one step towards the most important issue: the efficient and reliable comparison of different collector technologies. Counter-intuitively, the characteristic collector efficiency curve alone is not a reliable criterion to assess the profitability of a collector. This fact is illustrated in Fig. 2.11. While the efficiency curves of different types of collectors clearly seem to imply a certain tendency, this order changes decisively when examining the expected annual yield of each collector, which is, economically speaking, a much more meaningful parameter. Ultimately, the choice between two different solar collectors cannot be made simply by comparing the respective optical or thermal parameters but only by annual integration of their energy output.

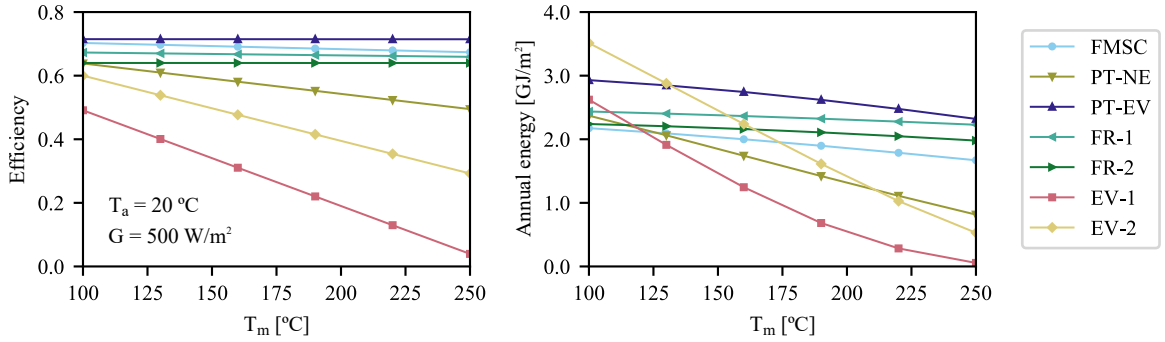

Fig. 2.11 The collector efficiency curve (left) is not a reliable criteria to assess the profitability of a collector. Annual yield calculations (right) are more meaningful. Adapted from Martínez-Moll et al. [91].

Some certification bodies, in addition to the thermal and optical collector parameters, include some type of rating value based on simulations in order to improve the comparability of the product. The European certificate Solar Keymark [92], for example, states the calculated annual yield for four representative locations with different weather conditions: Athens, Davos, Stockholm, and Würzburg. The calculations are based on a program called ScenoCalc [93], which was developed by the former Technical Research Institute of Sweden (SP) [94] under the framework of the European QUAiST project. The American certification body SRCC [95], on the other hand, chooses a slightly different approach and provides an hourly thermal collector output based on three different rating days: a low, medium, and high irradiance solar day. These rating values are supposed to be analogous to energy efficiency ratings found in household appliances and mileage ratings as applied to automobiles.

Doubtlessly, the more details the simulation takes into account, the more accurate the results. However, the more complicated the simulation, the more expertise and engineering

resources are necessary, which in turn reduces interest in investing in the technology. Consequently, a trade-off between accuracy and simplicity must be found. Different simulation programs and methodologies have been developed to meet this target. One example for a simulation program is the previously mentioned ScenoCalc, which calculates the annual collector yield based on either SST or QDT parameters. Another example is the Java-based GainBuddy developed by SPF [96]. GainBuddy is similar to ScenoCalc, with the difference that it additionally considers basic field parameters such as the shading between collector rows. A more sophisticated, but also more complicated simulation software is SAM - developed and maintained by NREL [97]. SAM allows the definition of transient characteristics such as the thermal capacity of the system. Apart from these simulation tools, there exist other methodologies which are also based on annual yield simulations and are supposed to facilitate collector comparison. Martínez-Moll et al. [91] suggest deriving the same collector-specific energy contour diagrams based on a functional fit to a point cloud derived from a global weather data base (Fig. 2.12).

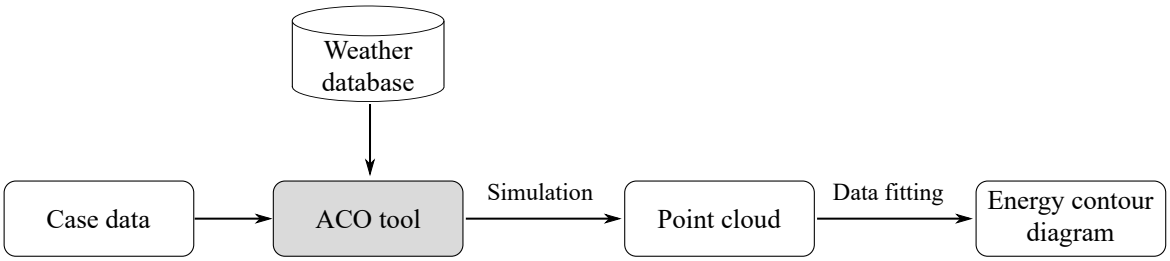

Fig. 2.12 Procedure to produce annual collector output charts from weather database and standardized collector parameters as proposed by Martínez-Moll et al. [91].

The question about which phenomena to include in annual yield simulations is still open to debate. In their report, Hess and Schmitt [98] point out the importance of a more accurate diffuse sky model in order to better predict the annual yield of non-imaging low concentrating collectors. Hess [99] mentions that the use of a simple isotropic diffuse model over a more sophisticated one could underestimate the annual yield by up to 40 %.

Chapter 3

Further development of OTSun

One of the major contributions of this thesis has been the further development of the in-house ray-tracing software OTSun. OTSun was first developed as a FORTRAN code at the University of the Balearic Islands [100]. The code was further validated in Sallaberry et al. [1], Pujol-Nadal [101] and Pujol-Nadal et al. [102]. Pujol-Nadal et al. saw a need for a new ray-tracing code, because of a lack of some fundamental mathematical models in existing open source codes. According to the authors, there have been shortcomings especially in the proper modeling of the incidence angle dependency of the glazing and the absorber. OTSun is currently being developed to include some new features, which are described in this chapter. The code is also being incorporated into the Python-based open source platform FreeCAD from which it will be publicly available, and it enables a more intuitive and user-friendly usage [103]. The following section refers to the first FORTRAN-based version plus all recently implemented improvements. This set of new features is the result of the literature research outlined previously in Sections 2.2.2 and 2.2.3.

The outcome of the simulations is the optical efficiency of the collector with respect to DNI (G_{bn}). Hence, the cosine effect is included in the incidence angle modifier, as shown in Eq. (3.1):

$$\eta = \frac{\dot{Q}}{A_{ref} G_{bn}} = (\alpha\tau\rho)_0 \cdot K(\theta) \tag{3.1}$$

3.1 Program overview

Fig. 3.1 represents an overview of the program that has been developed for the purposes of this thesis. Its structure can be separated into three core parts: the Python and FORTRAN-based

run-time routine, the user-defined case description, and a more permanent material/reflectance database.

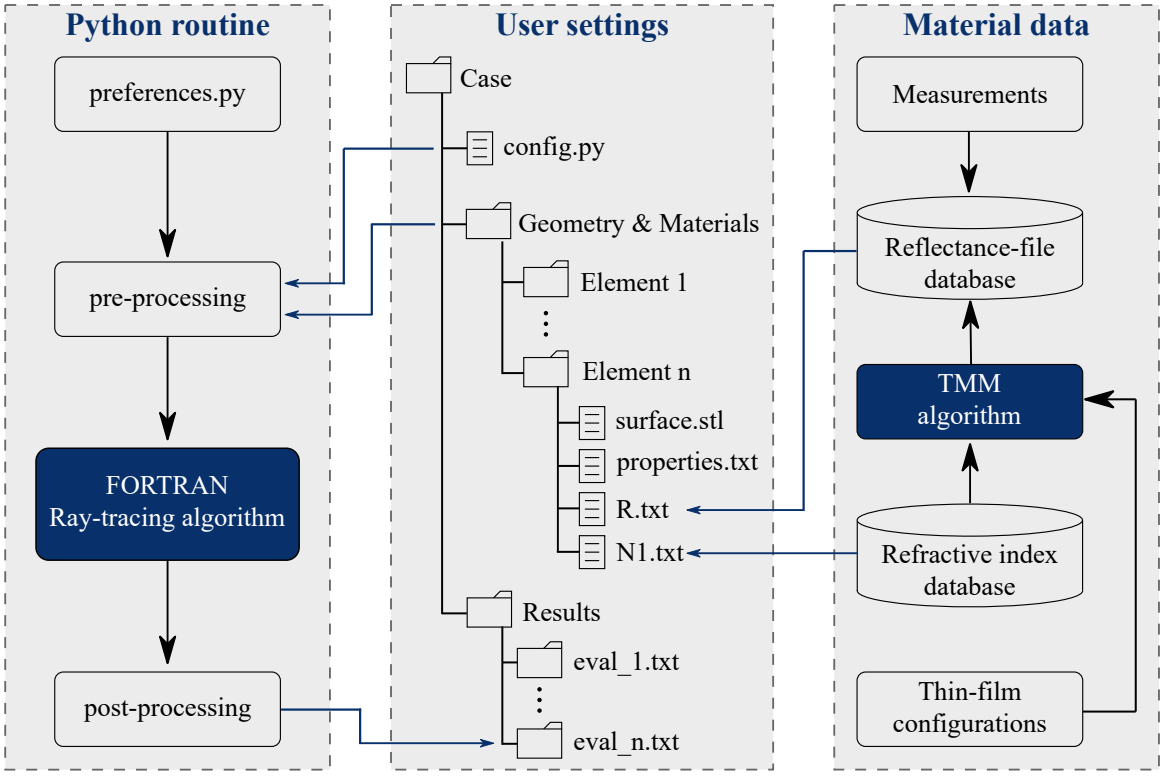

Fig. 3.1 Overview of the basic structure of the ray-tracing code developed for this thesis.

At this point a graphical user interface is still not available, so all input is based on data files stored in the case folder. One part of the case folder contains the collector model which is topologically composed of surfaces. The information of surfaces with shared optical and mechanical properties is contained in separate directories. Often, but not necessarily, these sub-units correspond to different functional collector components such as the absorber tube or a single mirror row or facet. Each surface-subdirectory contains the following files:

- *geometry.stl*
- *properties.txt*
- *N.txt* (refractive index, optional)
- *R.txt* (reflectance, optional)
- *sigma.txt* (scattering, optional)

The geometry.stl file contains the geometrical description of the surface. Each surface, no matter its shape, is composed of a finite number of triangles. Consequently, the .stl-file contains a list of triangle coordinates. STL is a standardized format supported by most CAD programs [104].

The properties.txt file has a total of 34×4 entries to define all the optical and mechanical properties of the surface element. Mechanical properties basically include the tracking type and local coordinate system of the component. Options and parameters of these mechanical properties can be defined in lines 28 to 34 of the properties file, found in Table 3.1.

Table 3.1 Part of the properties.txt file to define mechanical parameters.

Parameter	Index	Value			
		1	2	3	4
Tracking mode		0 (static)			
	28	1 (linear)			
		2 (CCStaR)			
Focal point	29	x_{foc}	y_{foc}	z_{foc}	
Local COSY	30	$e1_x$	$e1_y$	$e1_z$	
	31	$e2_x$	$e2_y$	$e2_z$	
	32	$e3_x$	$e3_y$	$e3_z$	
Local COSY origin	33	x_{origin}	y_{origin}	z_{origin}	
Rotational axis	34	x_{track}	y_{track}	z_{track}	

For the complete description of the optical properties of an element, it is necessary to assign a surface type, a reflectance model, a scattering model, and refractive indices (real and imaginary part) on the front and back side of the element's surfaces, as illustrated in Fig. 3.2.

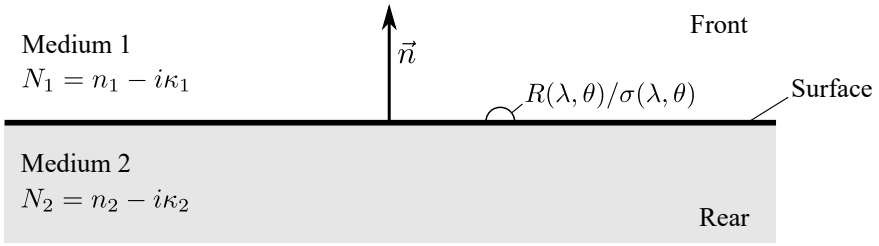

Fig. 3.2 Optical properties that have to be assigned to an interface according to Table 3.2.

All optical models can be defined in lines 1 to 6 of the properties.txt file, seen in Table 3.2. Not yet available but soon to be implemented models are shown in gray. The optical models

in Table 3.2 are described in the following sections. In principle, the selected reflectance, scattering, and refractive index can either be based on analytical models (Section 3.2.1 to 3.2.3) or can be imported and interpolated from external data files, which, in this case should be provided as R.txt (reflectance), N.txt (refractive index), or sigma.txt files (Gaussian scattering variance).

It is due to this import of reflectance data files that the ray-tracing code can deal with more complex surface textures such as coatings. Many R.txt files have previously been generated by means of the optical transfer matrix method (TMM) explained in Section 3.2.2. The only input required for the TMM simulations is an accurate description of the coating composition and the refractive indices of the respective layer materials. The resulting R.txt files with their incidence angle and wavelength-dependent reflectance coefficients are stored in a small reflectance data base (Fig. 3.1). Apart from numerical simulations, these files could also be obtained from experiments.

Now that the different optical models have been chosen in lines 1 to 6, the corresponding parameters for each model have to be provided. Table 3.3 shows entries 10 to 24 of the properties.txt file which is reserved for optical parameters. The parameters defined in this section of the file have to be coherent with the models defined in lines 1 to 6.

The executable part of the program is based on a Python code (Fig. 3.1, left). During run-time, the program imports the collector model files and the config.py file from the case folder. The config.py-file contains the necessary information for the ray-tracing simulations. This is the:

- Sun model
- Number of rays
- Spectral/Non-spectral simulation
- Sun positions θ, φ

Once the configuration settings and the available collector model files have been positively checked for plausibility, the program calls the pre-compiled FORTRAN-ray-tracing code for more time efficient simulations. After successfully finishing the ray-tracing simulation the results are post-processed and stored back into the case directory.

Since the geometry of a collector is composed of surfaces, it is important to explain how OTSun simulates the optical properties of a volume. Basically, all optical effects can be categorized into two groups: surface effects and volume effects. The first comprises

Table 3.2 Part of the properties.txt file to define optical models.

Parameter	Index	Value			
		1	2	3	4
Surface type	1	-1 absorptive 1 reflective 2 transparent 3 opaque 4 diffractive			
Reflectance model	2	1 constant 2 $R(\lambda,\theta)$-file 3 $R(\lambda)$-file 4 Tesfamichael 5 Grena 6 Schlick 7 Lazanyi 8 Fresnel* 9 τ * 10 τ-model*			
Scattering model	3	1 None 2 Lambertian 3 Gaussian 4 TIS 5 BRDF			
Spectral sigma	4	1 constant 2 $\sigma(\lambda,\theta)$-file 3 Power law			
External refractive index N_1	5	1 constant 2 file 3 Sellmeier 4 Drude-Lorentz			
Internal refractive index N_2	6	1 constant 2 file 3 Sellmeier 4 Drude-Lorentz			

Table 3.3 Part of the properties.txt file to define optical parameters.

Parameter	Index	Value			
		1	2	3	4
Reflection coefficient	10	ρ/coating-idx/ρ_{front}	ρ_{back}		
Tesfamichael/Lazanyi	11	b/a	c/b	$-/c$	
	12				
σ_1 (x-direction)	13	σ_{11}/file-idx/$\lambda_{ref,1}$	p_1	b_1	q_1
σ_1 (y-direction)	14	σ_{12}/file-idx/$\lambda_{ref,2}$	p_2	b_2	q_2
σ_2 (x-direction)	15	σ_{21}/file-idx/$\lambda_{ref,3}$	p_3	b_3	q_3
σ_2 (y-direction)	16	σ_{22}/file-idx/$\lambda_{ref,4}$	p_4	b_4	q_4
Weighting factor	17	K			
Macro errors	18	σ_1			
Macro errors	19	σ_2			
Rolling mark angle	20	α_{roll}			
Refractive index N_1	23	n_1/file-idx	k_1/α_1		
Refractive index N_2	24	n_2/file-idx	k_2/α_2		

phenomena which originate from light being incident on an interface between two media of different refractive indices. The most important phenomena for ray-tracing simulations are reflection (Section 3.2), refraction (only refractive material), and scattering (Fig. 3.3, Section 3.4). Beside the phenomena that occur when a ray impacts on an interface between two media, there are different effects that describe the propagation through a medium. As can be seen in Fig. 3.3, typical volume effects are bulk scattering and absorption (Section 3.5). At this point, OTSun only considers the absorption in a medium by defining its complex refractive index.

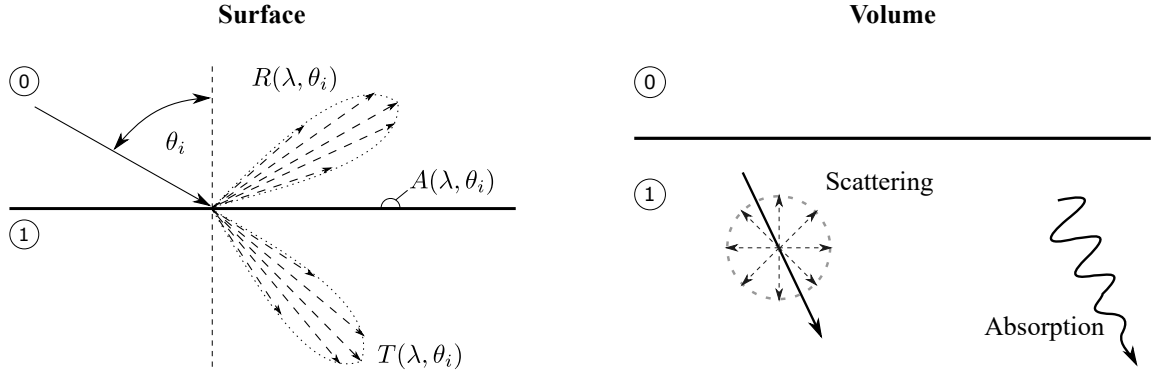

Fig. 3.3 Different phenomena that may occur at the surface or inside optical materials.

It should be stressed that refractive materials are especially difficult to handle in ray-tracing simulations. This is due to the fact that in the laboratory often only a single transparency or haze value is measured [50, 52] (Section 2.2.1); in this case, it is not possible to report to which extent this value originates from the effects at the surface or in the volume. This, however, would be a required parameter input in most ray-tracing codes. As a consequence, it can be observed that different ray-tracing programs have implemented fairly different approaches to simulate transparent material [105]. Section 3.6 covers this issue in more detail.

3.2 Reflectance models

Models for the surface reflectance of a medium can be defined in line 2 of the properties.txt file. As previously mentioned, the reflectance index of a surface can either be determined analytically or imported and interpolated from existing data files, based on more complex simulations or experiments. The following Sections, 3.2.1 through 3.2.3, cover analytical approaches, and Section 3.2.4 the data file import.

3.2.1 Fresnel

The Fresnel equations present the most common approach to determining the reflectance and transmittance coefficient at the interface between two media of different refractive indices. These equations result from the boundary condition of a balance of the electric and magnetic fields across the surface and therefore present a solution to the simplified Maxwell equations (for plane wave propagation) [55].

$$R = \left(\frac{Y_0 - Y_1}{Y_0 + Y_1}\right)\left(\frac{Y_0 - Y_1}{Y_0 + Y_1}\right)^* \tag{3.2}$$

$$T = \frac{4Y_0 Re(Y_1)}{(Y_0 + Y_1)(Y_0 + Y_1)^*} \tag{3.3}$$

Y_0 and Y_1 are the optical admittances of the respective material and depend on the polarization of the incident light. It is also common to use a modified "tilted" version of the optical admittance that incorporates the angle of propagation θ_1 inside the respective medium 1.

$$Y_1 = \begin{cases} \frac{N_1 \cos\theta_1}{Z_0} & \text{, if s-polarization (TE)} \\ \frac{N_1}{Z_0 \cos\theta_1} & \text{, if p-polarization (TM)} \end{cases} \tag{3.4}$$

with Z_0 the optical impedance of free space. TE refers to a plane wave with the electric field vector perpendicular to the plane of incidence and TM with the magnetic field vector perpendicular to the plane of incidence.

$$Z_0 = \sqrt{\frac{\mu_0}{\varepsilon_0}} \tag{3.5}$$

N is the complex refractive index

$$N = n - i\kappa \tag{3.6}$$

It should be noted that the refractive index can be complex, as is the case for non-dielectric matter such as metals. This is important for the analysis of mirrors. The refractive index and the angle of incidence are also the only non-natural constants and hence fully describe the reflectance at an interface. The angle of propagation of a medium θ_1 is related to the angle of incidence θ_0 in the first medium (generally air) by Snell's law:

$$N_0 \sin\theta_0 = N_1 \sin\theta_1 \tag{3.7}$$

3.2.2 Transfer matrix method

The material response is harder to predict if the surface of a material is covered with a coating or, in other words, if it is composed of multiple thin layers of dielectrics. A possible analytical approach to model the reflectance, transmittance, and absorptance of a thin-film assembly (coating) is the TMM. It is basically a further development of the previously described Fresnel equations. Within a layer, the electric and magnetic field is the sum of the total forward and backward (reflected) waves propagating according to a phase factor. This is illustrated in Fig. 3.4.

This assumption is described by M_r, the characteristic matrix of a thin-film layer r. Since the continuity condition of the electric and magnetic field across the boundary of the layer r and its adjacent layer also holds true here, the characteristic matrices of each layer can be multiplied. Theoretically, this can be done for a finite number q of layers. The result correlates the electric and magnetic field on top and at the bottom of the assembly (Eq. (3.8)) [55].

$$\begin{pmatrix} B \\ C \end{pmatrix} = \left\{ \prod_{r=1}^{q} \underbrace{\begin{bmatrix} \cos\varphi_r & (i\sin\varphi_r)/Y_r \\ iY_r \sin\varphi_r & \cos\varphi_r \end{bmatrix}}_{M_r} \right\} \begin{pmatrix} 1 \\ Y_m \end{pmatrix} \tag{3.8}$$

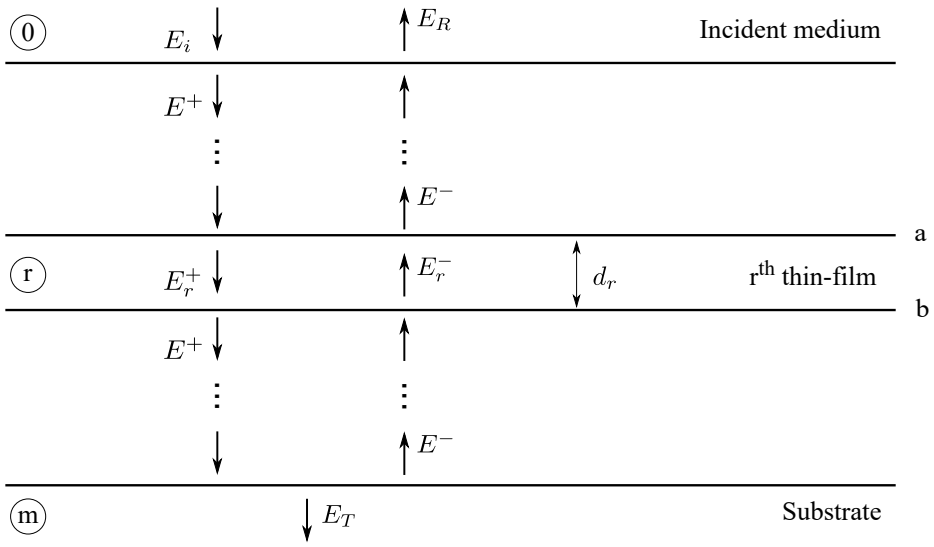

Fig. 3.4 Conservation of the electric and magnetic field of light across different interfaces of a thin-film assembly.

with a total number of layers q (including the substrate) and the optical admittance of each layer and the substrate Y_r and Y_m respectively according to Eq. 3.4. The phase factor φ_r is defined as

$$\varphi_r = \frac{2\pi N_r d_r \cos\theta_r}{\lambda} \tag{3.9}$$

From Eq. (3.8) an optical admittance of the assembly can be derived.

$$Y = C/B \tag{3.10}$$

This assembly admittance can be treated the same way as the Fresnel equations in Section 3.2.1 in order to derive the reflectance, transmittance, and absorptance of the stack.

$$R = \left(\frac{Y_0 - Y}{Y_0 + Y}\right)\left(\frac{Y_0 - Y}{Y_0 + Y}\right)^* \tag{3.11}$$

where Y_0 is the optical admittance of the incidence medium.

$$T = \frac{Re(Y_q)(1-R)}{Re(BC^*)} \tag{3.12}$$

$$A = 1 - R - T \tag{3.13}$$

The transmittance of the assembly is always independent of the direction of the propagation (propagation from the incidence medium to the substrate or from the substrate to the incidence

medium [106]). For the reflectance, however, this is only the case if absorption in the layers is ignored (only dielectric materials), which is usually satisfied for AR coatings, since here absorption is not desired. Eqs. (3.8) to (3.13) present the foundation for all thin-film performance simulations and design. Finally, it is worth noting that Snell's law at an interface between two media (Eq. 3.7) also holds for a thin-film stack:

$$N_0 \sin\theta_0 = N_r \sin\theta_r = N_m \sin\theta_m \tag{3.14}$$

AR/HR coatings: There are many ways to design AR and HR coatings. One possibility is to make them out of multiple quarter-wavelength layers. In this case the quarter-wavelength condition $\varphi = \pi/2$ has to be satisfied for each layer, so that

$$d_r = \frac{\lambda}{4n\cos\theta_r} \tag{3.15}$$

and with a successively increasing refractive index according to

$$N_r = \sqrt[r+1]{\frac{n_0}{n_{sub}}} \tag{3.16}$$

It is, however, more common in practice to use layers with alternating refractive indices. Some examples for the analytical assessment of such layers are Choi et al. [56], Mazur et al. [59], and Sahouane and Zerga [107] for solar thermal, and Saylan et al. [108] and Sikder and Zaman [109] for photovoltaic applications. Single layer AR coatings are especially needed for low-refractive materials. Porous sol-gels are also promising because the refractive index is related to the porosity [61, 63].

$$n_{ef} = [(1-p)(n^2-1)]^{0.5} \tag{3.17}$$

where p is the porosity volume fraction and n the refractive index of the base material.

Selective coatings: As described in the previous section, selective coatings are often based on dielectric-metal composites. Eqs. (3.8) to Eqs. (3.13) are only valid for layers with homogeneous properties. It is therefore necessary to approximate the effective refractive index of the composite from the refractive indices of the base materials. One way to do so is by using the Maxwell-Garnett relation.

$$\frac{\varepsilon_{ef} - \varepsilon_m}{L(\varepsilon_{ef} + \varepsilon_m)} = f \cdot \frac{\varepsilon_i - \varepsilon_m}{L(\varepsilon_i + \varepsilon_m)} \tag{3.18}$$

with the dielectric constants ε_m of the matrix, ε_i of the inclusions and ε_{ef} of the composite. f is the volume fraction of inclusion and matrix and L the depolarization factor. Some examples for the analytical analysis and design of high-temperature resistant selective thin-film assemblies using the previously described TMM are Soum-Glaude et al. [64], An et al. [65], Rebouta et al. [67], Hernández-Pinilla et al. [68], Cardenas [110], and Yang et al. [111].

3.2.3 Analytical $R(\theta)$-functions

Several expressions have been suggested in the literature to make meaningful assumptions with regard to the surface reflectance as a function of incidence angle. The main advantage of these models is that they depend on a limited set of material-specific coefficients irrespective of the complexity of the assembly. Using this method, numerous multi-layer stacks of advanced HR, AR, or selective coatings could be modeled with little or no additional input apart from the constant reflectance value R_0 at normal incidence. The use of an analytical expression over a lookup table can reduce the memory footprint of software. The following models have been proposed in different literature:

Grena [112]:

$$R(\theta) = R_0 + (1 - R_0)\left(\frac{2\theta}{\pi}\right)^8 \tag{3.19}$$

Tesfamichael and Wäckelgård [81]:

$$R(\theta) = R_0 + b(1 - R_0)\left(\frac{1}{\cos\theta} - 1\right)^c \tag{3.20}$$

Hess [99]:

$$R(\theta) = R_0 + \tan\left(\frac{\theta}{a}\right)^{\frac{1}{b}} \tag{3.21}$$

Schlick [113]:

$$R(\theta) = R_0 + (1 - R_0)(1 - \cos\theta)^5, \text{ with } R_0 = \left(\frac{n_0 - n}{n_0 + n}\right)^2 \tag{3.22}$$

Lazányi and Szirmay-Kalos [114]:

$$R(\theta) = R_0 + (1 - R_0)(1 - \cos\theta)^5 - a\cos(\theta)(1 - \cos\theta)^b, \text{ with } R_0 = \frac{(n_0 - n)^2 + \kappa^2}{(n_0 + n)^2 + \kappa^2} \tag{3.23}$$

Lazányi (modified):

$$R(\theta) = R_0 + (1 - R_0)(1 - \cos\theta)^c - a\cos\theta(1 - \cos\theta)^b \tag{3.24}$$

Eq. (3.19) was derived from experiments on different types of cermet-based solar absorbers (not mentioned). Eq. (3.20) is based on experiments on Ni-Al_2O_3 and Ni-NiO_x assemblies; Eq. (3.21) on a gradient Al-Al_2O_3 coating with a sputtered Al_2O_3 layer on top. The other formulas were taken from a computer graphics background. Nevertheless, all models can be useful to simulate the solar-weighted reflectance behavior of any type of material. Eqs. (3.23) and (3.24) represent the reflectance of metal surfaces such as mirrors.

3.2.4 File import

Reflectance data files can originate from experimental data acquisition or from optical simulations. The interpolation from data arrays instead of solving complex analytical expressions can save CPU time but comes at the cost of a larger memory footprint. The total λ-θ-data grid is restructured and stored in columns in the following order:

- Reflective materials: $\lambda/\theta/R$
- Refractive materials: $\lambda/\theta/R_\perp/R_\parallel$

The interval of the wavelength λ is [285, 4000] nm with step size 5 nm, which is similar to the reference solar spectrum provided by NREL [115]. Incidence angle values θ reach from 0° to 90° with step size 2° in order to cover the entire hemisphere of the sample.

It is also important to note that, in the case of refractive materials, the incidence angle always refers to the angle on top of the sample, even if it has previously been traced and calculated from the inside (back side). This is essential to be consistent with the total reflectance condition. The relationship between the incidence angle on the front and back side of an interface is given by Snell's law(Eq. (3.7)).

Finally, it is apparent that the file format for refractive materials is different to the format for reflective materials. This is due to the fact that the reflection on a refractive surface is polarizing by nature. This can also be derived from the different optical impedances in Eq. (3.4). It is therefore necessary to state the reflectance value of both perpendicular and parallel polarized light.

3.3 Polarization

Since the overall reflectance and transmittance of a transparent medium, such as glass, is the result of a series of reflections within the medium, the polarization effect is further intensified. In ray-tracing, this effect is only represented properly if s- and p-polarized light are treated separately, because the surface reflectance is different for s-polarized ($R_\perp$) and p-polarized ($R_\parallel$) incident light. The most common approach in ray-tracing simulations to model the effect of unpolarized sunlight is to assign a mean reflectance value to a refractive surface [116]:

$$R = 0.5(R_\perp + R_\parallel) \tag{3.25}$$

It can be observed that, in the case of refractive materials, using the mean value does not lead to correct results for larger incidence angles, where $R_\perp$ and $R_\parallel$ are significantly different. Therefore, OTSun uses a different approach. Here, rays are emitted with alternating s- or p-polarization at the light source. When a ray intersects with a refractive surface, the assigned polarization state determines whether to call a function for $R_\perp$ or $R_\parallel$. The difference in outcome between both approaches is seen in Fig. 3.5. The transmittances have been simulated for a glass plate with a refractive index of $n = 1.5$ and without absorption. A difference of more than 2 % can be observed for incidence angles around 70°.

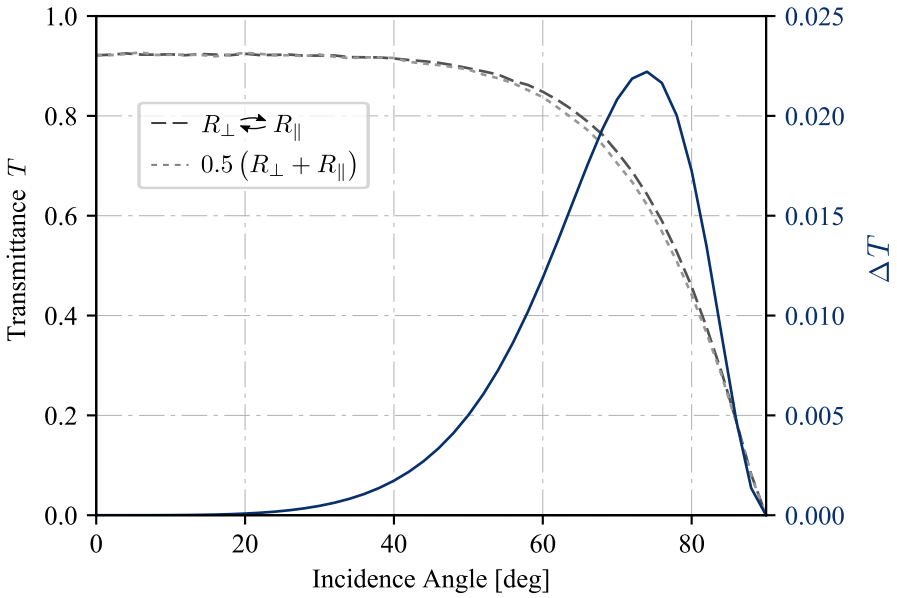

Fig. 3.5 Transmittance of a glass plate with refractive index of $n = 1.5$ based on ray-tracing simulations. The surface reflectance was first modeled as the mean $0.5(R_\perp + R_\parallel)$ and then as an alternating $R_\perp$ or $R_\parallel$ depending on the randomly generated polarization state of the incident ray.

Interestingly, Duffie and Beckman [38] provide an analytical model for a single glass layer, which is in perfect accordance with the ray-tracing results generated by OTSun. However, the analytical model provided for multiple layers, which seem to yield the same results as a simplified TMM analysis, vary significantly from those generated by OTSun. The higher the number of layers, the larger the differences, especially for high angles of incidence. This issue is addressed in Appendix A.

3.4 Scattering models

Scattering is another important phenomenon of radiation-matter interaction on a surface. While reflection is the result of an energetic balance, scattering is due to surface texture. The microscopically random surface structure influences the direction of the reflected light and disperses the energy flux spatially (Fig. 3.6).

In general, it is possible to distinguish between two ideal cases of reflection: isotropic reflection (maximum scattering) and specular reflection (no scattering). In reality, the reflection pattern lies somewhere between both cases and is described by a BRDF function. BRDFs can be provided either as analytical functions or as a data file based on experiments. Many different BRDFs have been proposed to meet the many different surface types [117].

From the perspective of Monte Carlo ray-tracing, it is necessary to express the direction of reflection in terms of probabilities. Isotropic, or Lambertian, reflection in this regard is the simplest case, since the probability for each direction of reflection is the same. This is the case for very rough or matte surfaces.

3.4.1 Gaussian scattering

In simulations of solar thermal applications, specular reflection is commonly represented by a Gaussian distribution. Eq. (3.26) shows a general and well-established probability density function for solar thermal simulations.

$$f = K_\sigma e^{-\left(\frac{\varphi^2}{2\sigma_{21}^2}+\frac{\varphi^2}{2\sigma_{22}^2}\right)} + (1-K_\sigma)e^{-\left(\frac{\varphi^2}{2\sigma_{11}^2}+\frac{\varphi^2}{2\sigma_{12}^2}\right)} \tag{3.26}$$

with φ the aperture area of the integrating sphere indicated in Fig. 2.8, σ the variance of the scattering in each respective orthogonal direction, and K_σ the weighting factor of the superposition of both Gaussian curves (usually a narrow and broad one). Eq. (3.26) essentially incorporates four basic cases of Gaussian specular reflection.

- Single univariate ($K = 0$, $\sigma_{11} = \sigma_{12}$)
- Single bivariate ($K = 0$, $\sigma_{11} \neq \sigma_{12}$)
- Double univariate ($K \neq 0$, $\sigma_{11} = \sigma_{12}$, $\sigma_{21} = \sigma_{22}$)
- Double bivariate ($K \neq 0$, $\sigma_{11} \neq \sigma_{12}$, $\sigma_{21} \neq \sigma_{22}$)

The implementation of Eq. (3.26) is described in Appendix B. Figure 3.6 shows an example of a double Gaussian scattering pattern. The multivariate Gaussian function accounts for a preferred reflection direction, which in reality appears in reflective material. It is caused by the respective processing method, as for example the rolling process in the manufacturing of aluminum mirrors. The superposition of two Gaussian distributions better represents the combined effect of specular and non-specular reflection.

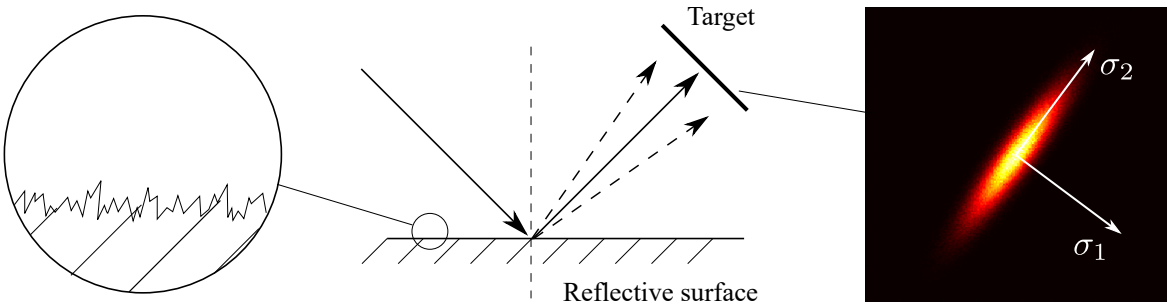

Fig. 3.6 Microscopic surface errors lead to narrow-angle scattering of specular reflection (left). Reflection pattern on target (right).

It is important to state that the scattering itself depends on the wavelength and the angle of incident light as well ($\sigma = \sigma(\lambda, \theta)$). This dependency significantly varies according to the material type [76, 80]. Since there is still no standardized experimental method for the complete spectral assessment of specular material [118], little can be found on wavelength and incidence angle dependency of the variance σ. One of the few suggestions is the power law proposed by Good et al. [76], shown in Eq (3.27)

$$\sigma(\lambda, \theta) = \sigma(\lambda_{ref}, \theta_{ref}) \cdot \left(\frac{\lambda}{\lambda_{ref}}\right)^{p} \left(\frac{\cos\theta}{\cos\theta_{ref}}\right)^{q} \tag{3.27}$$

A common approach to incorporate macro errors in ray-tracing simulations is to convolute all macroscopic errors to a single variance as if they were all Gaussian distributed [79].

$$\sigma^2_{macro} = \sum_{i=1}^{n} \sigma^2_{spec} + 4\sigma^2_{slope} + \sigma^2_{align} + \sigma^2_{track} \tag{3.28}$$

It is worth noting that if the specular error represents a superposition of two Gaussian distributions, following the convolution approach, the overall scattering profile of the specular and macro errors is given by

$$f = K_\sigma e^{-\left(\frac{\varphi^2}{2\left(\sigma_{macro}^2+\sigma_1^2\right)}\right)} + (1-K_\sigma)e^{-\left(\frac{\varphi^2}{2\left(\sigma_{macro}^2+\sigma_2^2\right)}\right)} \tag{3.29}$$

3.4.2 Total integrated scattering

Even though in simulations of solar thermal applications the TIS model does not play an important role, it is worth mentioning. The TIS probability function is one of the oldest. It was originally developed to achieve a better understanding of radar scatter from rough surfaces but is also used for the qualification of photovoltaics [119]. There are also endeavors to establish the TIS as a model for solar thermal applications. Montecchi [75] proposes the use of Eq. (3.30) to model the specular reflectance of commercial first-surface mirrors (aluminum and polymer mirrors). In Montecchi [120] the same author emphasizes the need for an alternative parameter, based on the TIS model, for the near-specular solar reflectance.

$$\frac{R_s(\lambda,\theta,\phi)}{R_h(\lambda,\theta,h)} = \exp\left[-\left(\frac{4\pi\sigma_\phi\cos\theta}{\lambda}\right)^2\right] \tag{3.30}$$

where R_s is the spectral reflectance, R_h the hemispherical reflectance, and σ_ϕ the equivalent-roughness. Montecchi [75] treats σ_ϕ as a heuristic parameter instead of as a physical characteristic of the surface. The parameter follows Eq. (3.31)

$$\sigma(\varphi) = A_1\exp\left[-(\varphi/\sigma_1)^2\right] + A_2\exp\left[-(\varphi/\sigma_2)^2\right] \tag{3.31}$$

One advantage of Eq. (3.30) is that it already provides an analytical relationship between specular scattering and the wavelength of the incident light. This model has still not been implemented in OTSun but shall be in the near future.

3.5 Volume effects

While Sections 3.2 through 3.4 covered effects that occur when light is incident on a surface between two media, several phenomena can be observed when light propagates through a medium. Figure 3.3 only illustrates the most common: bulk scattering and extinction. Bulk scattering can be important if the medium contains particles or inclusions as, for example,

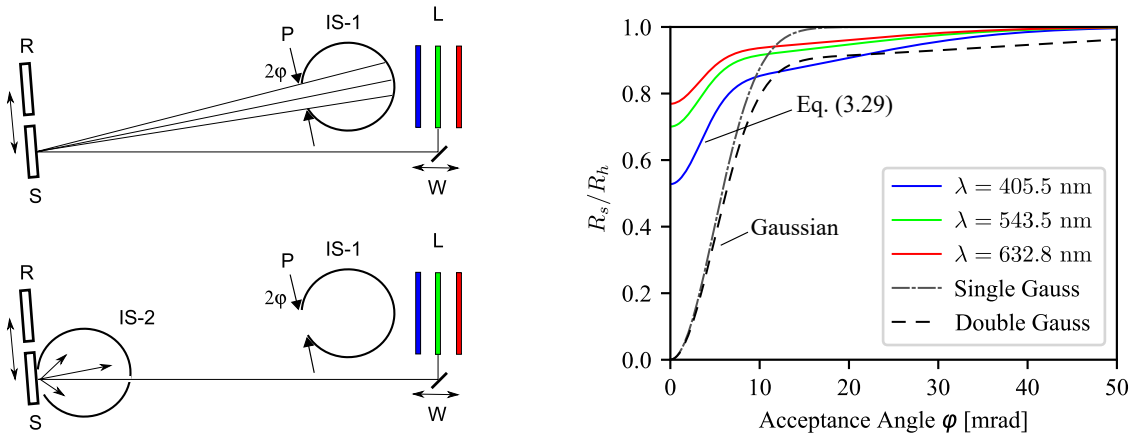

Fig. 3.7 TIS scattering. Left: Experimental setup of Montecchi [75] to measure R_s and R_h for different wavelengths. Right: comparison of TIS and Gaussian scattering patterns for $\sigma_1 = 4.9\,\text{mrad}$ and $\sigma_2 = 36\,\text{mrad}$ representing an aluminum mirror.

in the case of Cai et al. [121]. It can also play an important role in polymeric material or atmospheric calculations such as for solar tower applications [52]. If the medium is mainly homogeneous, however, bulk scattering in comparison to surface scattering is rather small and absorption will have most influence on the radiation intensity [122]. That is why OTSun only considers the absorption in a medium according to the Beer–Lambert law:

$$\frac{I}{I_0} = e^{-\alpha d} \tag{3.32}$$

where α is the absorption coefficient of the medium and d is the propagated path length of the light through the medium. The absorption coefficient α is correlated with the extinction coefficient κ – the complex part of the refractive index of a material (Eq. (3.33)).

$$\alpha(\lambda_0) = \frac{4\pi\kappa}{\lambda_0} \tag{3.33}$$

where λ_0 is the vacuum wavelength. A rough relation between a material's absorption and the wavelength can be obtained by an exponential Urbach fit. However, this approximation is not accurate in all cases [52].

In order to move from experimental data to usable input for ray-tracing, one challenge is to separate between volume and surface effects, as in reality they can only be measured together. This was also pointed out by the work of Good et al. [123] and Wallner et al. [122].

3.6 Combined surface reflectance and volume models

As the previous analysis implies, the overall optical property of a transparent medium is the result of the coupled effect of reflections, refraction, and absorption between two refractive surfaces. Especially in terms of ray-tracing, it is challenging to reconcile the parameter input with experimental results, since the volume can only be measured as a whole. Consequently, it can be difficult to report to which extent this value originates from the effects at the surface or in the volume. Many different models for refractive material have been implemented in current ray-tracing programs [105]. Different transparent models have been simulated and compared in Section 4.4.3.

3.7 Spectral sun model

The model of the sun is a core part of the ray-tracing simulation. The light source is the starting point of each tracing loop initiated by emitting a ray with specific characteristics. The principle physical properties of a ray are: a propagation vector of the wave front (direction), wavelength, and polarization. Each one of these properties is invoked randomly based on specific underlying probability density functions (PDFs).

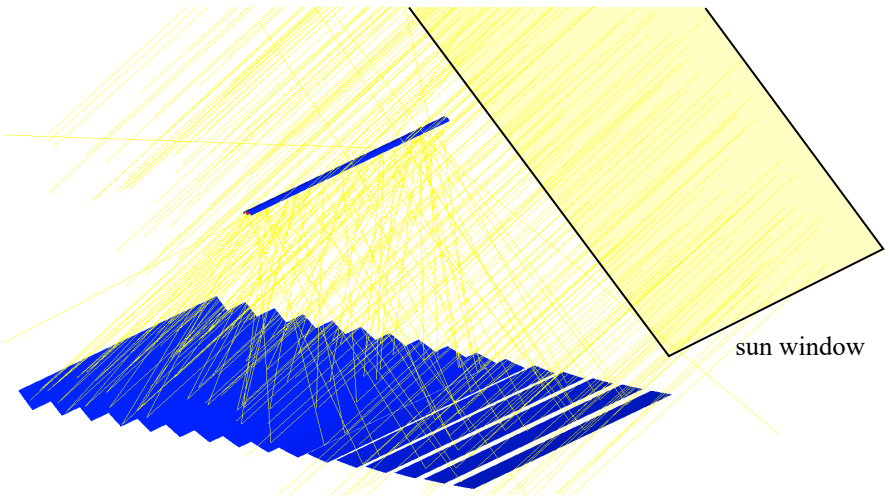

Fig. 3.8 The sun window is the geometrical origin for the randomly generated rays.

Direction: The direction or angle of a ray depends on the probability of emission for different regions of the solar disc. Is it more likely for a ray to be emitted at the center of the solar disc (small angle) or the outskirts of the solar disc (large angle)? The probability of the occurrence of each angle can be described by the PDF found in Eq. (3.34). This PDF can be

found in Pujol-Nadal [124] and represents the sun model proposed by Buie et al. [125].

$$F(\theta) = \begin{cases} a_1 2\pi \int_0^{\theta} \frac{\cos(0.326\theta')}{\cos(0.308\theta')} \theta' d\theta' & \text{if } 0 \leq \theta < 4.65 \\ \frac{a_2 2\pi e^k}{\gamma+2} \left(\theta^{(\gamma+2)} - 4.65 \right) & \text{if } 4.65 \leq \theta \leq 43.6 \end{cases} \tag{3.34}$$

where θ is the sun angle with respect to the center of the sun disk. a_1 and a_2 are

$$a_1 = \frac{1 - \text{CSR}}{2\pi \int_0^{4.65} \frac{\cos(0.326\theta')}{\cos(0.308\theta')} \theta' d\theta'} \tag{3.35}$$

$$a_2 = \frac{\text{CSR}}{2\pi e^k \int_{4.65}^{43.6} \theta'^{(\gamma+1)} d\theta'} \tag{3.36}$$

and CSR is the Circumsolar Ratio according to Eq. (3.37), the fraction of total emitted energy that originates from the region around the solar disk.

$$\text{CSR} = \frac{I_{CS}}{I_D + I_{CS}} \tag{3.37}$$

This CSR is caused by scattering phenomena in the atmosphere and is highly dependent on the weather conditions. Figure 3.9 shows the Buie distribution for different CSRs. There is also the option to select the "point source" model, in which case the sun angle would be zero all the time, because the sun disc is assumed to be reduced to a single point. This is useful for more hypothetical simulations or to analyze the influence of the collector components separately.

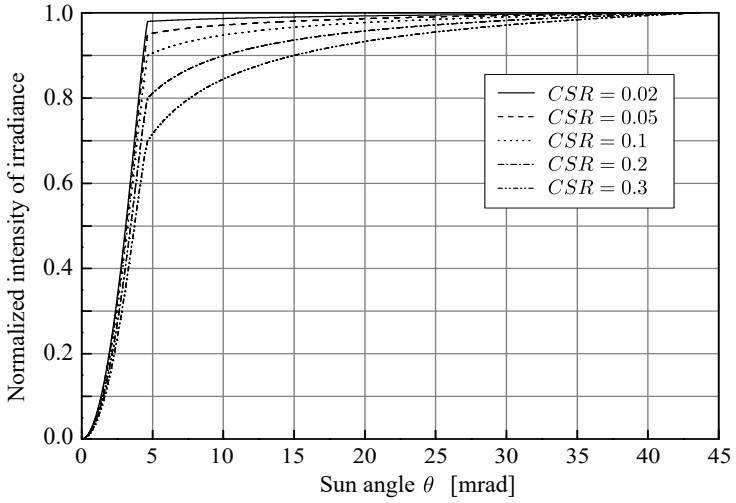

Fig. 3.9 Buie distribution of different circumsolar ratios.

Wavelength: The probability density function for the wavelength of the ray has been derived from the reference AM 1.5 solar spectrum provided by NREL [115]. Figure 3.10 shows the reference spectrum and its corresponding PDF, which is the cumulative function of the spectrum.

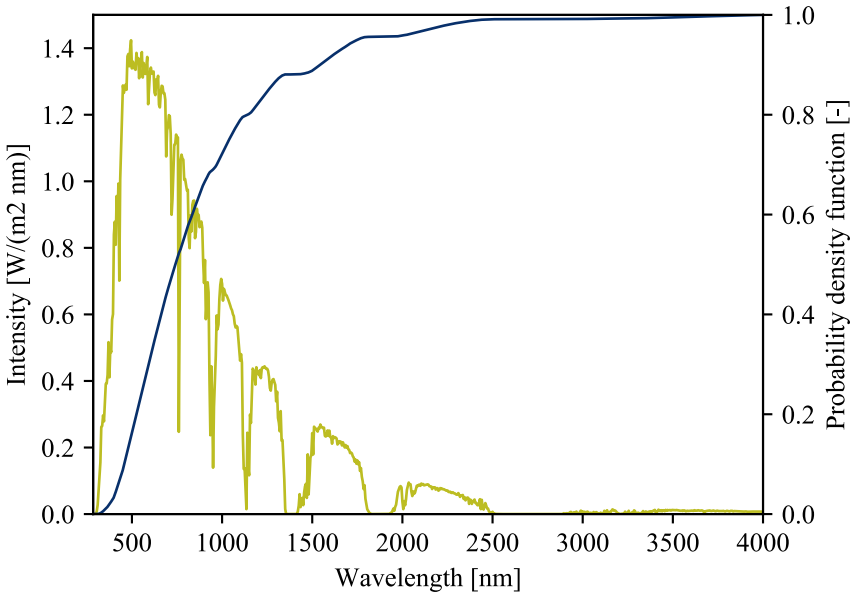

Fig. 3.10 The reference AM 1.5 solar spectrum and its corresponding probability density function.

Polarization: As for the polarization: Unpolarized light is assumed, which is common for solar irradiance. In this respect "unpolarized" means that any orientation of the polarization vector is equally likely to occur.

3.8 Tracking

Currently OTSun provides three different tracking modes, as seen in Table 3.1:

- static
- linear
- CCStar

The required tracking mode has to be defined under "mechanical parameters" in line 28 of the properties.txt file of each respective collector component, for example, a mirror row of a Fresnel collector. If the tracking mode is "static" (no tracking at all), no additional parameters are required. In the case of "linear" or "CCStaR" tracking, Table 3.1 lists the parameters the user is required to provide.

Linear tracking: For linear tracking, the required parameters are the origin and local coordinate system of each adjustable component, the axis of rotation, and the focal point. The rotation angle θ_{track} is the angle between the original surface normal and the angle bisector between the projected sun angle vector and the focus vector. This relation is illustrated in Fig. 3.11 for the example of a single Fresnel mirror row. In the case of rotation around the x-axis, the rotation matrix would result in a rotation matrix around α

$$L_\alpha = \begin{pmatrix} 1 & 0 & 0 \\ 0 & \sin(\theta_{tr}) & -\sin(\theta_{tr}) \\ 0 & \sin(\theta_{tr}) & \cos(\theta_{tr}) \end{pmatrix} \tag{3.38}$$

Finally, to re-orientate the object, all of its vertices have to be multiplied by the rotation matrix

$$\boldsymbol{x}' = L_\alpha \boldsymbol{x} \tag{3.39}$$

CCStar tracking: The linear tracking system of the CCStaR collector is different from the conventional approach as it consists of static mirror rows and moves the absorber tube instead of tracking the sun light. This mechanism is illustrated in Fig. 3.11.

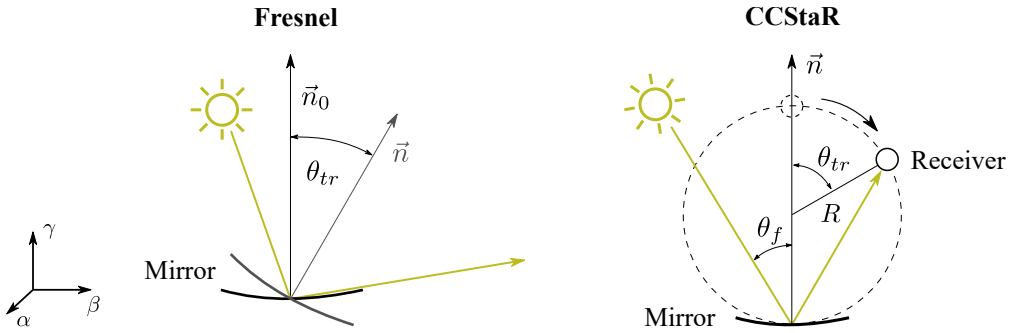

Fig. 3.11 CCStaR and Fresnel collector-specific tracking.

The rotation angle θ_{track} to position the absorber tube in the focus is twice the angle θ_f between the surface normal $\vec{n}$ and the projected reflection vector $\vec{v}_{ref}$. This yields the updated receiver position according to Eqs. (3.40) and (3.41)

$$x_f = R\sin(2\theta_{tr}) \tag{3.40}$$

$$z_f = R(1+\sin(2\theta_{tr})) \tag{3.41}$$

3.9 Conclusions

In this chapter a powerful ray-tracing software for accurate optical simulations has been presented. The program is based on the original OTSun code and has been developed further to meet the objectives of this thesis. The current version allows to choose from a great variety of optical models. Table 3.4 shows how OTSun compares to other ray-tracing programs.

Table 3.4 Features of different ray-tracing programs

Software	License	System		Optical properties					Light source		
		Geometry	Tracking	$R(\theta)$	$R(\lambda)$	TMM	κ	σ	Sun shape	Spectrum	Polarization
		Embedded CAD		Incidence angle dependency of reflectance	Wavelength dependency of reflectance	Embedded TMM algorithm	Gradual absorption in glazing	Scattering profiles	Which sun models?		s/p-polarization in source
OTSun	Free	via stl-file import	line-focused CCStar	×	×	×	×	2 bivariate Gaussians	Point Buie	AM 1.5 User defined	×
Tonatiuh	Free	predefined elements	line focused					1 univariate Gaussian	Pillbox Buie		
SolTrace	Free	predefined elements	line focused point focused	×			planned	1 univariate Gaussian Pillbox	Point Pillbox User defined		
CROWN	Commercial	periodic textures via $z(x,y)$-file		×	×	×	×		Point	User defined	×
SimulTrough	Free	only parabolic troughs		×	×		×	1 bivariate Gaussian Fourier harmonics	Winter et al. [126]	1.5 AM	
OptiCAD	Commercial	predefined elements		×	×		×	User defined	User defined	User defined	User defined

Chapter 4

Ray-tracing sensitivity analysis

4.1 Background

Statistical ray-tracing algorithms have become popular to assess the optical performance of concentrating solar collectors [127, 128]. These algorithms apply geometrical optics, which means that they provide solutions of the simplified Maxwell equations for plane-wave propagation and homogeneous, isotropic optical material properties.

Nowadays, ray-tracing simulations are mainly applied to deal with design and optimization problems [127, 129], but they can play an important role in other fields as well. For example, in the IEA Solar Heating and Cooling Task 49 (Solar Process Heat) it has recently been suggested to include ray-tracing results in the standardized collector testing procedure [32], an idea that is also being followed up on in the current IEA Task 57 [36]. One of the most recent studies on this topic is Osório et al. [105], where a ray-tracing round robin was carried out among many Task 49 participants in an attempt to better compare and characterize statistical simulation tools.

A key problem with the study of Osório et al. is that all participants used their own specific open source or commercial ray-tracing codes, each one relying on a very different set of optical models. As such the comparison lacks a common basis to start from, which makes it almost impossible to clearly pinpoint the influence of different parameters on the simulation result.

Another problem is that especially open source programs, which enjoy great popularity among the scientific community, were released many years ago and not all of them have been updated accordingly to make use of the newly available data input provided by solar material

research centers and manufacturers. Especially surface-treated materials are challenging in this respect [60, 130]. This issue was also discussed in Hertel et al. [131].

4.2 Objectives

Especially with regard to recent developments of solar materials, the key optical properties that should be defined in ray-tracing simulations of solar thermal collectors, have still not been sufficiently identified. This study aims to shed new light on this question by looking most of all into the influence of incidence-angle- and wavelength-resolved simulations using the OTSun ray-tracing code (Chapter 3).

4.3 Reference case

In this study, we chose a LFC as a test case. The geometry was first presented by Horta and Osório [132] and then further analyzed in their round robin [105]. As shown in Fig. 4.1, the collector consists of 16 slightly parabolically shaped heliostats with a width of 0.75 m. The absorber tube has a diameter of 35 mm and it is positioned at 7.4 m above the heliostat rows. It is covered with a 5 mm-thick borosilicate envelope. A CPC-shaped secondary reflector helps in improving the performance of the collector. Its length is 120 m.

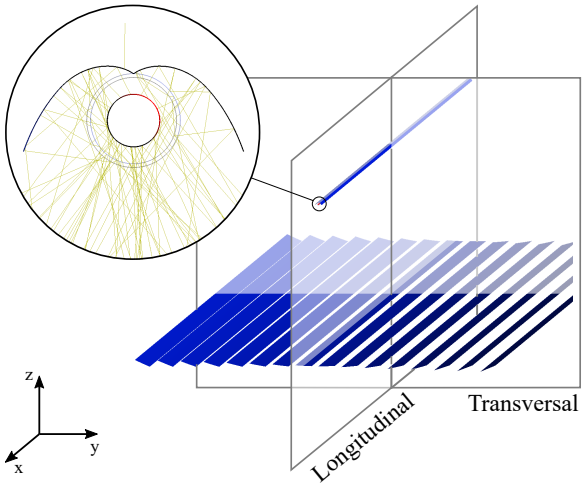

Fig. 4.1 LFC geometry that was analyzed in this study.

The objective of this study is to carry out a sensitivity analysis using assumptions as accurate as possible, considering both wavelength- and incidence-angle-dependent optical properties. It is difficult to find such detailed information in the literature as the assessment

is either technically not yet possible or there is still no standardized measurement technique available. The below-presented optical properties of the materials of the collector are a collection of accurate analytical models taken from different studies. All reflectance data were obtained through a preprocessing step by using the TMM for thin films as described in Section 3.2.2.

4.3.1 Mirror

The thin-film structure of the mirror considered in this analysis was presented by Sutter et al. [58]. The model presents an aluminum mirror with a HR coating. The coating is an assembly of quarter-wavelength dielectric layers with alternating high and low refractive indices. The thick top layer of porous SiO_2 makes the mirror more durable against environmental impacts. Figure 4.2 shows an exemplary cross-sectional curve of the characteristic reflectance surface $R(\lambda, \theta)$ for normal incidence.

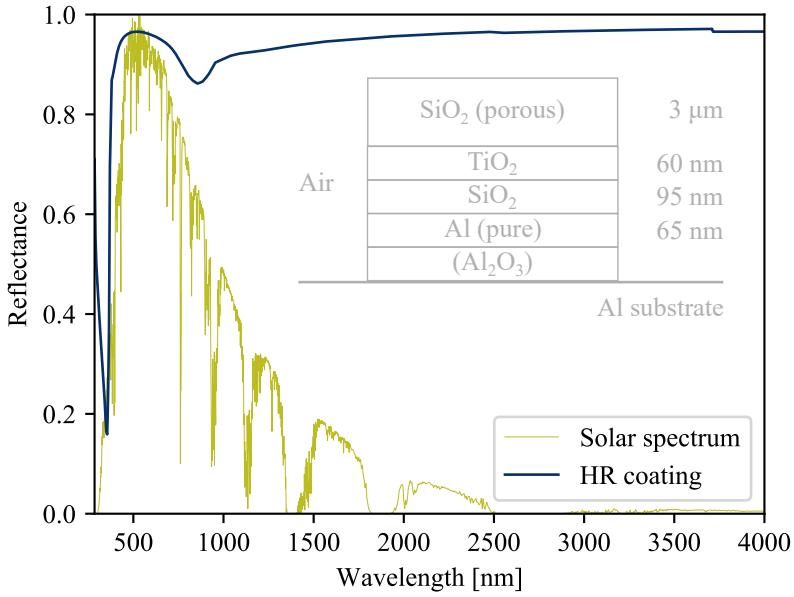

Fig. 4.2 Thin-film assembly of the HR of the mirror and an exemplary cross-sectional curve of its TMM reflectance surface $R(\lambda, \theta)$ at normal incidence.

Generally, the model proposed by Pettit (Eq. (3.26)) is acknowledged when the scattering of specular solar mirrors is considered. A single Gaussian curve represents a good model to describe the scattering profile of glass mirrors [77]. On the other hand, the more complex bivariate double Gaussian shape of the scattering pattern is more generic to recent mirror technologies such as polymer or aluminum mirrors [79, 123], because of their rougher surface structure and/or milling marks originating from the manufacturing process. Detailed optical

parameters to describe the bivariate scattering pattern can hardly be found in the literature. Sutter et al. [80] determined deviations for both σ_1 and σ_2.

In practice, not only the total intensity of the reflected light $R_h(\lambda, \theta)$, but also the variances σ of the scattering change with different wavelengths and incidence angles. To model this dependency, we adopted Good's model for our ray-tracing calculations but slightly extended it to obtain data points for all possible combinations of λ and θ (Eq. (3.27)).

Validating Eq. (3.27) with $\sigma(\lambda, \theta)$ sample points from Good et al. [123] showed that the error range for $\Delta\sigma = \sigma_{fac} - \sigma_{exp}$ is of the same magnitude as the one-dimensional power-law fits themselves. This is illustrated in Fig. 4.3. The parameters presented in Table 4.1 were measured by Good et al. for an HR-coated aluminum mirror sample.

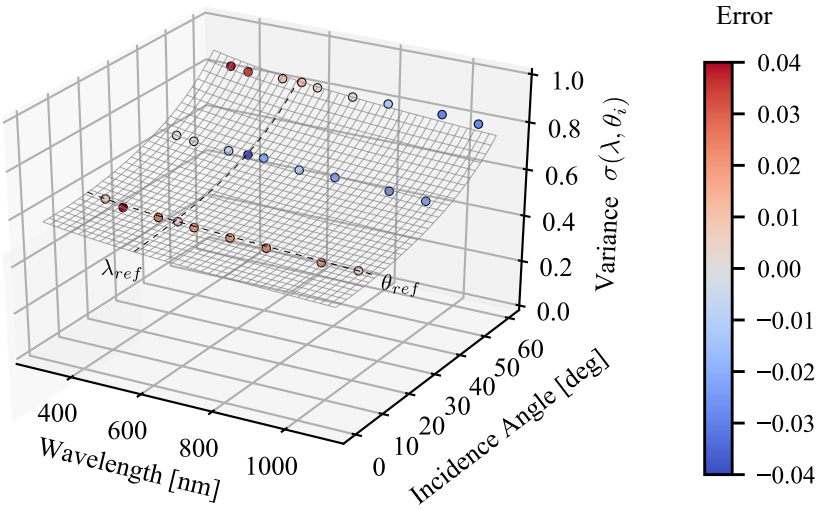

Fig. 4.3 Measured points versus the analytical factorization model for the variance of specular scattering. Good et al. [123] proposed a power law to describe the curves along the $\lambda_{ref} = 555\,\text{nm}$ and $\theta_{ref} = 15°$ directions, respectively.

In addition to the specular scattering, it is common to include structural and operational surface errors, such as slope deviations, receiver misalignment, or tracking errors, in the Gaussian error model. One approach is to convolute all these macroscopic errors with the specular errors to a single variance as if they were all Gaussian distributed [79] (Eq. (3.28)). σ_{mac}-values for the simulations presented in Table 4.1 were taken from Zhu and Lewandowski [133] and Zhu [134].

4.3.2 Absorber

The model of the absorber has been analyzed in An et al. [65] and is shown in Fig. 4.4 together with its TMM reflectance curve at normal incidence. The thin-film assembly describes a high-temperature spectrally selective coating with two solar light absorbing layers deposited on an infrared reflecting molybdenum buffer layer. The additional Si_3N_4 dielectric on top works as an AR layer. The whole assembly has been sputtered on a stainless steel substrate.

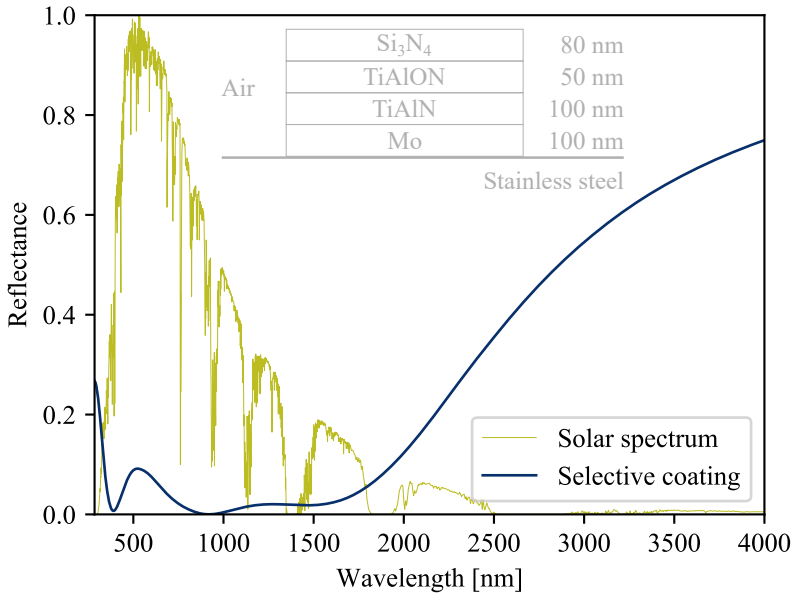

Fig. 4.4 Thin-film assembly of the absorber and exemplary cross-sectional curve of its TMM reflectance surface $R(\lambda, \theta)$ at normal incidence.

4.3.3 Envelope

The envelope consists of borosilicate glass (Schott N-BK7) with a single MgF_2 quarter-wavelength AR layer corresponding to a reference wavelength $\lambda_0 = 550\,\text{nm}$ of free space. A similar glass model was also simulated in Grena [112], however, it didn't take into account the wavelength dependency as illustrated in Fig. 4.5.

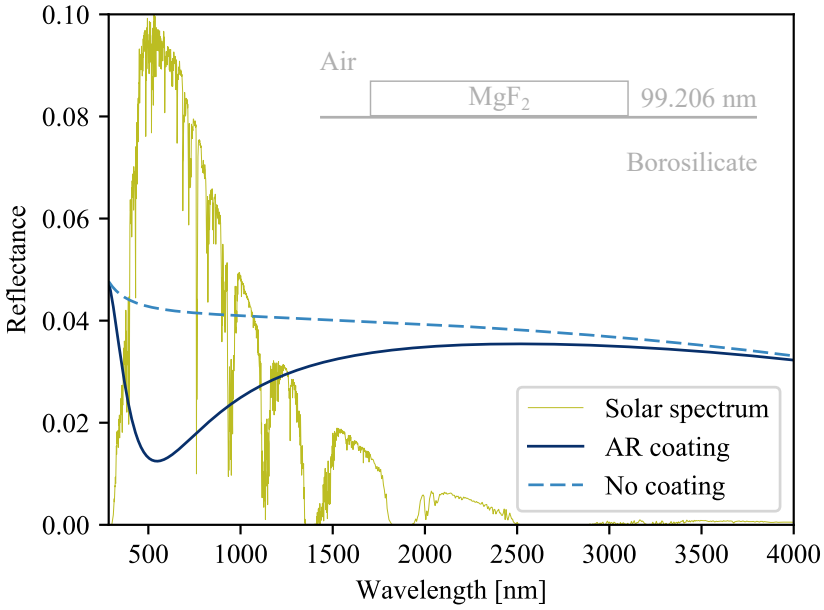

Fig. 4.5 AR layer on the glass and exemplary cross-sectional curve of its TMM reflectance surface $R(\lambda, \theta)$ at normal incidence.

Table 4.1 shows a summary of all reflectance and scattering models together with the parameters that are defined for each respective surface type. Refractive index data were obtained either from the Filmetrics [135] or the RefractiveIndex [136] database.

Table 4.1 Reflectance/scattering models and parameters for each respective surface type of the collector model as they were chosen for the sensitivity analysis reference case.

Surface Type	Reflectance		Scattering	
	Model	Parameters	Model	Parameters
Mirror	TMM [58]	Refractive index database [135, 136]	Specular Power law $\sigma_{\parallel}$ (parallel)	$\lambda_{ref} = 555$ nm $\sigma_{ref} = 0.53$ $p = -0.12$ $q = -0.61$
			Specular Power law $\sigma_{\perp}$ (perpendicular)	$\lambda_{ref} = 555$ nm $\sigma_{ref} = 0.29$ $p = -0.81$ $q = -0.57$
			Macro-errors	$\sigma_{mac,\parallel} = 2.5$ mrad $\sigma_{mac,\perp} = 3.35$ mrad
Absorber	TMM [65]	Drude-Lorentz and Tauc-Lorentz parameters from [65]	Lambertian	None
Glass	TMM (MgF_2-layer)	Refractive index database [135, 136]	None	None

4.4 Methodology

In this study, we used the in-house Monte Carlo ray-tracing tool OTSun described in Chapter 3. In OTSun fully describes the optical properties of materials by defining its reflectance and scattering profile at the surface and absorption in the volume. Reflectance characteristics can either be defined by hard coded analytical functions or via data-file import, e.g., based on pre-processed TMM optical analysis, in order to account for more complex phenomena such as coatings. Figure 4.6 gives an overview of the sensitivity analysis, which has been carried out. It consists of three parts: The comparison between wavelength-resolved, angle-resolved and constant parameter simulations (Section. 4.4.1), a methodology to recover incidence angle dependency by using analytical expressions, when only constant input is available (Section 4.4.2) and a comparison of different refractive models for the glass cover (Section. 4.4.3).

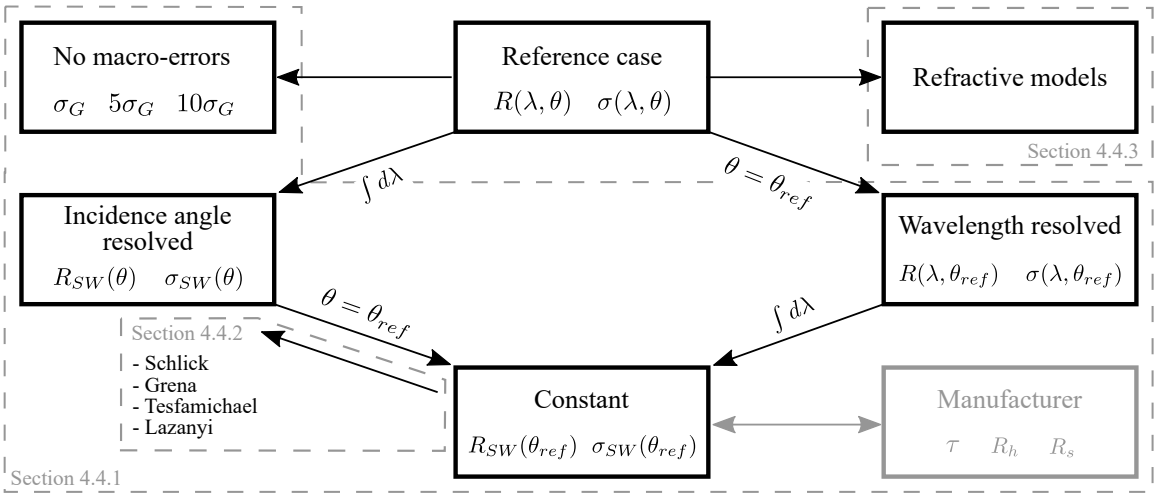

Fig. 4.6 Overview of the simulation cases. Surface reflectance and scattering can depend on the incidence angle and the wavelength.

4.4.1 Incidence-angle-resolved versus wavelength-resolved simulations

The primary objective of this study was to discuss the importance of reflectance and scattering data that solely depend on the incidence angle (incidence-angle-resolved), on the wavelength (wavelength-resolved), or on neither of them (constant). At first sight, using merely constant parameters for simulations does not seem appropriate for accurate simulations, however, in practice it is often the only data provided by the manufacturer. For example, the complex specular characteristics of a mirror are described by a hemispherical (R_h) and a specular (R_s)

reflectance value, and transparent materials are characterized by a single transparency or a haze value.

Starting from the most accurate case — the reference case described in Section 4.3 — there are three methods to obtain the incidence-angle-resolved data:

$$f_{SW}(\theta) = \frac{\int f(\lambda,\theta)s(\lambda)d\lambda}{\int s(\lambda)d\lambda} \tag{4.1}$$

$$f(\theta) = f(\lambda_{sw},\theta), \text{ with } \lambda_{SW} = \frac{\int \lambda s(\lambda)d\lambda}{\int s(\lambda)d\lambda} \tag{4.2}$$

$$f(\theta) = f(\lambda_{max},\theta) \tag{4.3}$$

where $s(\lambda)$ is the solar spectrum and λ_{max} is the wavelength at the maximum of the solar spectrum. For our ray-tracing simulations, there are three relevant parameters to completely describe a material: the surface reflectance, the surface scattering, and the refractive index of the medium. It has been observed that the best results are achieved by applying Eq. (4.1) to the surface reflectance and by applying Eq. (4.3) to the refractive index and scattering data. This is concluded from a short preliminary study, where the incidence-angle-resolved case is compared with the full parameter case using all possible combinations of Eqs. (4.1) to (4.3). The wavelength-resolved data is based on a reference at normal incidence $\theta_{ref} = 0$.

4.4.2 Recover incidence angle dependency

In ray-tracing simulations it is often very important to know in which way the reflectance of a material depends on the angle of the incident light. The approach in this section makes use of the models in Section 3.2.3 to approximate the incidence angle dependency of the reflectance when only constant values are available.

Figure 4.7a and b show that Eqs. (3.19), (3.20) and (3.22) are in fairly good agreement with solar-weighted reflectance data for the glass and the absorber. The model of Tesfamichael predicts the trend of the curve despite the fact that its parameters refer to $Ni - Al_2O_3$ and $Ni - NiO_x$ assemblies. However, it is less accurate for angles more than 80°. Figure 4.7c demonstrates that all these models perform poorly for metal surfaces with a complex refractive index. For a better representation of metals, Lazányi and Szirmay-Kalos [114] proposed a variation of Schlick's model. We observed that by further modifying this approximation, adding to it one more degree of freedom (parameter "c"), results could be substantially

improved. This is illustrated in Fig. 4.7d, which shows the best fits of Eq. (3.24) for two first-surface reflectors (Ag and Al) and the HR coating described in Section 4.3.

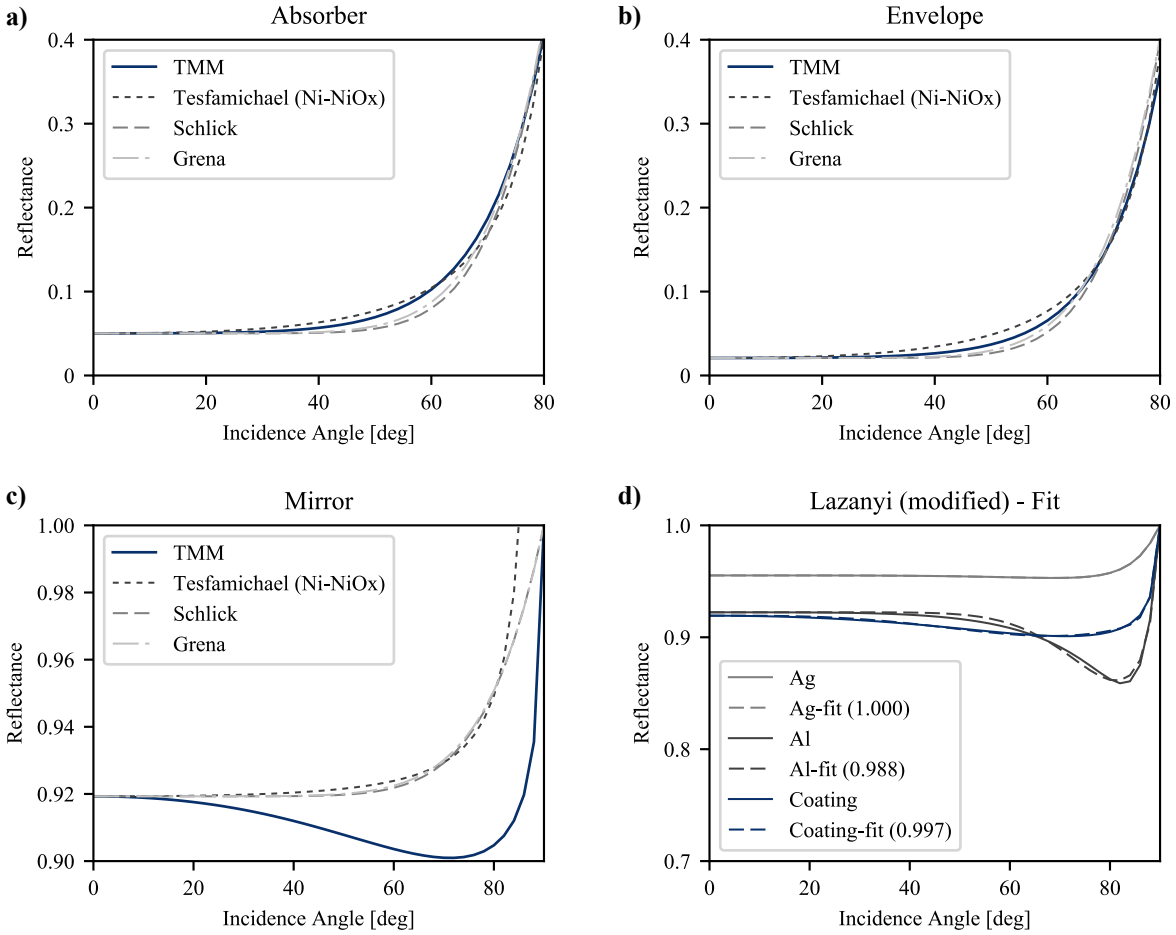

Fig. 4.7 Comparison of different reflectance models (Section 3.2.3) with results from TMM (Section 3.2.2) applied to the thin-film assemblies of Section 4.3. In brackets: coefficient of determination R^2.

Table 4.2 shows a selection of the best 1D reflectance models and their parameters for each respective surface type, as they are discussed in Section 4.5.

Table 4.2 Reflectance model and paramters of each collector component.

Surface Type	Reflectance Model	Parameters
Mirror	Lazányi (modified)	$a = 0.1$
		$b = 1.7$
		$c = 38$
Absorber	Schlick	$R_0 = 0.05$
Glass	Schlick	$R_0 = 0.021$

4.4.3 Comparison of refraction models

Perhaps the main conclusion drawn from the ray-tracing software comparison of Osório et al. [105] was that most differences between simulation results originated from different approaches to model transparent material. This seems plausible, since the overall optical property of such a medium is the result of a coupled effect of reflection, refraction and absorption between and in-between two surfaces (Fig. 4.8). Many different models for refractive material have been implemented in current ray-tracing programs.

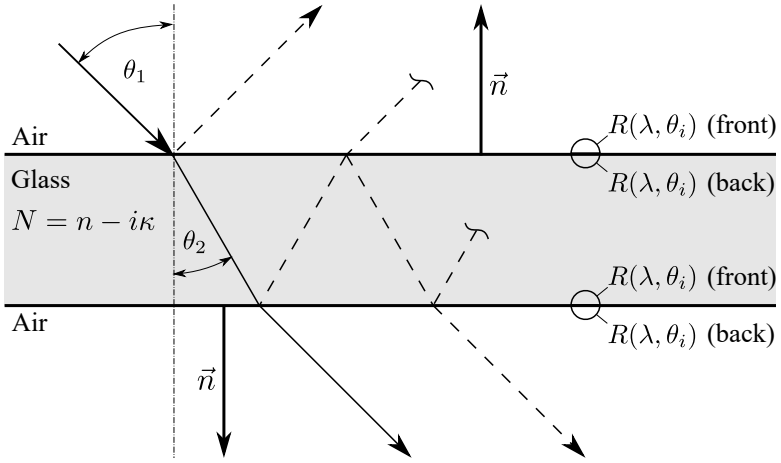

Fig. 4.8 Physical phenomena for refractive material. Multiple reflections between boundaries and absorption in the in-between lead to overall transparency of the medium.

There are two ways to model the reflectance of a transparent sample. Either a single reflectance value is assigned to the surface, then it is valid for both rays that are incident on the front and the back side of the surface, or it is assigned to the front and the back side separately. The latter was implemented in Tonatiuh and RayTrace3D with a back side reflection value of zero. In this case the reflectance defined on the outside of a surface represents the reflectance of the entire volume.

In some cases absorption is calculated considering the overall propagation path through the medium and its complex refractive index κ. In other cases it is permanently included in the surface reflectance value. All programs include the refracted pathway according to Snell's law, but not all programs allow for the consideration of an AR coating (e.g., SPRAY). Since OTSun is flexible when it comes to the parameter input for transparent models, all variations presented in Table 4.3 have been simulated without changing any other parameter from the reference case described in Section 4.3.

While Tonatiuh only accepts constant values, RayTrace3D can import incidence angle dependent reflectance data based on, e.g., experimental results for flat samples. In this study,

the input $R(\theta)$ for the RayTrace3D does not come from experiments, but is the result of a full parameter simulation of a flat glass model of the same thickness as the envelope. The only difference between the RayTrace3D model and the reference case is that the envelope is not flat, but curved. The expected error will be rather small. Results are discussed in the next chapter.

Table 4.3 Overview of different ray-tracing models for transparent media.

Software	Surface				Volume	
	Front	Back	Model	Coating	Real	Imaginary
OTSun	$R(\lambda,\theta)$	like front	TMM	yes	$n(\lambda)$	$\kappa = 0$
No absorption	$R(\lambda,\theta)$	like front	TMM	yes	$n(\lambda)$	$\kappa = 0$
No coating	$R(\lambda,\theta)$	like front	Fresnel	no	$n(\lambda)$	$\kappa(\lambda)$
RayTrace3D	$R(\theta)$	0	File	yes	$n = const$	$\kappa = 0$
Tonatiuh	$R = const.$	$R = 0$	Constant	no	$n = const$	$\kappa = 0$

4.5 Results and discussion

The following results are based on the same sun model (Buie [125]) with a sun cone of 4.65 mrad, a circumsolar ratio of 0.05 and a total count of 10^7 emitted rays. The outcome of the simulations is measured by the optical efficiency of the collector with respect to DNI. Hence, the cosine effect is included in the incidence angle modifier as shown in Eq. (3.1). The reference area A_{ref} is 1440 m^2. It is the cumulative aperture area of the heliostats projected onto the x-y-plane at normal incidence. Furthermore, it is noteworthy that the term "incidence angle" does no longer refer to the angle on a surface, but to the global angle of incidence on the collector aperture.

As described in Section 4.4.1, the first case to be analyzed is the impact of angle- or wavelength-resolved input on the calculated efficiency. Figure 4.9 illustrates the efficiency curves (top) and the respective optical efficiency difference $\Delta\eta = \eta - \eta_{ref}$ (bottom) considering the reference case for simulations of every 5° along the longitudinal or transversal symmetry plane of the collector, respectively (Fig. 4.1).

Figure 4.9 clearly shows that there is a significant difference between considering only constant reflectance and scattering values and an angle-dependent reflectance/scattering curve. The difference in both approaches results in an error of almost 7 % at an incidence angle of 60°. In this case, it should be noted that the relative error $\Delta\eta/\eta_{ref}$ would be constantly

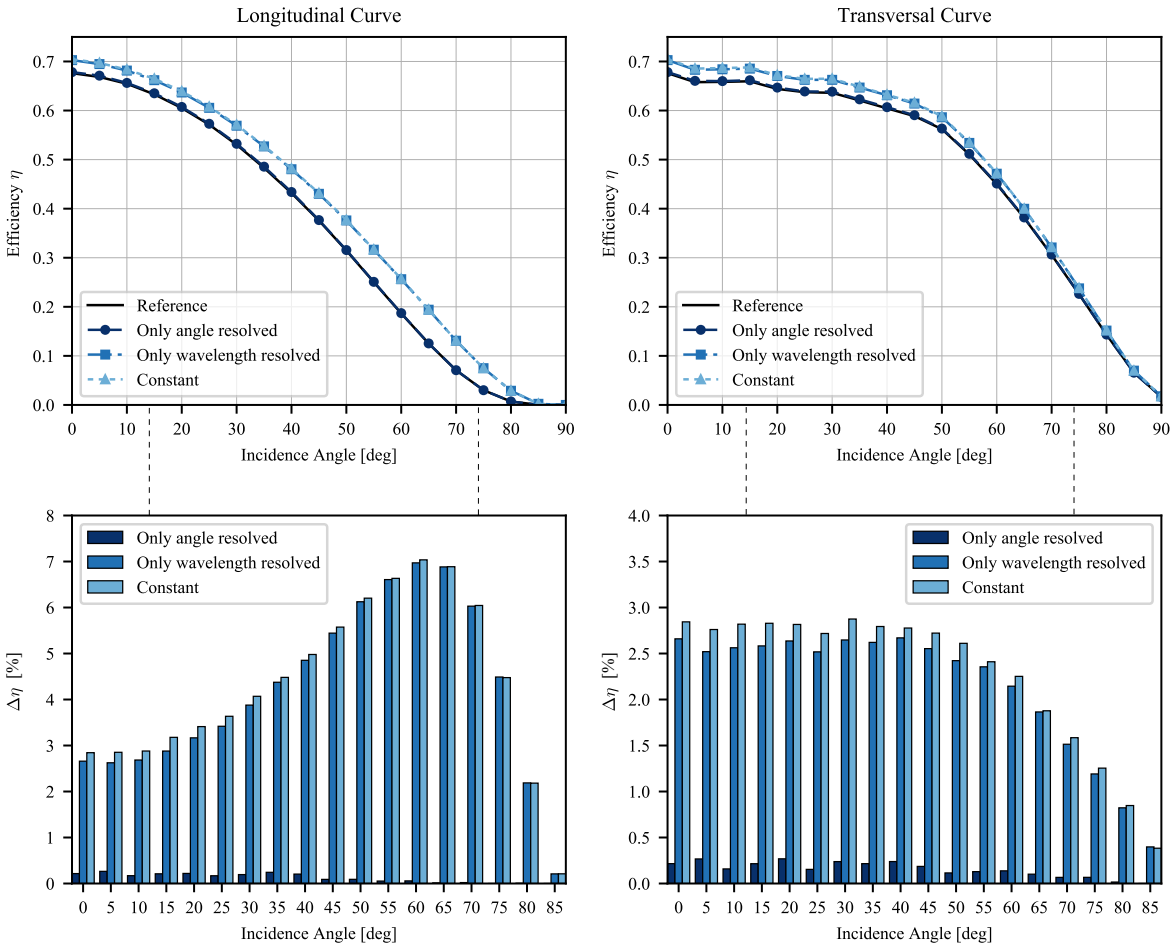

Fig. 4.9 Angle- versus wavelength-resolved input simulations for every 5° along with the longitudinal and transversal collector planes (Fig. 4.1). Top: efficiency curves. Bottom: difference with respect to the reference case.

increasing toward higher incidence angles on a much higher level (+38 % at 60°). Thus, from an energetic perspective, the differences would be even more noticeable in that region.

Figure 4.9 also shows that it is not necessary to conduct a computationally expensive spectral simulation (angle-resolved) for solar thermal applications. The difference in the calculated efficiencies is generally found to be small. It is more significant for lower incidence angles but remains below half a percentage point. This is not surprising because the specular scattering of the mirror reflection is the most influential factor on the wavelength sensitivity of the collector efficiency. Though the scattering measured by Good et al. [76] shows some dependency on the wavelength, with values around 0.5 mrad, it is almost one magnitude smaller than the implemented macroscopic errors (2 mrad to 3 mrad [133, 137]).

In this study, an attempt was made to analyze the effect of the wavelength-dependent specular scattering without obscuring it by the convolution of non-wavelength-dependent macroscopic errors. To do so, simulations of the reference case have been repeated, this time without considering the macro errors and with a variance of specular scattering 5 and 10 times higher than the original value. This parameter range is plausible, since the reference variances provided by Good et al. [76] (0.3 mrad to 0.7 mrad) are significantly smaller than those commonly found in the literature (1.5 mrad to 2.5 mrad), such as in Sutter et al. [80]. The results of this analysis are shown in Fig. 4.10.

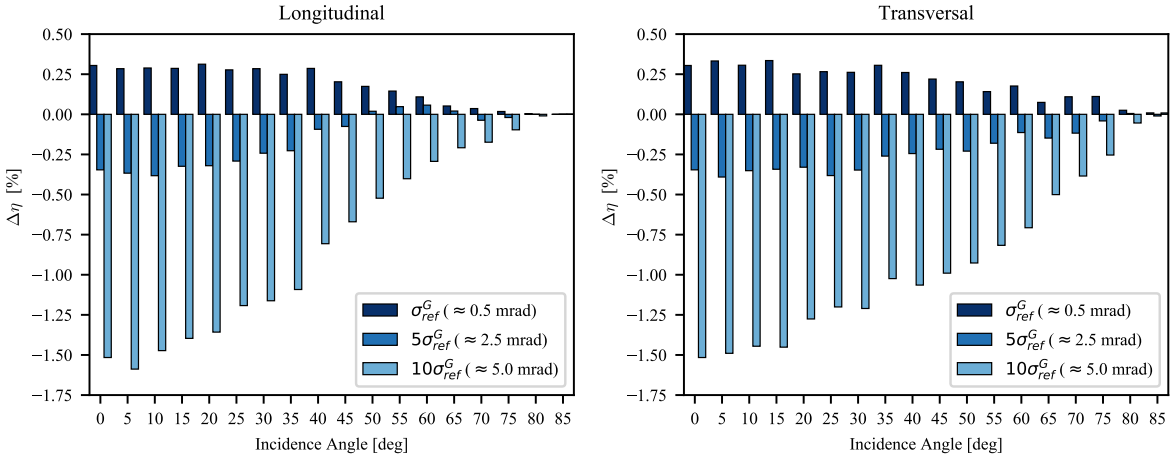

Fig. 4.10 Difference between the calculated efficiency of the full parameter and incidence-angle-resolved simulations for different specular error variances and without considering macro errors.

In this case, the importance of a spectral simulation with larger specular scattering is quite evident. Such a specular ray-tracing feature can make a difference of up to 1.5 % in precision. Although admittedly, a specular scattering of approximately 5 mrad would be rather exceptional for clean solar mirrors, it may be found for accumulated dust [138].

In the end, what matters most is the energy distribution profile on the absorber surface depending on the wavelength. The results shown in Fig. 4.11 are based on the same assumptions as described earlier and assume the highest specular error of $\sigma = 10\sigma_G$. In this case, a remarkable distinction between the intensity profiles of different wavelength intervals on the absorber surface can be noticed. The wavelength intervals were chosen in such a way that they present the same integrated energy share. As clearly shown in Fig. 4.11, the distribution of short wavelengths is more dispersed than that of long wavelengths, and apparently with larger incidence angles in the transversal plane the intensity maximum shifts to the side. This fact might not be too interesting for conventional solar thermal applications, it might however for PVT technologies where the absorber unit is a PV cell.

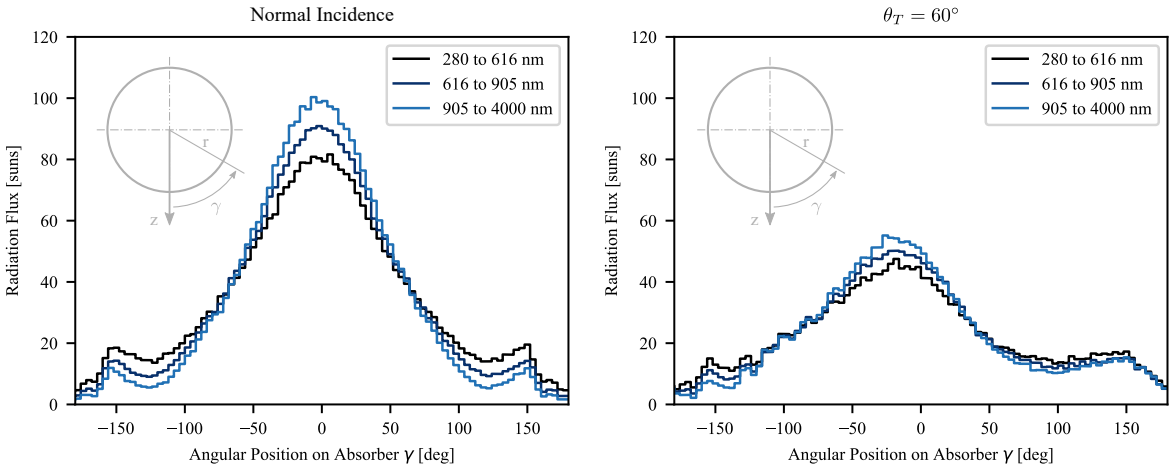

Fig. 4.11 Intensity profile on the absorber surface for simulations with only specular errors of $\sigma = \sigma_G$. The integrated intensity over each wavelength interval is identical.

In order to obtain accurate results from ray-tracing simulations, the previous analysis has shown that the incidence angle dependency of the surface reflectance of the simulated material is an indispensable input. Albeit, these data are not always provided by the manufacturer. In the next step, it has been attempted to recover the incidence angle dependency considering the simple analytical functions discussed in Section 4.4.2. Figure 4.12 illustrates the difference between the calculated collector efficiency for the reference case and simulations based on surface reflectance parameters presented in Table 4.2.

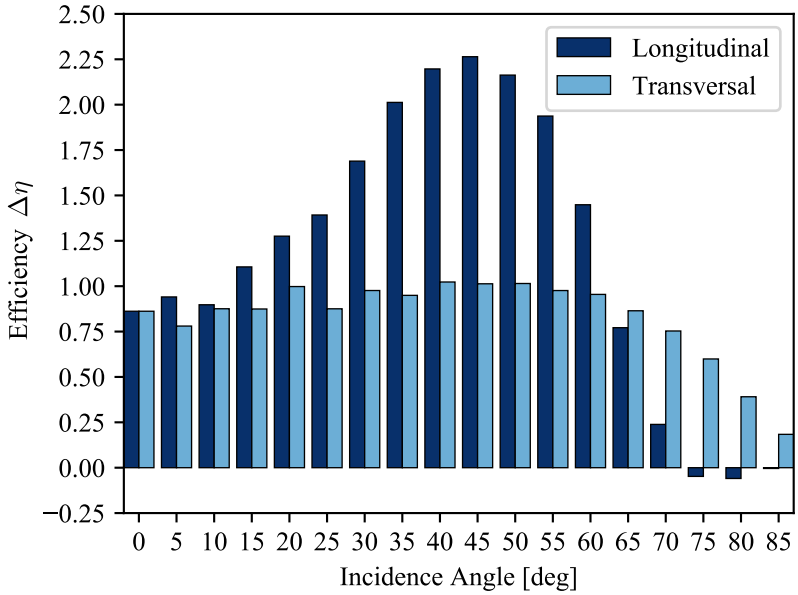

Fig. 4.12 Difference between the calculated efficiency of a full parameter simulation and simulations based on 1D surface reflectance models.

The error is still high with up to 1 % for transversal and approximately 2.25 % for longitudinal simulations, respectively, but it has been reduced by a factor of about 4 as compared to constant simulations from Fig. 4.9. The remaining error is primarily due to inaccuracies of the Schlick model that has been applied to transparent and absorbing materials in Fig. 4.7a and b.

As for the comparison of refractive models, the different definitions from Table 4.3, will be discussed in Fig. 4.13. As expected, neglecting the absorption in the glass does only make a small but notable difference. Higher errors can be observed for the Tonatiuh model or when the AR coating is not taken into account. The first one is comparable to simulations with constant reflectance values and hence shows increasing errors for high angles of incidence. The second one is based on solutions of the Fresnel equations for reflectance values, which do not properly represent the optical characteristics of a thin-film layer. Simulations with the RayTrace3D refractive model show the smallest errors. Basically, these originate from the difference between reflectance of a flat (input) and the actual cylindrical glass sample.

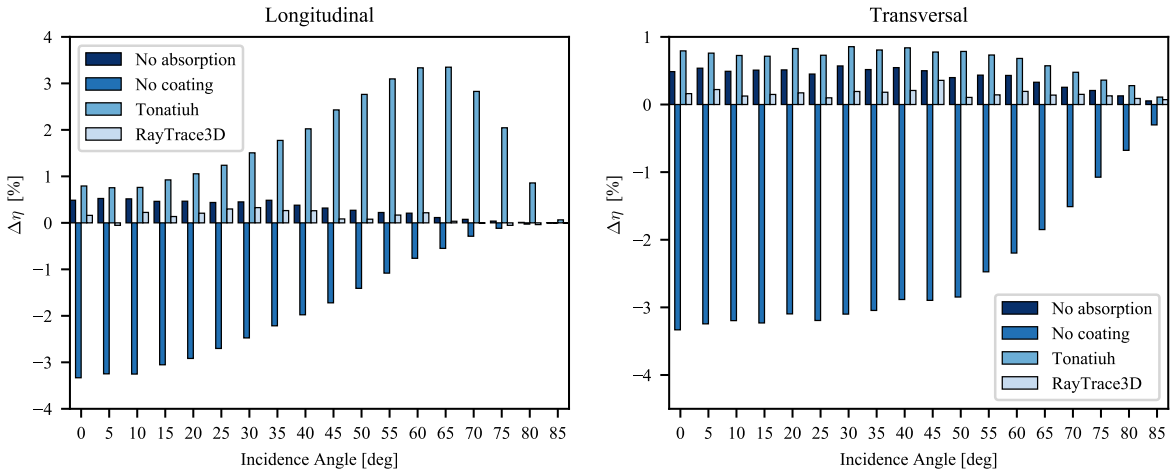

Fig. 4.13 Absolute error between calculated efficiency of a full parameter simulation and a simulations based different refractive models for the envelope according to Table 4.3.

Finally, since the ray-tracing tool possesses the possibility to conduct spectral simulations, both the probability density functions (PDF) of the emitted and the received light spectrum have been compared. The difference of both PDFs is presented in Fig. 4.14. The graph could be interpreted as the solar collector's spectral footprint – the impact on light of different wavelengths that propagates through the domain. It can be observed that the received spectrum is reduced in the very low wavelength region and between 750 and a 1000 nm. This pattern represents the reflectance minimum of the HR-coating of the mirror from Fig. 4.2. Equally, the reduction in the longer wavelengths is caused by the high reflectance of the selective coating of the absorber (Fig. 4.4), but most importantly, the received spectrum is

more pronounced in the high energy UV/VIS region. This is the result of a general optical optimization of all collector components with the purpose to harness solar energy.

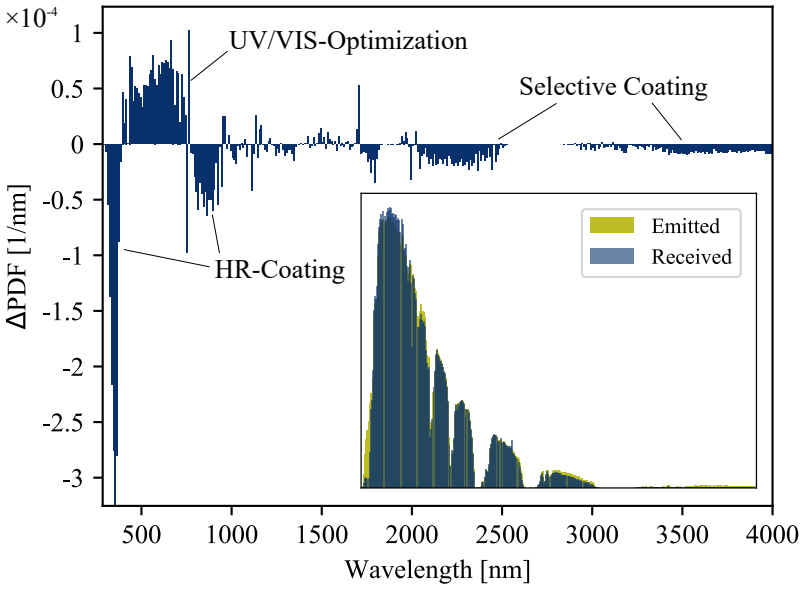

Fig. 4.14 Differences between the probability density functions of the emitted and the received light spectrum.

4.6 Conclusion

Simulations with incidence-angle and wavelength-resolved reflectance and scattering data showed that results based on constant values, as often provided by the manufacturer, are generally found to be inaccurate. In this analysis, it could be demonstrated that the difference can be up to 7 % at an incidence angle of approximately 60° considering a full parameter simulation. On the other hand, it does not seem to be necessary to carry out a complete spectral analysis for solar thermal applications with low optical complexity, unless a collector component shows highly wavelength sensitive behavior. In the presented example, if there is a very strong dependency of the mirror scattering on the wavelength, the error reached the same magnitude as caused by macro errors. Differences of up to 1.5 % could be observed as compared to the more accurate reference case.

On the other hand, even if the difference of the integrated energy values is small, it could be shown that its scattering on the absorber surface depends on the respective wavelength. Therefore, when a wavelength-sensitive absorber is applied, which is the case for PV or PVT collectors, the proper assessment of such intensity profiles could play an important role.

By using simple analytical reflectance models, the difference in the results of simulations with a constant parameter input could be significantly reduced. This work also provided an approach for modeling the reflectance of metallic surfaces by properly using a small set of empirical parameters irrespective of the composition of the mirror.

Chapter 5

Factorization error

5.1 Background

As could be seen in Section 2.1.3, using the original McIntire factorization model of Eq. (2.8) to assess the biaxial IAM-characteristics of solar concentrating collectors with complex geometries is still standard protocol. The factorization model inherently introduces errors by factorizing the underlying non-factorizable physical functions that make the efficiency dependent on the incidence angle. A couple of studies can be found in the literature, which attempt to quantify this error.

Rönnelid et al. analyzed the biaxial model for a CPC [139]. They pointed out that most errors occur in the range of large incidence angles and that using factorized IAM will generally overestimate the annually delivered energy by 4 % to 5 % (referring to a field study in Stockholm, Sweden). Similar conclusions can be found in the case of an LFC. By doing a ray-tracing analysis, Zhu found the maximum error to be 5 % [134]. Mertins, on the other hand, did an experimental study of the annual error in energy gain, referring to the examples Hughade, Egypt (2.4 % error) and Faro, Portugal (3.7 % error) [140]. Horta et al. used an analytical representation of the error by integrating over the entire collector hemisphere, which results in 22.67 % deviation from the ray-tracing results [132]. Bernhard et al. [141] showed that for LFCs, the error can be reduced significantly by replacing the longitudinal angle θ_L with θ_i, the angle between the sun position vector and the transversal plane of the collector (Fig. 5.1). According to Horta et al., using θ_i instead of θ_L results in a hemispherical integration error of 1.65 %, while Mertins stated that annual energy prediction errors can be reduced to less than 0.5 %.

More complex IAM characteristics have been observed for the a fixed mirror CCStaR collector of Pujol and Martínez [101]. In this study, a corrected McIntire model using θ_L was applied to estimate the error between ray-tracing results and the factorization approximation. Pujol and Martínez chose a more statistical approach using the Pearson correlation. A comparison with non-factorized IAM values resulted in an r value of 0.975.

5.2 Objectives

All of the above research was conducted in the framework of individual projects with design and project-specific purposes. So far, no study has been dedicated to compare the effect of simplified IAM models across different technologies. Moreover, each of the mentioned studies chooses a different approach to quantify the factorization error. In this study the error between factorized IAM and ray-tracing IAM will be analyzed for different collector geometries. Results will be presented in Section 5.6 in a more practice-related and intuitive way by calculating the annual error over latitude for the respective site.

Another fact about the IAM that is often overlooked is that there exist different definitions and ways to apply the factorization approach of Eq. (2.8) (Section 5.3). This study will raise awareness of the existence of different models and the lack of consensus on a standardized approach to apply it. By comparing different approaches for different collector geometries, the strengths and weaknesses of each model will be exposed.

5.3 Factorization models and angle conventions

The original approach was proposed by McIntire [49]. He suggested that the optical efficiency for an arbitrary sun position is the product of efficiencies measured at its respective angle projections on the longitudinal and transversal planes of the collector, as seen in Fig. 5.1. The factorization approach proved to be useful in practice, since it reduces the experimental effort by deriving the entire IAM surface $K(\theta_L, \theta_T)$ based on a small number of observations in the collector's symmetry planes.

Mertins [140] first indicated that a factorization in the θ_L-θ_T-angle space showed considerable limitations when applied to a LFC. The main reason for this is that in this case the representation of end-losses is not satisfactory. As a consequence Mertins proposes to conduct the factorization in the θ_i-θ_T-angle space, where θ_i is the angle between the sun vector and the transversal plane of the collector (Fig. 5.1). The main advantage of a

factorization in the θ_i-θ_T-space is that cosine losses would be represented correctly, since

$$\cos\theta = \cos\theta_i \cos\theta_T \tag{5.1}$$

where θ is the incidence angle with respect to the collector normal. Appendix C summarizes a couple of formulas which relate different spaces of angle.

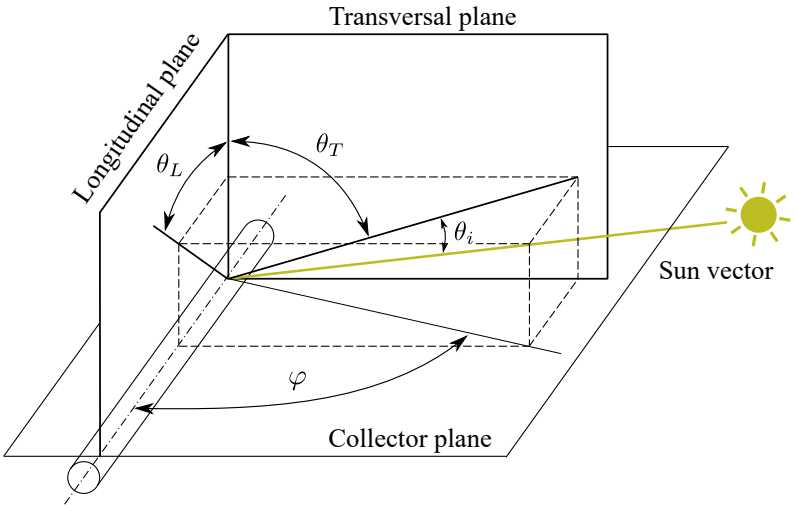

Fig. 5.1 Different angle definitions for biaxial collector geometries.

Apart from different angle spaces it is also important to be aware of the physical effects the IAM factor includes. One effect which should be highlighted in this respect are the cosine losses. Whether or not the IAM factor includes cosine losses depends on the type of irradiance it refers to. While in the low temperature sector, but also in the ISO 9806 standard, the IAM refers to G_{bT} and therefore does not include the cosine factor (e.g., in Horta and Osório [132] or ScenoCalc [93]), in the high temperature sector it refers to DNI and therefore includes the cosine factor (e.g., Morin et al. [142]). Since an accurate definition of the IAM is missing, many other phenomena are often considered separately from the IAM factor, e.g. end-losses [132], shadowing between mirror rows [142], cleaniness [138] etc.

One of the major argument made in this work is that the accuracy of the McIntire approach is a result of both the factorization space and the physical phenomena included in the IAM factor. The scope has been reduced to the cases in Table 5.1.

Table 5.1 Different IAM definitions

Radiation	Angle space	
	(θ_T,θ_L)	(θ_T,θ_i)
G_{bT}	$K(\theta_T,0)K(0,\theta_L)G_{bT}$	$K(\theta_T,0)K(0,\theta_i)G_{bT}$
G_{bn}	$K'(\theta_T,0)K'(0,\theta_L)G_{bn}$	$K'(\theta_T,0)K'(0,\theta_i)G_{bn}$

5.4 Test cases

Simplified versions of four solar collectors have been modeled by a commercial CAD tool, neglecting most of the support structures (Section 5.4.1). A ray-tracing simulation was carried out for each of these geometries using a sophisticated in-house program based on the Monte Carlo method (Section 5.4.2 and 5.4.3). The resulting IAM surfaces were compared with factorized IAMs using the error integration method described in Section 5.5. The resulting error depends on the orientation of the collector. Four collector geometries, illustrated in Fig. 5.2, have been modeled: CPC [143], MaReCo [144], LFC [132], and CCStar [1]. Their designs are based on selected examples from literature. Different location-specific orientations were specified for each collector (see Table 5.2).

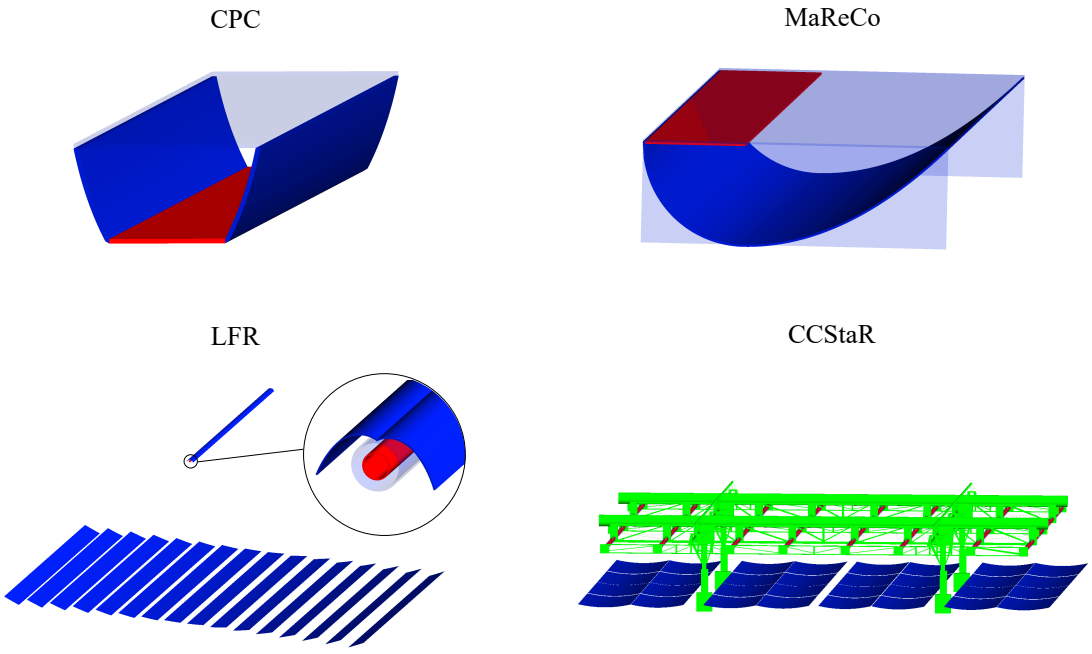

Fig. 5.2 Illustration of the four test cases: CPC, MaReCo, LFC, and CCStaR. Except for the CCStaR geometry, supporting structure is neglected.

5.4.1 Collector geometry and orientation

The CPC collector, first discussed in Helgesson [143], uses a fin absorber, has a truncation factor of 0.4 and an acceptance half angle of 35°. To reduce convection losses, the collector is sealed with a 2 mm-glass cover. The orientation is in east-west (EW) direction and tilt is constantly set to an angle equal to latitude. The collector orientation is based on the rotation coordinate system presented in Fig. 5.3.

MaReCo was included in this study because of its asymmetric design. Its reflector is composed of a circular shaped and parabolic shaped part. The way these two parts are combined defines the inclination of the optical axis. The MaReCo in this study has an optical axis orientation of 90° with respect to de aperture area and its interior is enclosed with a 3 mm-glass plate [144]. The collector orientation is EW and tilt is latitude minus 30°.

LFC consists of a module of 16 mirrors with individual curvature. The receiver has a secondary CPC reflector with an acceptance half angle of 48.39° and a truncated height of 41 mm. The absorber tube is enclosed by a 5 mm-thick solar glass [132]. The collector installation is north-south (NS) and horizontal.

CCStaR was developed at the University of the Balearic Islands. Instead of adjusting the mirrors to the path of the sun, it has a movable receiver, which tracks the focus along a circular trajectory. The collector was originally designed for heat applications, since its static foundation favors rooftop installation. This design is an interesting case for the analysis in this study because its variable geometry leads to complex IAM characteristics that might not be representable by factorization. The reflector consists of eight rows of four mirrors each. The eight receivers have a cylindrical absorber (40 mm in diameter) enclosed by a 1.8 mm-thick glass tube [1]. The collector is orientated in NS direction and tilted to an angle equal to latitude up to a maximum of 30°.

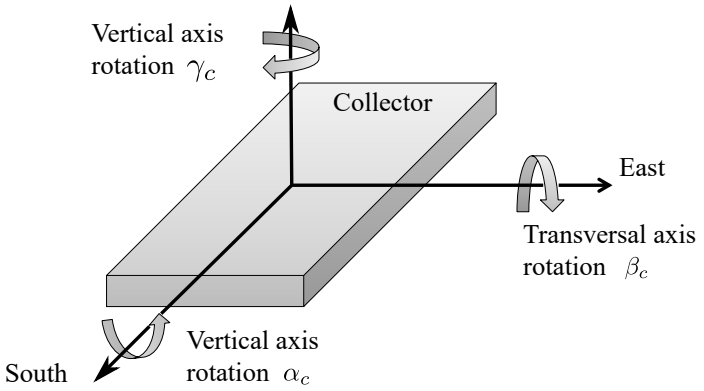

Fig. 5.3 Definition of the collector's rotation coordinate system. Reprinted from Pujol-Nadal et al. [145].

The collector geometries were modeled with a commercial CAD tool VariCAD [146]. The supporting structure, except for the CCStaR geometry, was neglected. Further details about the collector designs are given in Table 5.2.

Table 5.2 Geometrical and operational simulation parameters of each collector, with rotation angles from Fig. 5.3 and latitude ϕ_L.

Collector	A_{ap} $\left[\mathrm{m}^2\right]$	CR $[-]$	l_{focal}/L	Orientation	Tilt
CPC	0.15	1.53	n/a	East-West	$\alpha_c = \phi_L$
MaReCo	4.96	3.45	n/a	East-West	$\alpha_c = \phi_L - 30°$
LFC	138.75	54.57	6.40×10^{-1}	North-South	$\beta_c = 0°$
CCStaR	37.4	5.52	8.10×10^{-2}	North-South	$\beta_c = \begin{cases} \phi_L & \text{if } \phi_L \leq 30° \\ 30° & \text{if } \phi_L > 30° \end{cases}$

5.4.2 Optical specifications

The ray-tracing program that was used for this study incorporates angular dependencies of optical properties, realistic sun models, as well as stochastic photon–material interaction. The program has been validated in Pujol-Nadal [101] and Sallaberry et al. [1]. Most of the optical specifications of each collector were taken from the respective literature (see Section 5.4.1). The optical characteristics of the materials are described by three parameters:

Absorptance: The absorptance of material is given by the absorptance coefficient α. To account for the dependency of α on the angle of incidence, the ray-tracing code incorporates the model of Tesfamichael (Eq. (3.20)), which was derived from experimental results on aluminum oxide [147]. The same coefficients that characterize the specular behavior of aluminum oxide ($b_0 = 0.017$ and $c = 1.8$) were used for the test cases described in the previous section.

Transmittance: To model the transmittance behavior of material such as glass, the ray-tracing software considers Snell's law for refraction (Eq. (3.7)), extinction according to Beer–Lambert (Eq. (3.32)), and the electromagnetic Fresnel equations (Eqs. (3.2) and (3.3)). The material is completely defined when specifying the refraction index n of air and the material as well as the extinction coefficient κ of the material.

Reflectance: Reflectance of the material is defined by the reflectance coefficient R and the specular scattering σ. σ represents the variance of a Gaussian distribution that models scattering due to both microscopic errors (e.g., surface roughness, specular effects) and

macroscopic errors (e.g., slope deviations, tracking errors). A summary of all the optical parameters specified in the ray-tracing model for each collector is given in Table 5.3.

Table 5.3 Optical simulation parameters of each collector.

Collector	Absorptance	Transmittance		Reflectance	
	α [−]	κ [mm^{-1}]	n [−]	R [−]	σ [mrad]
CPC	0.950	7.125×10^{-3}	1.52	0.8	7.0
MaReCo	0.955	1.71×10^{-2}	1.52	0.95	4.0
LFC	0.955	7.125×10^{-3}	1.52	0.93	4.0
CCStaR	0.950	4.0×10^{-3}	1.52	0.85	7.0

5.4.3 Numerical specifications

The ray-tracing software is based on different stochastic models. The origin of each ray is defined by a randomly initialized "seed" according to the Monte Carlo method. The sun is modeled using the Buie equations considering a circumsolar ratio of 0.05 and a sun angle of 4.65 mrad [125].

The optimal ray density for each collector was determined by a sensitivity analysis for a specific set of critical incidence angles. The selected number of rays was assumed to be sufficiently high when no more significant differences could be notices for the efficiency values at critical angles of incidence θ ($\Delta\eta(\theta) \leq 1.0 \cdot 10^{-3}$). The ray density for each specific case is strongly related to the complexity of the geometry. Table 5.4 gives an overview of the different numbers of rays used for the simulation. The ray density chosen for the CPC collector is exceptionally high to guarantee accuracy around the problematic region of incidence angles near the acceptance angle. The CPC geometry is not highly complex and the computation time is therefore short.

5.5 Error definition

Different methods have been chosen to interpret the error that factorization introduces into energy gain predictions. These can be categorized as the energetic and non-energetic approaches. The non-energetic approach only considers the IAM surface obtained by factorization and ray-tracing results. Various methods can be found which compare both IAM surfaces. Zhu considered only the maximum error [134]. Horta et al. estimated an average

Table 5.4 Numerical parameters of each collector.

Collector	Rays $[-]$	Density $\left[\mathrm{m}^{-2}\right]$
CPC	5.0×10^5	3.26×10^6
MaReCo	1.0×10^5	3.02×10^4
LFC	3.0×10^5	2.16×10^3
CCStaR	1.0×10^6	2.67×10^4

error by integrating over the entire surface, each increment weighted by the cosine of the incidence angle [132]. Pujol et al. analyze relation between the composed IAM surface and the numerical result by applying a Pearson correlation test, which gives a rather statistical notion of the error [129]. These methods are general and provide a parameter that could be assigned to every collector specifically. Nevertheless, under certain circumstances, these interpretations can be less meaningful. So is the overall error also influenced by incidence angles which never appear for a real collector installation during the annual course of the sun [148]. For example, for a horizontal LFC installation, the factorization errors made for incidence close to normal are irrelevant if the collector is located in areas of high latitudes. In addition, in practical implementation, the non-energetic error estimation does not account for the different intensities of solar radiation, which puts more weight for certain incidence angles. As an example, Fig. 5.4 shows the accumulated and normalized annual radiation profiles on the collector hemisphere at latitudes 0°, 30°, and 60°. When the collector tilt is equal to the latitude, the radiation band is located around the collector normal with a cut off edge near the horizon.

In the energetic approach, the collector efficiency equation is taken as a basis. Instead of real IAM values, it represents the error in predicting the annual energy yield when factorization is applied. Rönnelid et al. validated the numerically integrated energy gain based on factorization with experimental results of a CPC installation in Stockholm (Sweden) [139], whereas Mertins validated his results with measurements of a LFC in Hurgada (Egypt) and Faro (Portugal) [140].

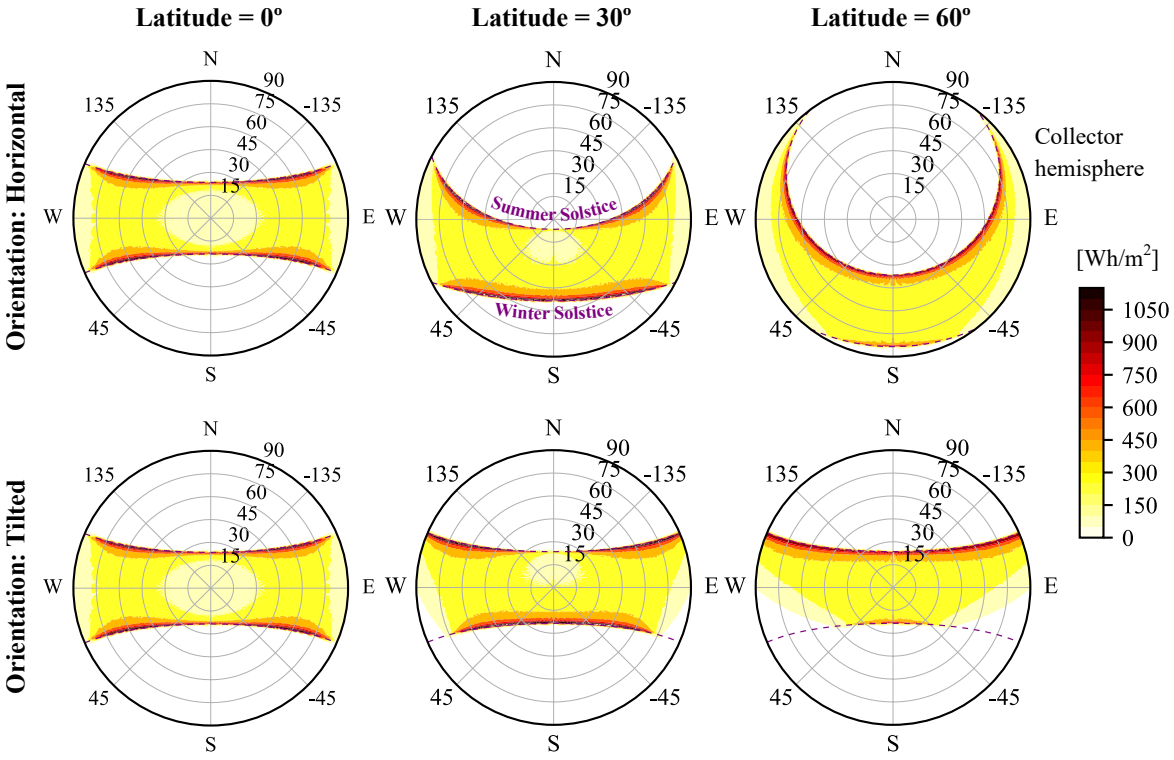

Fig. 5.4 Annual irradiance distribution over the collector hemisphere according to the clear-sky model of Meinel and Mainel (Eq. (5.10)). Distributions are shown for different latitudes and collector orientations.

While this semi-experimental approach yields reliable results for application-specific installations, it lacks generality as it might not be applicable to other sites or collector technologies. For achieving a more site-specific result, yet adequately general interpretation of errors, another purely numerical approach is suggested in this study. It can be seen as a trade-off between the two previously described methods. This method is partly based on the collector efficiency equation. Thermal effects such as heat losses or thermal capacity are not taken into consideration. The annual energy yield of each collector is then calculated for both the composed IAM surface and the ray-tracing results depending on the latitude at which the collector is located (Eqs. (5.2) and (5.3)).

$$q_{RT} = F'\eta_0 K'(\theta_T, \theta_L) G_{bn} \tag{5.2}$$

and

$$q_{fac} = F'\eta_0 K'(\theta_T, 0) K'(0, \theta_L) G_{bn} \tag{5.3}$$

Here, only direct beam is considered and the energy gain by diffuse radiation is neglected. The relative error is defined as the difference between factorization and ray-tracing, as follows:

$$\varepsilon_a(\phi) = \frac{q_{fac} - q_{RT}}{q_{RT}} \tag{5.4}$$

From Eq. (5.2) and (5.3) follows the definition of collector specific and latitude ϕ_L dependent annual error:

$$\varepsilon_a(\phi) = \frac{\sum_{year} K'(\theta_T, 0) K'(0, \theta_L) \cdot G_{bn}(\theta) \cdot \Delta t}{\sum_{year} K'(\theta) \cdot G_{bn}(\theta) \cdot \Delta t} - 1 \tag{5.5}$$

According to the IAM definitions listed in Table 5.1, four different definitions can be applied to Eq. (5.5) depending on the space of angle and the type of radiation that is considered: (θ_T, θ_L)-space and radiation on tilted surface G_bT:

$$\varepsilon_a(\phi) = \frac{\sum_{year} \frac{\cos(\theta(t))}{\cos(\theta_T(t))\cos(\theta_L(t))} K'(\theta_T(t), 0) K'(0, \theta_L(t)) \cdot G_{bn}(\theta(t)) \cdot \Delta t}{\sum_{year} K'(\theta(t)) \cdot G_{bn}(\theta(t)) \cdot \Delta t} - 1 \tag{5.6}$$

(θ_T, θ_L)-space and direct normal irradiance G_{bn}:

$$\varepsilon_a(\phi) = \frac{\sum_{year} K'(\theta_T(t), 0) K'(0, \theta_L(t)) \cdot G_{bn}(\theta(t)) \cdot \Delta t}{\sum_{year} K'(\theta(t)) \cdot G_{bn}(\theta(t)) \cdot \Delta t} - 1 \tag{5.7}$$

(θ_T, θ_i)-space and radiation on tilted surface G_bT:

$$\varepsilon_a(\phi) = \frac{\sum_{year} \frac{\cos(\theta(t))}{\cos(\theta_T(t))\cos(\theta_i(t))} K'(\theta_T(t),0)K'(0,\theta_i(t)) \cdot G_{bn}(\theta(t)) \cdot \Delta t}{\sum_{year} K'(\theta(t)) \cdot G_{bn}(\theta(t)) \cdot \Delta t} - 1 \tag{5.8}$$

(θ_T, θ_i)-space and direct normal irradiance G_{bn}:

$$\varepsilon_a(\phi) = \frac{\sum_{year} K'(\theta_T(t),0)K'(0,\theta_i(t)) \cdot G_{bn}(\theta(t)) \cdot \Delta t}{\sum_{year} K'(\theta(t)) \cdot G_{bn}(\theta(t)) \cdot \Delta t} - 1 \tag{5.9}$$

However, from Eq. (5.1) follows that when θ_i is used referring to the *IAM* to G_{bT} or G_{bn} makes mathematically no difference. Consequently, Eqs. (5.8) and (5.9) are mathematically the same and only three different error definitions remain. They are discussed in Section 5.6.

Essentially, Eqs (5.6) to (5.9) can be interpreted as an irradiance/energy-weighted factorization error. This requires reasonable assumptions about the annual path of the sun as well as the location specific hemispherical distribution of irradiation. The model to calculate the position of the sun was taken from Duffie and Beckman [38], while the radiation intensity is based on Eq. (5.10) from Meinel and Mainel [149]. The latter is a simplified model that only relies on geometric parameters and does not need any measurable atmospheric parameters.

$$G_{bn} = E_0 \cdot 0.7^{AM^{0.678}} \tag{5.10}$$

with the extraterrestrial radiation I_0,

$$E_0 = 1367.7 \cdot \left(1 + 0.033 \cdot \cos\left(\frac{2\pi}{365} d_y\right)\right) \tag{5.11}$$

and the representation for the air mass (AM) coefficient as given by Karsten and Young [150]

$$AM = \frac{1}{cos(\theta_S) + 0.50572 \cdot (96.07995 - \theta_S)^{-1.6354}} \tag{5.12}$$

5.6 Results

The annual error integration discussed in Section 5.5 was applied to all of the four test cases described in Section 5.4. Both IAM and DNI depend on the sun position vector. The instant DNI value is based on Eq. (5.10), while the IAM values are obtained by interpolation of the ray-tracing surface. Figure 5.5 shows exemplary results of IAM value interpolation for the LFC case described in Section 5.4, which was installed at latitude 60°. In Fig. 5.5 (left)

the annual set of sun position vectors, with a time step of 1 h and mapped onto θ_T-θ_L-space, is illustrated. In the same figure, a typical path of the sun for the day 160 of the year, near the summer solstice (21th of June, day 172), is also shown. Starting from the sun position tuples of Fig. 5.5 (left), the annual IAM values can be interpolated from the ray-tracing or factorization surface (Fig. 5.5 (right). The same figure also depicts the expected direct solar irradiation based on Eq. (5.10).

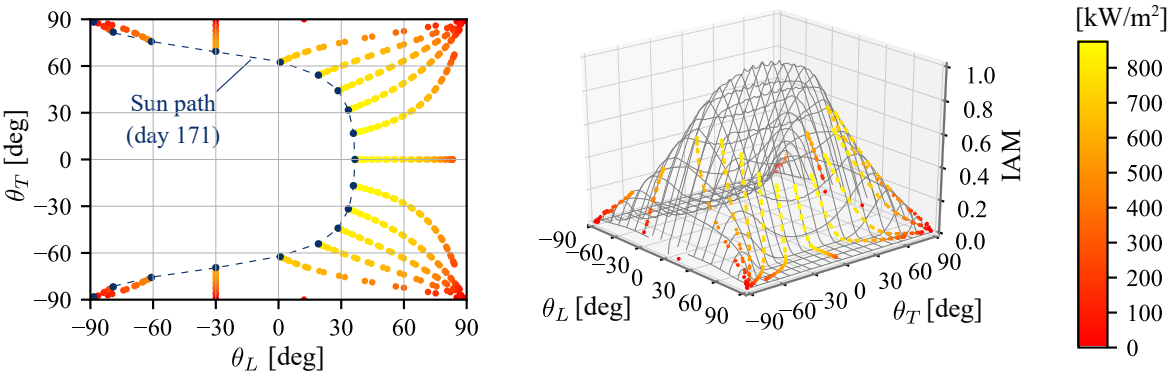

Fig. 5.5 Annual IAM value interpolation for the ray-tracing results of the LFC in Fig. 5.2 installed at latitude 60°.

The integration time step was selected as 1 min for Eqs. (5.6) to (5.8) as described below. With these settings the computation time for each case extended to a few minutes using a 2.2 GHz i7 quad core processor. Fig 5.6 shows the total annual energy gain as a function of latitude Φ_L based on the ray-tracing simulations and the clear sky radiation model of Eq. (5.10).

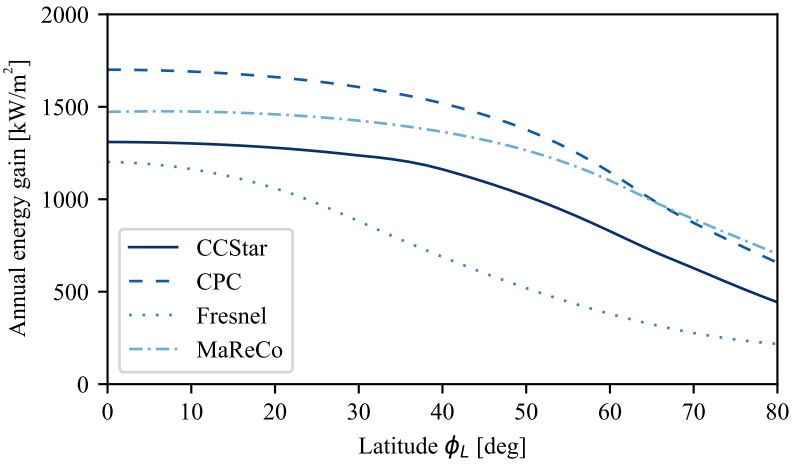

Fig. 5.6 Integrated annual energy gain of each test case based on ray-tracing simulations and the ideal clear sky radiation model in Eq. (5.10).

Figure 5.7a shows the relative annual error ε_a of the three relevant models from Section 5.5 for the EW CPC installation as given in Table 5.2. In this case, small errors ($< 2\,\%$) are generated independently of the IAM model for all the latitude locations. The curves show a fairly constant trend. The reason for this is the operational mode of the CPC collector. Since the collector is always tilted to an elevation angle equal to latitude, the error integration is more or less restricted to the same area on the IAM surface (close to normal, Fig. 5.4). Except for G_{bT} on θ_T-θ_L-domain, a tendency of slightly but constant overestimate can be observed. It should be noted that in case of G_{bT}, cosine losses are accounted for separately, while for DNI the cosine effect is included in the IAM factors, and therefore, in a certain way, accounted for twice (first in the observation on the transversal plane and then in the observation on the longitudinal plane). This leads to an underestimation of the actual IAM value. In the case considered herein, the traditionally applied factorization approach in the θ_L-θ_L-space yields the best results.

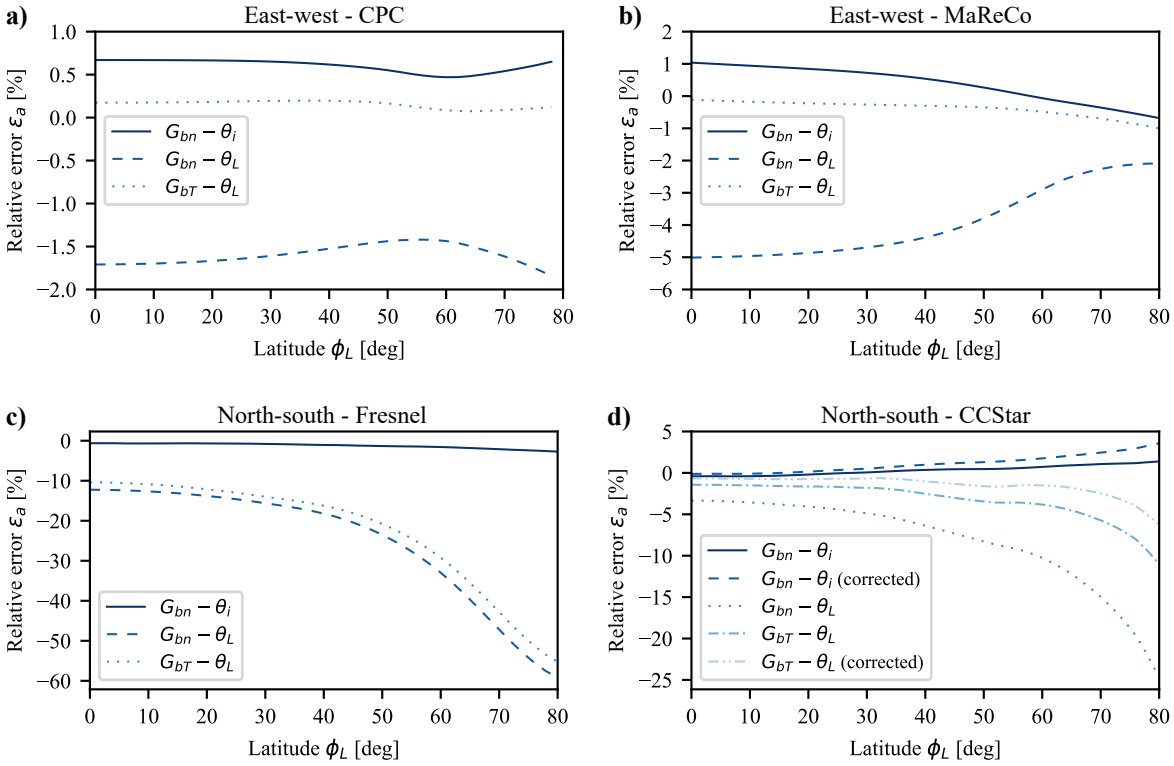

Fig. 5.7 Results of annual error integration based on Eqs. (5.6) to (5.9) for different test cases from Section 5.4.

The results for the MaReCo collector are depicted in Fig. 5.7b). Due to its design, the collector's efficiency is moderately affected by end-losses. This can be seen in the constant underestimate of both the θ_L definitions. The underestimate is multiple times larger if referred to DNI instead of G_{bT}, because the cosine effects are not adequately represented by

factorization. Both θ_i definitions and the traditional G_{bT}-θ_L model represent most accurate approximations.

The error integration for LFC was done with NS orientation, which is common for most plant installations. The results are shown in Fig. 5.7c. While factorization in θ_T-θ_i-space causes the smallest errors ($< 3\,\%$), it becomes clear that factorization in the θ_T-θ_L-space approximates the real values poorly. Starting from a very strong underestimate of 10 % at latitude 0°, the negative error further increases at higher latitudes. As discussed in Section 5.3, it is mainly based on a misinterpretation of end-losses in the θ_T-θ_L-space, as the magnitude of end-losses does not correlate with the angle θ_L. Figure 5.8 illustrates the asymmetry of the IAM surface in θ_T-θ_L-space, which cannot possibly be represented by factorization. In theory, θ_T-θ_L-curves should approximate θ_i, as the ratio of focal length l_{foc} to aperture length L approaches zero. This has also been observed by Horta and Osório [132]. Since the example mentioned herein has a fairly high ratio (very short collector), the end-loss effect is comparatively stronger.

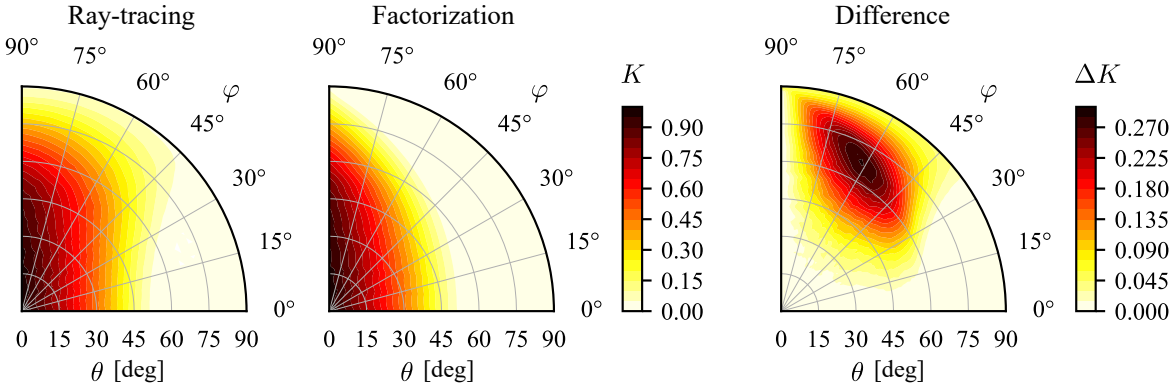

Fig. 5.8 Error of factorization in θ_T-θ_L-space in the case of the LFC in Fig. 5.2. Large errors are caused for oblique angles due to a poor representation of end losses.

The CCStaR as a line-focusing system yields results similar to the LFC (Fig. 5.7d). Large errors can be observed for θ_T-θ_L-factorization due to end-loss misinterpretation. The CCStaR example with a much lower l_{foc}/L-ratio also shows less, but still significant, underestimate (up to $-25\,\%$; LFC: $-60\,\%$). One design specific aspect of the CCStaR, when it comes to end-loss estimation, is that l_{foc}/L-ratio is not constant. CCStaR shows a strong geometry-changing behavior (it is part of variable geometry collectors). It tracks the focal point by moving the absorber tube along a circle trajectory around the reflector. Consequently, the end-losses cannot be expressed as a function of θ_L or θ_i alone. Pujol-Nadal et al. suggested a correction factor by which the composed IAM surface should be multiplied in order to compensate for these asymmetries [100, 129]. Based on geometric assumptions, it was

shown that such a correction factor for the θ_T-θ_L-factorization would be:

$$f(\theta_T, \theta_L) = \frac{L - [R + R\cos(2\theta_T)]\tan(\theta_L)}{L - 2R\tan(\theta_L)} \tag{5.13}$$

in case of factorization in θ_T-θ_i-domain a modified form of this correction factor is necessary:

$$f(\theta_T, \theta_i) = \frac{L - R\sqrt{\sin^2(2\theta_T) + [\cos^2(2\theta_T) + 1]^2}}{L - 2R\tan(\theta_i)} \tag{5.14}$$

Thus, the corrected composed IAM surface is:

$$K(\theta_T, \theta_{L/i}) = K(\theta_T, 0) \cdot K(0, \theta_{L/i}) \cdot f(\theta_T, \theta_{L/i}) \tag{5.15}$$

Both θ_L and θ_i corrections were applied (Fig. 5.7d). Although from a physical perspective, it would be more appropriate to consider the correction factor, the non-corrected version shows more accurate results for θ_i-θ_T model, probably because it accidentally balances out the otherwise overestimate of optical effects. For the G_{bT}-θ_L model, however, the correction leads to significant improvements.

Referring factorization to θ_i has the advantage of representing the end-losses and cosine losses more accurately - the two major effects for IAM reduction. The results of all four test-cases for (θ_T,θ_i)-factorization were compared with each other to see how other effects (optical parameters, supporting elements, design specific effects) respond under different circumstances (Fig. 5.9). Two possible patterns can be derived:

First: LFC is the only collector whose error curve is constantly negative (continuously decreasing with higher latitudes). Apparently the approximation is not able to cope with other phenomena with favorable effects on the collector's efficiency. Such effects can be caused by blocking or shading for example.

Second: CCStaR collector shows a notable tendency of increasing error with higher latitudes. The reason for this is most likely that factorization does not adequately display the diminishing effect of supporting elements on real IAM.

Finally, the influence of aperture length L on the factorization error in the θ_T-θ_L-domain for LFC has been discussed. As mentioned earlier, the main cause of deviation between factorization and ray-tracing results is the missing correlation between the angle θ_L and end-losses in case of line focusing systems. With a decreasing ratio of focal length l_{focal} to collector aperture length L, end-losses become less significant and hence the factorization error should be less significant as well. This can clearly be seen in Fig. 5.10, which shows

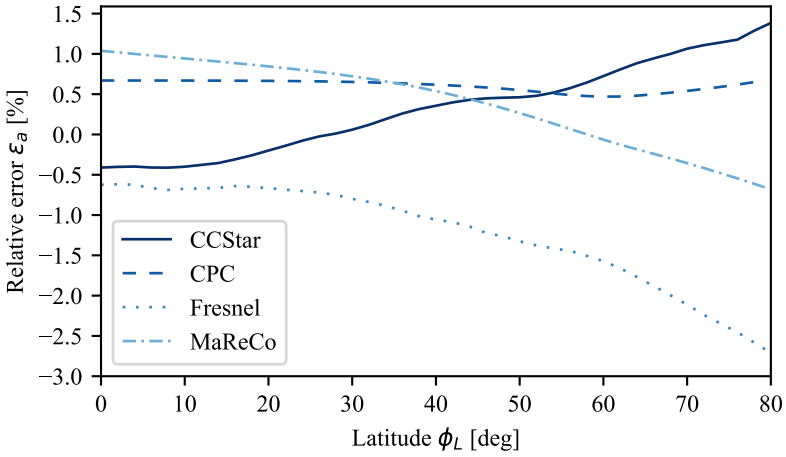

Fig. 5.9 Comparison of annual error integration over latitude for factorization in θ_T-θ_i-space.

integrated θ_T-θ_L-factorization errors for the LFC collector of Section 5.4 with different lengths. At this point, the absolute of the error is accumulated. The original length is 12 m. With increasing aperture length L and decreasing ratio l_{foc}/L the factorization error decreases. However, in no case it reaches the result of the factorization in the θ_T-θ_i-space.

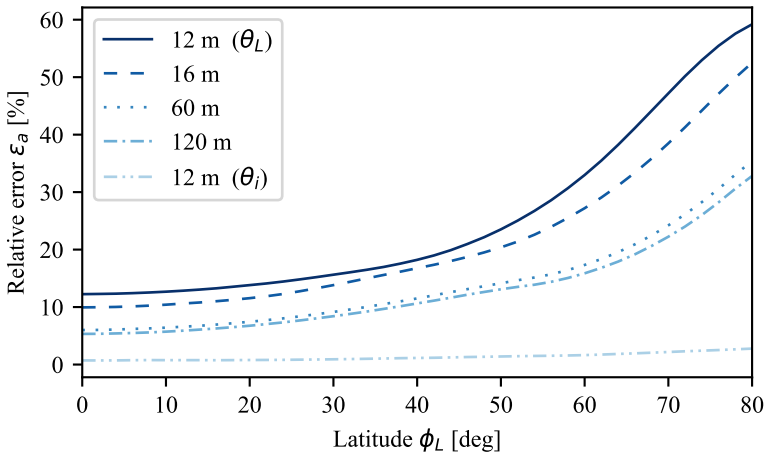

Fig. 5.10 Influence of the aperture length on the θ_T-θ_L-factorization error (horizontal, NS LFC installation). Compared to constantly low θ_T-θ_i-factorization error.

Even though most of the figures imply very small errors, results should be treated with care when estimating the actual impact on annual energy prediction. The presented approach was chosen to compare different IAM definitions with each other, but it is not a tool to assess the economical or technical feasibility of a collector. Although, the integration is based on the collector efficiency equation, it does not include operational parameters such as process temperature, diffuse radiation, wind correction or heat capacity. Rönnelid et al. [139], while analyzing the impact of factorization on the overall energy gain experimentally, detected a

4 % to 5 % overestimate for CPC with 45° tilt at latitude 59 % (Stockholm). This difference of 4 % to 5 % in energy gain corresponds to less than 0.2 % relative error of the described method.

5.7 Conclusion

The accuracy of the McIntire factorization approximation was compared as it was applied to different domains (θ_T-θ_L vs θ_T-θ_i) and referring to different irradiances (DNI vs. G_{bT}). The scope of the study extended to four different solar collector designs: CPC, MaReCo, LFC and CCStaR. By defining the error as the difference between DNI-weighted annual integration of ray-tracing and factorized IAM surfaces at different latitudes, a magnitude of error related to energy output has been provided without the loss of generality associated with site specific evaluations.

Factorization in θ_T-θ_i space yielded accurate results in all of the cases, including static collectors. It was only slightly outperformed by the traditional θ_L-approach in case of a CPC and MaReCo. The difference was, however, rather marginal. When it comes to experimental assessment, the θ_i-model seems to provide a good tradeoff between effort and accuracy. By definition, it accounts for cosine losses and end-losses, which are the two major effects responsible for the decrease of the IAM factor at large incidence angles. Apart from that, using θ_i would solve the debate about whether to refer the IAM to direct or tilted beam, as it makes mathematically no difference. Conclusively, in θ_L- and θ_i-models, the latter represents the best alternative in the cases analyzed. The θ_i-model seems to be the better choice for line focusing systems in general, since it doesn't have any additional disadvantages or drawbacks over the conventional model.

The European (EN 12975-2), the American (ASHAE) as well as the International (ISO 9806:2013) testing standards dictate factorization in the θ_T-θ_L domain. This factorization model produces poor approximations for some concentrating collectors such as the LFC. For this reason, it is already common practice that manufacturers and users of LFC use a factorization in the θ_T-θ_i domain. It has been shown that this factorization not only produces better results for both the LFC and the FMSC, but it produces at least comparable results for the other test cases as well. Therefore it appears to be the more general alternative. Factorization in (θ_i-θ_T)-space inherently accounts for two effects: Cosine effect:

$$\cos\theta = \cos\theta_i \cos\theta_t \tag{5.16}$$

End losses:

$$\Delta l = f(\theta_i) \tag{5.17}$$

There will never be a factorization approach that could perfectly describe the real IAM surface. Factorization inherently introduces an error, as the underlying physical mechanisms cannot be mapped on a bi-angular domain.

Chapter 6

Impact of thermal losses on the factorization error

6.1 Background

It has been shown in Section 5.1 that many studies were conducted with the purpose of quantifying the error between the IAM surface based on simulations and the one based on factorization. In all of these studies, the thermal part of the energy equation was neglected. Since a poorly approximated IAM value affects only the optical term of the energy equation (Eq. (2.1)), it might seem reasonable to neglect thermal effects such as the process temperature. However, in view of an annual energy balance, increasing heat losses due to elevated process temperatures can influence the significance of the errors made on the energy gain side. No previous study could be found on this topic. Considering the constantly increasing demand of industrial solar thermal applications, the influence of the process temperature on the factorization approach is a fact worth analyzing.

6.2 Mathematical model

If the influence of diffuse irradiation, thermal capacity, and wind is not taken into account, the QDT equation is reduced to its simplified form of Eq. (6.1). This equation can be regarded as composed of two separate parts: the optical part $\dot{q}^{opt}$ and the thermal part $\dot{q}^{th}$, where $\dot{q}^{th}$ is

the only temperature dependent term.

$$\dot{q} = \underbrace{\eta_{0,b} \cdot K_b'(\theta) \cdot G_{bn}}_{\dot{q}^{opt}} - \underbrace{\left(c_1 \cdot \Delta\vartheta + c_2 \cdot \Delta\vartheta^2\right)}_{\dot{q}^{th}} \tag{6.1}$$

where G_{bn} is the direct normal irradiance, $\Delta\vartheta$ is the difference between ambient temperature and mean temperature of the heat transfer fluid $\vartheta_m - \vartheta_a$.

When it comes to annual energy integration of Eq. (6.1), the IAM $K_b'(\theta)$ plays an important role, as it reflects the collector response to different sun angles. This behavior can be fairly complex and is best illustrated with a surface of IAM values over all possible angle pairs that define the position of the sun. The most popular spaces are those spanned by the projected angles (θ_L, θ_T) or (θ_i, θ_T) respectively, as discussed in the previous chapter; Fig. 5.1 shows the angle definitions. In this study, the IAM surface was obtained numerically. A simulation was conducted for each of the four collector geometries that are presented in Section 6.3. The simulation has been run for all possible (θ_i, θ_T) tuples with an increment of 5° by using once more the in-house ray-tracing program OTSun. In order to estimate the error of the factorization approach, two IAM surfaces were compared:

- Factorized surface (FAC): This is based on the ray-tracing results obtained by varying only one of the two angles (either $(0, \theta_T)$ or $(\theta_i, 0)$). All other angles are defined as the product of the corresponding transversal and longitudinal IAM values, according to Eq. (2.8).
- Ray-tracing surface (RT): This is completely based on the results obtained by ray-tracing for every point on the collector hemisphere. Ray-tracing results are assumed to be close to the real optical behavior of the collector and are therefore used as a reference for error.

Fig. 6.1 shows the factorized and the ray-tracing IAM surfaces in the case of a LFC of Section 6.3 as well as the difference between both surfaces in the (θ_i, θ_T)-space.

The factorization error can be defined as the ratio of the annual difference between ray-tracing and factorization results considering the collected ray-tracing energy as a reference. The definition of the factorization error is given as follows:

$$\varepsilon(\Delta\vartheta) = \frac{\int^{year}(\dot{q}_{RT} - \dot{q}_{FAC})dt}{\int^{year}\dot{q}_{RT}dt} = \frac{\int^{year}(\dot{q}_{FAC}^{opt} - \dot{q}_{RT}^{opt})dt}{\int^{year}(\dot{q}_{RT}^{opt} - \dot{q}_{RT}^{th}(\Delta\vartheta))dt} \tag{6.2}$$

Note that only the denominator in Eq. (6.2) is temperature dependent; consequently, a higher error ratio can be expected with higher temperatures.

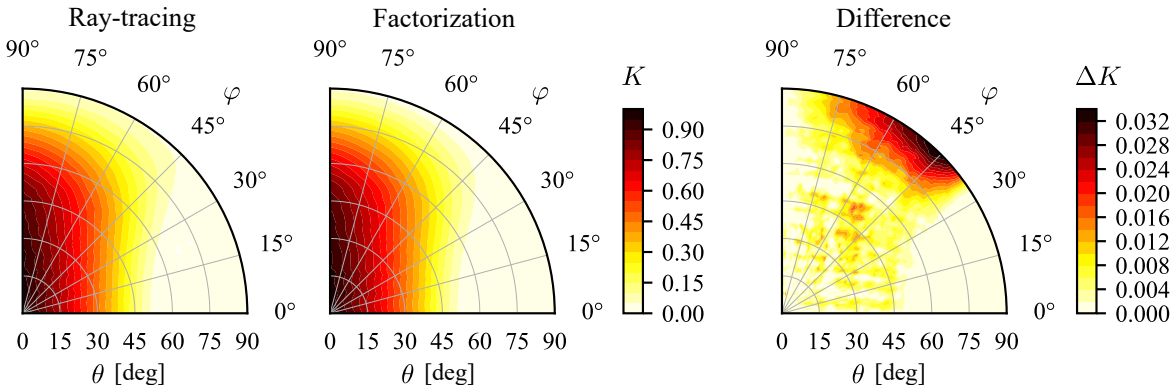

Fig. 6.1 Error of factorization in the θ_T-θ_i-space in the case of the LFC illustrated in Fig. 5.2.

6.2.1 Ideal error development

The factorization error according to Eq. (6.2) was analyzed in the previous chapter neglecting all thermal effects ($\varepsilon(0)$). The θ_T-θ_i factorization, in most cases, yields the most reliable results. Nevertheless this error $\varepsilon(0)$ ranges from 0.47 % to 0.67 % for a CPC collector, -0.68 % to 1.04 % for a MaReCo collector, -2.71 % to -0.61 % for a Fresnel collector, and -0.41 % to 1.38 % for a CCStaR collector depending on the orientation and latitude at which the collector is installed.

Now, Eq. (6.3) shows the trend of $\varepsilon(\Delta\vartheta)$ with regard to the reference value $\varepsilon(0)$, which is the factorization error at ambient conditions without thermal losses $\Delta\vartheta = 0$.

$$\frac{\varepsilon(\Delta\vartheta)}{\varepsilon(0)} = \frac{1}{1 - \frac{\int^{year} \dot{q}_{RT}^{th}\, dt}{\int^{year} \dot{q}_{RT}^{opt}\, dt}} = \frac{1}{1 - \frac{\bar{q}^{th}}{\bar{q}^{opt}}} \tag{6.3}$$

where $\dot{q}^{opt}$ and $\dot{q}^{th}$ are the annual energy gains and losses, respectively. As can be seen in Fig. 6.2, the curve approaches infinity as the process scenario approaches the stagnation condition $\dot{q}^{th}/\dot{q}^{opt} = 1$. Eq. (6.3) implies that the significance of the factorization error $\varepsilon(\Delta\vartheta)$ increases rapidly with higher process temperatures.

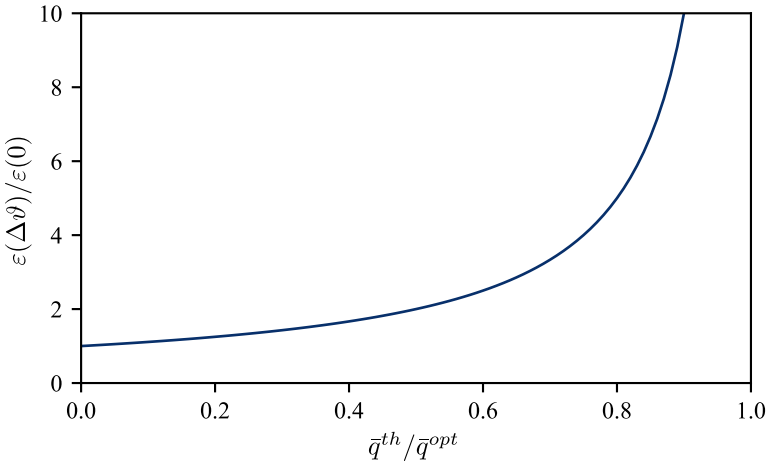

Fig. 6.2 Error development under idealized assumptions according to Eq. (6.3).

6.2.2 Realistic error development

There is an influential parameter of real operating collectors the ideal case does not take into account: the amount of working hours. Under real conditions, the useful energy output of a collector is limited to the moments when absorbed energy actually exceeds energy losses. Working hours thus represent the operating state of the collector distinguishing between operating and not operating. This effect can have positive influence on the error development and, therefore, counteract the previously described ideal scenario.

To illustrate this effect, Fig. 6.3 compares the working hours at different operating temperatures with the factorization errors for a collector at a certain location and with a pre-defined orientation. To do so, data is evaluated for each sun position vector that occurs for a defined case during the year. For example, given a certain sun position in the collector coordinate system (Fig. 6.4, left) during a summer day, the factorization error can be derived by interpolation from the IAM surfaces (Fig. 6.1), while working hours (operating state) result from evaluating the energy output equation (Eq. (6.1)) based on data taken from a weather data file. If this analysis is done not only for one single vector, but for all sun position vectors during a year, results can be presented in a contour plot. Both quantities, factorization error and working hours, are shown in polar coordinates for the entire collector hemisphere. The exemplary results were obtained for the Fresnel collector described in Section 6.3 and considering a TMY file of Seville, Spain.

The depicted factorization error is the absolute difference between the IAM values obtained by factorization and those obtained by ray-tracing (Fig. 6.1). More precisely, the upper plot in Fig 6.3 represents the average value of these differences that can be found for

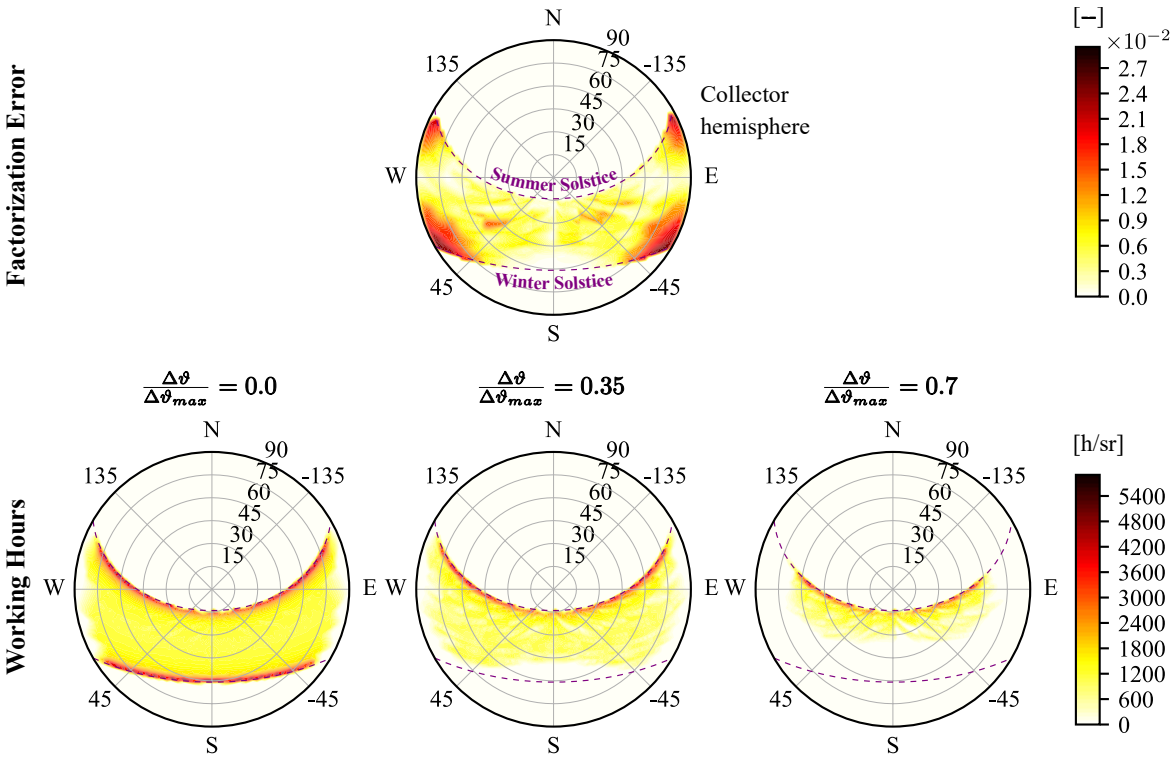

Fig. 6.3 Factorization error (top) and decreasing operating time at elevated temperatures (bottom) shown for the Fresnel collector in Fig. 5.2 and weather data of Seville.

each increment of the polar grid of the discretized collector hemisphere following Eq. (6.4)

$$\Delta\bar{K}'_b(\phi_i,\theta_{zj}) = \frac{\sum_k^T \left| K'_{b,FAC}\left(\phi(t_k),\theta_z(t_k)\right) - K'_{b,RT}\left(\phi(t_k),\theta_z(t_k)\right)\right| \delta\left(\omega(i,j)\right)}{\sum_k^T \delta\left(\omega(i,j)\right)} \tag{6.4}$$

where i and j are the computational indices of the polar grid (Fig. 6.4 (right)).

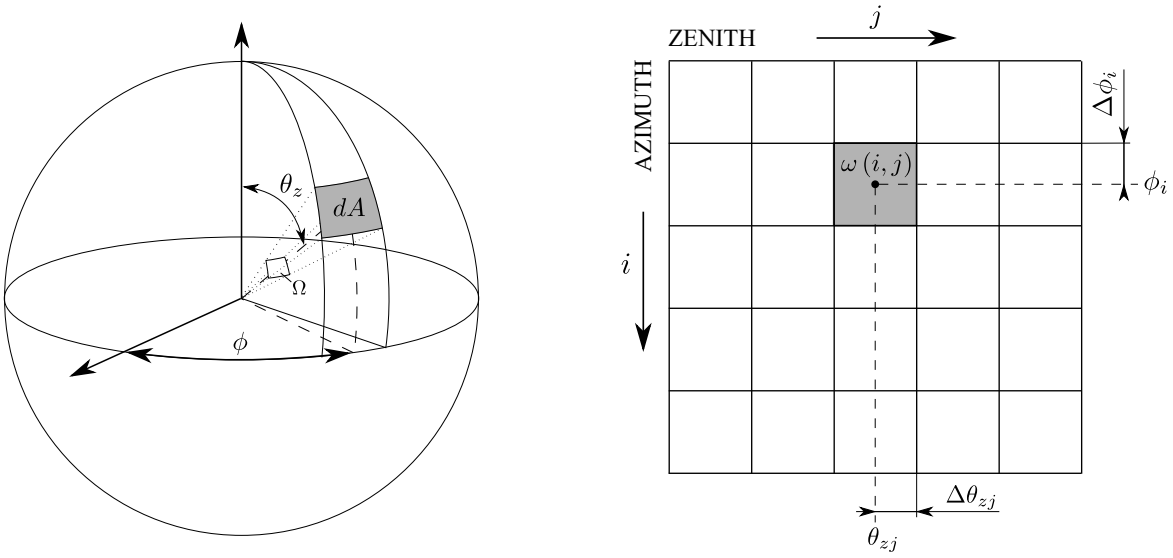

Fig. 6.4 Angle convention of spherical coordinates and the computational grid.

Each tuple (i,j) corresponds to a tuple ϕ_i, θ_{zj}, whereas initial data depend on the defined time step Δt and time vector $[t_0,t_1,\ldots,t_k,\ldots,T]$. The upper limit T of the interval marks the end of the year given the respective unit of the time step (e.g., for $\Delta t = 1h$, $T = 8760$). $\delta(\omega(i,j))$ is the Kronecker delta function for the interval $\omega(i,j)$. The interval is defined as

$$\omega(i,j) = [\phi_i \pm \Delta\phi_i] \cap [\theta_{zj} \pm \Delta\theta_{zj}] \tag{6.5}$$

where $\Delta\phi_i$ and $\Delta\theta_{zj}$ are the (i,j)-dependent increments of the azimuth and zenith angles, respectively. Given this interval, the Kronecker delta function is defined as:

$$\delta\left(\omega(i,j)\right) = \begin{cases} 1 & \text{if } \left(\phi(t_k),\theta_z(t_k)\right) \in \omega(i,j) \\ 0 & \text{if } \left(\phi(t_k),\theta_z(t_k)\right) \notin \omega(i,j) \end{cases} \tag{6.6}$$

According to Eq. (6.4), the factorization error in Fig. 6.3 is depicted as a polar surface of absolute values. Working hours, on the other hand, have been depicted as density values with

the total amount of working hours per steradian within the interval $\omega(i,j)$.

$$wh(\phi_i,\theta_{zj}) = \frac{\sum_k^T wh\,(\phi(t_k),\theta_z(t_k))\,\delta\,(\omega(i,j))}{\Omega(\phi_i,\theta_{zj})} \tag{6.7}$$

where $wh(\phi(t_k),\theta_z(t_k))$ is the number of working hours for each respective sun position. It is defined as $wh = \sigma \cdot \Delta t$, where σ takes a value of either 1 (collector is working) or 0 (collector is not working):

$$\sigma = \begin{cases} 1 & \text{if } Q^{opt} \leq Q^{th} \\ 0 & \text{if } Q^{opt} > Q^{th} \end{cases} \tag{6.8}$$

The steradian for a discrete sphere element is commonly defined as:

$$\Omega(\phi_i,\theta_{zj}) = \Delta\phi_i \left[\cos(\theta_{zj} - \Delta\theta_{zj}) - \cos(\theta_{zj} + \Delta\theta_{zj})\right] \tag{6.9}$$

The working hour distribution is shown in Fig. 6.3 for three different levels of operating temperature ratios: $\Delta\vartheta/\Delta\vartheta_{max} = 0.0$ (at ambient temperature), 0.35 (368 °C), and 0.70 (736 °C). $\Delta\vartheta_{max}$ is the highest possible temperature difference at a given location at which the collector still produces energy over a year or, in other words, the lowest temperature with zero working hours. Values are given in hours per steradian. The amount of working hours can be derived from the graph by multiplying the density values by the size of the corresponding hemispherical section in steradian. It should be noted that these dimensions in steradian are typically small, and hence, the working hour density values appear to be large. In the case of $\Delta\vartheta/\Delta\vartheta_{max} = 0.0$, the distribution corresponds to a total annual amount of 3718.38 working hours. Clearly, the operating interval of the collector shifts toward summer and noon time as the operating temperature increases. The time step for the simulation was set to $\Delta t = 1\,\text{min}$. The polar angle increments $\Delta\phi_i$ and $\Delta\theta_{zj}$ were kept constant at 1°.

To estimate the factorization error in a realistic way, the error definition from Eq. (6.2) needs to be modified to

$$\varepsilon(\Delta\vartheta) = \frac{\int^{year}(\dot{q}^{opt}_{FAC} - \dot{q}^{opt}_{RT})dt|_{WH}}{\int^{year}(\dot{q}^{opt}_{RT} - \dot{q}^{th}_{RT})dt|_{WH}} \tag{6.10}$$

where WH is the working hour condition, $\dot{q}^{opt} > \dot{q}^{th}$. Consequently, the error ratio $\varepsilon(\Delta\vartheta)/\varepsilon(0)$ cannot be simplified as shown in Eq. (6.3). This results in a more complex expression:

$$\frac{\varepsilon(\Delta\vartheta)}{\varepsilon(0)} = \underbrace{\frac{\int^{year}(\dot{q}^{opt}_{FAC} - \dot{q}^{opt}_{RT})dt|_{WH}}{\int^{year}(\dot{q}^{opt}_{FAC} - \dot{q}^{th}_{RT})dt}}_{\alpha_1} \cdot \underbrace{\frac{\int^{year}\dot{q}^{opt}_{RT}dt}{\int^{year}(\dot{q}^{opt}_{RT} - \dot{q}^{th}_{RT})dt|_{WH}}}_{\alpha_2} \tag{6.11}$$

This equation contains two meaningful parameters α_1 and α_2, which indicate different trends. They will be analysed in more detail in Section 6.4.

6.3 Test cases

Four different collector geometries were analyzed in this study: ETC [139], MaReCo [144], Fresnel collector [151], and CCStaR [1]. The geometries of these collectors are identical to those in Section 5.4. Optical and thermal properties of the MaReCo and CCStaR collectors are fully described in the Industrial Solar data sheet [151]. Detailed optics of the ETC and Fresnel collector can be found in Section 5.4. In this work, the heat loss coefficients c_1 and c_2 for the ETC and Fresnel were based on a direct flow evacuated tube collector [40] and the prototype Industrial Solar LF 11 [151], respectively. All optical and thermal properties of the collectors are summarized in Table 6.1.

Table 6.1 Optical and thermal simulation parameters of the collectors.

Model	η_{0b} [−]	η_{0d} [−]	c_1 $\left[\mathrm{W}/(\mathrm{m}^2\,\mathrm{K})\right]$	c_2 $\left[\mathrm{W}/(\mathrm{m}^2\,\mathrm{K})\right]$
ETC	0.617	0.623	0.767	0.004
MaReCo	0.690	0.560	2.400	0.0
Fresnel	0.635	-	0.000	0.00043
CCStaR	0.700	-	0.000	0.0034

Information about the solar irradiance was taken from the meteorological Energy Plus database [152]. Annual energy integration according to Eq. (6.2) was conducted for a TMY in Seville, Spain (latitude 37.42°) and Stockholm, Sweden (latitude 59.65°). The weather data source of the TMY files is Spanish Weather for Energy Calculations (SWEC) for Seville and International Weather for Energy Calculations (IWEC) for Stockholm. In addition, a specific collector orientation and tilt was assumed for each test case in order to simulate realistic process conditions. Table 6.2 gives a summary of technical and operational specifications. The collector orientation is based on the rotation coordinate system presented in Fig 5.3. It also includes the maximum operating temperature ϑ_{op} specified by the manufacturer.

Table 6.2 Technical and operational simulation parameters of the collectors.

Model	Orientation	Tilt	ϑ_{op} [°C]
ETC	EW	$\alpha_c = \phi_L$	180
MaReCo	EW	$\alpha_c = \phi_L - 30°$	75
Fresnel	NS	horizontal	200
CCStaR	NS	$\beta_c = \begin{cases} \phi_L & \text{if } \phi_L \leq 30° \\ 30° & \text{if } \phi_L > 30° \end{cases}$	200

6.4 Results and discussion

The annual energy gain for the four test cases was calculated for two different locations at the distinct latitudes of Seville and Stockholm. Incidence angles were obtained from the ray-tracing surface and factorization surface as shown in Fig. 6.1.

Fig. 6.5 depicts the error obtained by Eq. (6.11) in the case of the Fresnel collector. Coefficient α_1 slowly converges to 0 as the process temperature increases because the integration interval is constantly diminishing with fewer moments in the year satisfy the working hour condition. What is really significant, however, is the fact that the first integration points to be excluded from the integration are those with high incidence angles, where the factorization error is seemingly highest [153].

α_1 can be interpreted as a positive impact on the factorization error. Coefficient α_2, on the other hand, diverges to infinity with increasing temperature. It corresponds to the ideal error development presented in Fig. 6.2, and α_2 has a negative impact on the error. The factors α_1 and α_2 represent two temperature-dependent effects that neutralize each other. It can clearly be seen that the factorization error would increase rapidly according to α_2, but that this development is attenuated by the positive influence of the working hour condition on the factorization error, represented by α_1. As a result, the error shows a nearly constant trend until it finally increases exponentially when approaching the stagnation temperature.

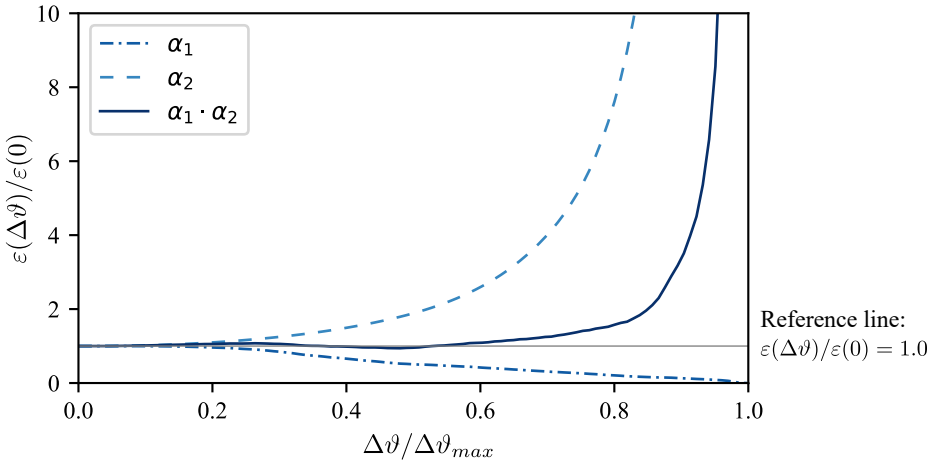

Fig. 6.5 Factorization error development; the curves of α_1 and α_2 represent the two different temperature-dependent effects that influence the trend.

Fig. 6.6 shows the results for the absolute error ratio $\left|\frac{\varepsilon(\Delta\vartheta)}{\varepsilon(0)}\right|$ based on Eq. (6.11). The errors for the test cases presented in Table 6.1 and Table 6.2 as well as the expected annual working hours are plotted. The abscissa shows the ratio of operating temperature difference to maximum temperature difference at stagnation condition $\dot{q}^{th} = \dot{q}^{opt}$, which ranges from 0 to 1.

All error curves show a much steadier trend at lower temperatures than the trend of the ideal curve shown in Fig. 6.2. The MaReCo collector shows the most continuous, less stepwise trend with larger errors in a comparably lower temperature range. This is probably due to its relatively poor optical properties. With $c_1 = 2.4$, its heat loss coefficient is more than that for the ETC, which is the second highest.

Very little difference can be observed between the two different locations. Apparently, results for Stockholm, the location at higher latitude, are slightly worse. The error begins to increase earlier, at lower temperatures. However, it is noteworthy that the working hour curve has a different shape; it is more bended compared with the results for Seville, decreasing more rapidly when the collectors are running at higher temperatures. The errors may therefore be higher at higher latitudes, but with less working hours, which make them less significant. In general, significant increase in error can only be noticed at temperatures close to the stagnation state, where the expected amount of working hours is low and the process therefore is economically not significant. With respect to a typical load profile for industrial installations, the increase in error does not possibly play an important role.

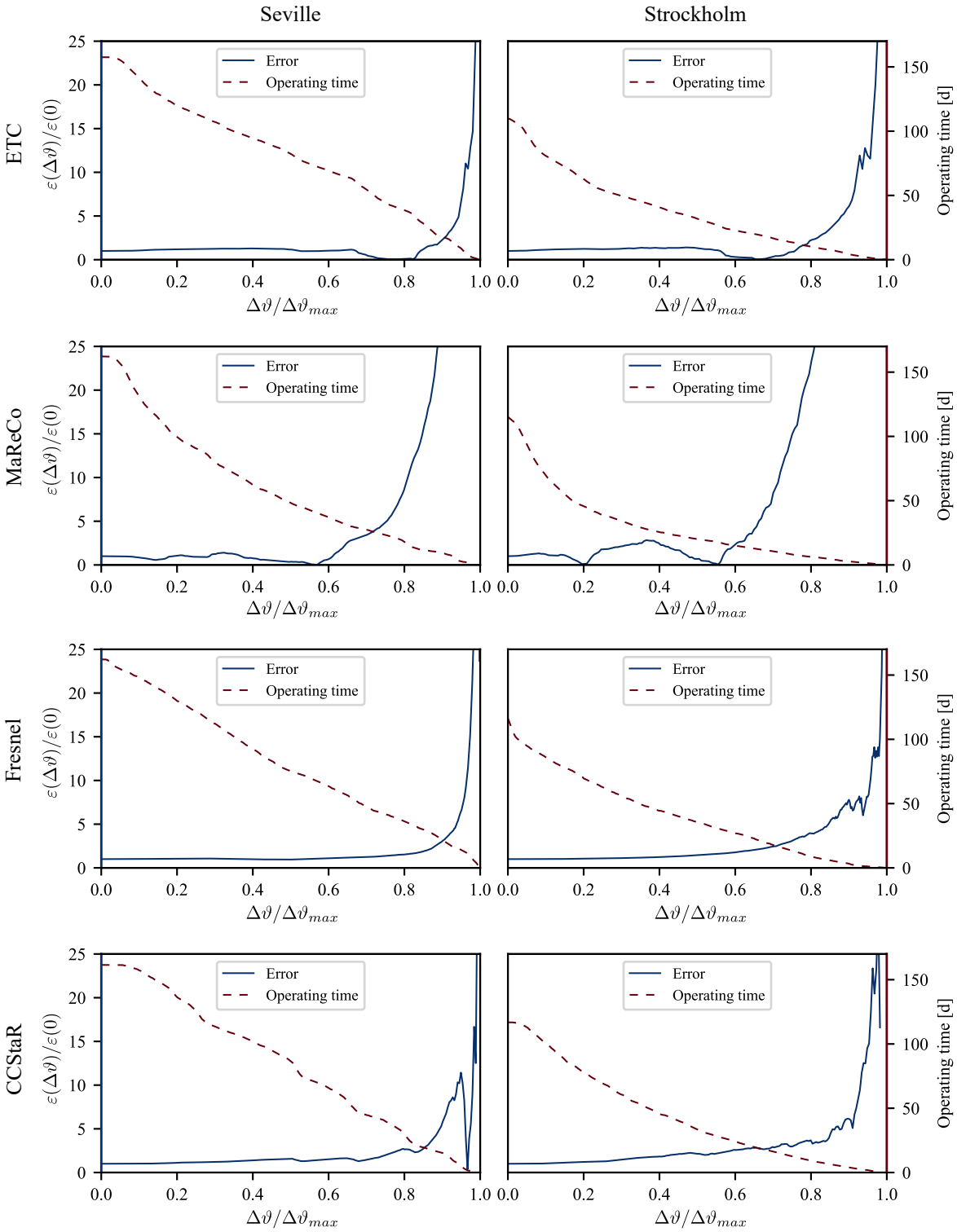

Fig. 6.6 Annually integrated factorization errors according to Eq. (6.11) and working hours for the four test cases.

Table 6.3 summarizes some key values of Fig. 6.6 for interpreting the results further. The table contains some significant temperature ratios with the maximum operating temperature difference $\Delta\vartheta_{max}$ as a reference. The ratio $\frac{\Delta\vartheta_{op}}{\Delta\vartheta_{max}}$ is compared with $\frac{\Delta\vartheta}{\Delta\vartheta_{max}}\big|_{\frac{\varepsilon(\Delta\vartheta)}{\varepsilon(0)}=2}$ and $\frac{\Delta\vartheta}{\Delta\vartheta_{max}}\big|_{\frac{\varepsilon(\Delta\vartheta)}{\varepsilon(0)}=5}$, the temperature differences where the error has doubled and quintupled, respectively. Even though a maximum operating temperature ϑ_{op} is specified by the manufacturer, for the considered test cases, all ratios are still far below the two threshold values.

Table 6.3 Comparison of operating conditions with threshold values.

Model	$\frac{\Delta\vartheta_{op}}{\Delta\vartheta_{max}}$	$\frac{\Delta\vartheta}{\Delta\vartheta_{max}}\big\|_{\frac{\varepsilon(\Delta\vartheta)}{\varepsilon(0)}=2}$	$\frac{\Delta\vartheta}{\Delta\vartheta_{max}}\big\|_{\frac{\varepsilon(\Delta\vartheta)}{\varepsilon(0)}=5}$	ϑ_{op} [°C]
		Seville		
ETC	0.57	0.89	0.94	318.66
MaReCo	0.20	0.64	0.75	370.77
Fresnel	0.19	0.86	0.94	1051.85
CCStaR	0.44	0.75	0.89	459.30
		Stockholm		
ETC	0.57	0.79	0.88	284.03
MaReCo	0.20	0.59	0.66	317.01
Fresnel	0.19	0.64	0.84	808.79
CCStaR	0.44	0.52	0.86	415.46

The results for the MaReCo collector installed in Stockholm show a notable multiplication of the pure optical error around a temperature ratio of 0.4. However, this change appears more significant than it really is, as shown in Fig. 6.7. The absolute error $\varepsilon(\Delta\vartheta)$ results take tolerable values throughout the low and medium temperature ranges.

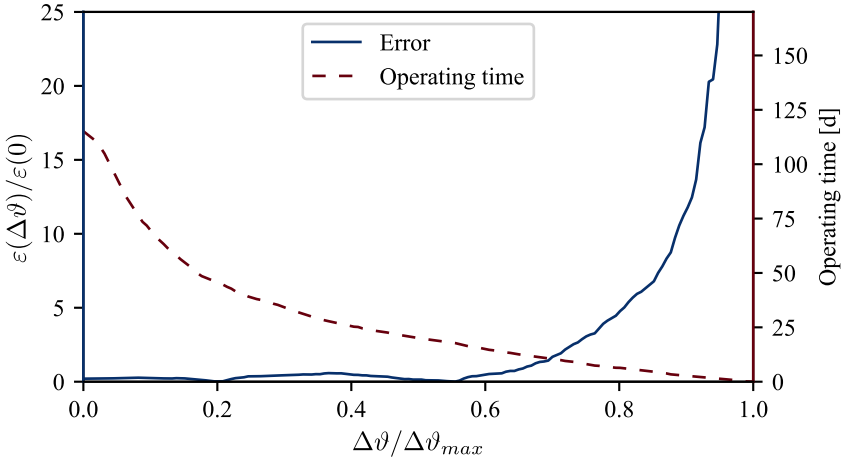

Fig. 6.7 Thermal dependency of the factorization error for MaReCo installed in Stockholm.

The significance of the factorization error also depends on the annually collected energy, since this is the denominator of Eq. (6.10). Figure 6.8 illustrates the amount of collected energy in $\mathrm{kW/m^2}$ over the relative operating temperatures of each collector for both locations Seville and Stockholm. The Fresnel and CCStaR collectors seem to have rather lower energy output values compared with those of the ETC and MaReCo collector. This is because of the following two reasons: First, the ETC and MaReCo collectors are tracked and therefore constantly face the sun in an optimal angle. Second, the chosen example of the Fresnel and CCStaR collectors are quite short and as a consequence have more end losses.

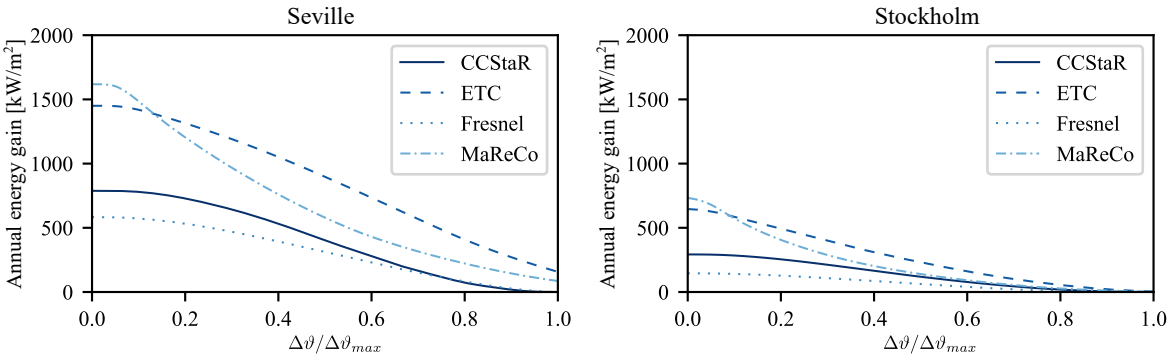

Fig. 6.8 Annually collected energy depending on the relative operating temperature of the collector.

6.5 Conclusion

Solar thermal collectors have become interesting for the use in industrial processes. Such installations run at high temperature levels, and for some collector types, there are only very few practical examples of such operation conditions. High process temperatures can lead to unknown effects on models and therefore influence energy yield predictions. In this light, the possible influence of the process temperature on the IAM factorization approach was analyzed in this study. Four test cases were considered for this purpose: ETC, MaReCo, Fresnel, and CCStaR collectors.

Two fundamental effects could be observed that govern the behavior of error curve. On the one hand, increasing thermal losses due to large process temperatures were observed to have a negative impact on the error. With the error defined as the ratio between factorization energy error and annually delivered energy due to ray-tracing, a decrease in the latter gives the factorization error more weight. On the other hand, the working hour condition was observed to have a positive impact on the error development, as fewer moments with potentially high IAM factorization errors are not taken into account. It could be concluded that within

the economically viable temperature range of each particular industrial application, the thermal process parameters do not have any significant influence on the error made by the approximation.

Chapter 7

Comparison between the experimental and the extrapolated stagnation temperature

7.1 Background

As shown in Section 1.1 most industrial processes require heat at temperatures higher than 100 °C. A significant share of such medium temperature processes could in theory be provided by well-insulated FPCs and ETCs, that so far have mostly been deployed for domestic applications. Both collector types withstand operating conditions far beyond atmospheric pressure and are therefore capable of providing process heat at temperature levels well beyond 100 °C. Stagnation temperatures of conventional FPCs are around 200 °C; those of ETC can reach even higher values, depending on their design [96].

According to the ISO 9806:2013 standard in Section 2.1, the efficiency curve of the collector is based on observations at temperature levels evenly spaced over the operating temperature range of the collector. This operating range is usually below 100 °C when operating at non-pressurized conditions. As a consequence, this approach could lead to an extrapolated area of the efficiency curve which shows larger uncertainties.

One possibility to improve the accuracy of the high temperature part of a collector's efficiency curve could be to include the stagnation temperature in the fit. The determination of the stagnation temperature forms also part of the standardized test procedure. This way, the methodology could allow improving results without any additional experimental effort.

This is meant to be a preliminary study. The feasibility of this study has been assessed by comparing both the extrapolated (not taking into account the stagnation temperature) and interpolated (taking into account the stagnation temperature) efficiency curve. To do so, three different datasets of FPCs and ETCs from two different databases have been considered. One FPC database was provided by CENER [154], the other two datasets consisting of FPC and ETC collectors were taken from the publicly available database of the Institute for Solar Technology [96]. In a second step, the extrapolated stagnation temperature has been compared with the experimentally measured stagnation temperature.

Interestingly, results showed a technology specific trend. It could be observed that the difference between measured and extrapolated stagnation temperature is constantly positive in the case of FPC collectors and constantly negative in the case of ETC collectors. To judge the accuracy of the new interpolated efficiency curve, experimental data is essential, which at this point is not available.

7.2 Methodology

Three datasets from two different databases have been evaluated. One database was provided by CENER. The database comprises 81 FPCs of different designs. Two more datasets were taken from the database of the Institute of Solar Technology in Switzerland (SPF) consisting of 24 FPCs and 23 ETCs respectively.

As for data provided by CENER, every collector was certified according to the standard regulations with eight data points at four different inlet temperatures. Apart from fitting the collector efficiency curve only to test results for the eight operational modes $\Delta\vartheta/G_T$, the stagnation temperature with its typical efficiency of zero has been included as an additional observation as well.

7.2.1 Collector efficiency curve

For this study the steady state collector model from the ISO 9806:2013 [35] has been chosen, same as presented in Eq. (2.1). To characterize the collector's efficiency behavior, η_{hem} needs to be measured at least four times, each time at a different ratio $\Delta\vartheta/G_T$. An analytical expression according to Eq. (7.1) is then obtained by determining the characteristic constants $\eta_{0,hem}$, a_1 and a_2 applying a WLS fit.

The ratio $\Delta\vartheta/G$ for different observations during the test is usually kept small to guarantee an accurate fit in temperature regions the collector will most likely be operating in. This

means, however, that for collectors that possibly operate at higher $\Delta\vartheta/G_T$-ratios, the fitted efficiency curve is not backed up by experimental data. Output predictions in this region could therefore be inaccurate. Eq. (2.1) can be rewritten to an energy output per collector area equation, when multiplying by the reference irradiance G_T.

$$\frac{Q}{A} = \eta_{0,hem} G_T - a_1 \Delta\vartheta - a_2 \Delta\vartheta^2 \tag{7.1}$$

7.2.2 Stagnation temperature

To overcome the problem of a lack of observations for higher temperatures without additional experimental effort, it may be useful to include the stagnation temperature as an additional node point in the fit. For safety reasons (risk of collector over-heating), the stagnation temperature (ϑ_{stg}) is always provided alongside other collector data. According to the ISO 9806:2013 standard, the stagnation temperature is defined as the highest temperature ϑ_{sm} that can be found on the absorber surface, while the collector is exposed to the available solar irradiance G_m and ambient temperature ϑ_{am} (outdoors, or in a solar irradiance simulator) under steady-state conditions without heat extraction from the collector (stagnation condition). To achieve these conditions with liquid heating collectors, it is recommended to drain the collector completely from all remaining heat transfer fluid and to seal all fluid pipes except for one to prevent cooling by natural circulation.

There is a standardized form of the stagnation temperature which is obtained by assuming a constant proportion of $(\vartheta_s - \vartheta_a)/G$. With the standard reference values $\vartheta_{as} = 30\,^{\circ}\mathrm{C}$ and $G_s = 1000\mathrm{W/m^2}$ according to Eq. (7.2), the standard stagnation temperature results in:

$$\vartheta_{stg} = \vartheta_{as} + \frac{G_s}{G_m}(\vartheta_{sm} - \vartheta_{am}) \tag{7.2}$$

Following these guidelines, the test demands that for FPCs the temperature sensor should be positioned at two-thirds of the absorber height and half the absorber width (Fig. 7.1), as it is supposed to be the point on the absorber surface where the temperature is highest during stagnation [35].

For ETCs the specifications are less strict. The ISO 9806:2013 states that in this case the temperature sensor should be placed at a suitable location in the collector, i.e, where the highest temperature relevant to the heat transfer fluid is to be found. Since, in the case of ETCs the absorber surface is not easily accessed, it is common practice to measure the stagnation temperature for a single tube at the tip of the pipe or copper tube respectively (Fig. 7.1).

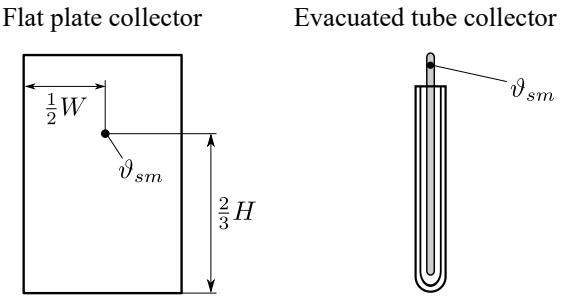

Fig. 7.1 Stagnation temperature measurement points according to the ISO 9806:2013, with W and H the width and the height of the flat plate collector respectively.

7.2.3 Data fitting

The ISO 9806:2013 standard suggests a WLS fit. Since uncertainty values of the temperature sensors were not available, a common MLR fit was applied instead of the suggested WLS method. This will not make any difference to the outcome of the study.

The collector efficiency equation of Eq. (7.1) can be converted into a multidimensional linear equation, such that it takes the form of the following general expression:

$$y_i = \beta_0 + \beta_1 x_{i,2} + \beta_2 x_{i,2} + ... + \beta_{p-1} x_{i,p-1} + \varepsilon_i \tag{7.3}$$

with y and x as the experimental parameters or observations, β as the regression coefficients and ε as the error. According to the MLR approach there exists a set of regression coefficients which minimizes the overall error $\sum_{i=1}^{n} \varepsilon_i$. This optimal coefficient vector is given by:

$$\hat{\mathbf{b}} = (\mathbf{X}^T \mathbf{X})^{-1} \mathbf{X}^T \mathbf{Y} \tag{7.4}$$

where $\mathbf{b}$ is the vector of the regression coefficients.

$$\mathbf{b} = \begin{bmatrix} \beta_0 \\ \vdots \\ \beta_p \end{bmatrix} = \begin{bmatrix} \eta_0 \\ \alpha_1 \\ \alpha_2 \end{bmatrix} \tag{7.5}$$

The design parameters which need to be determined are the optical efficiency η_0 and the thermal coefficients and α. $\mathbf{X}$ is a $n \times p$-matrix that contains the n observations for each

parameter p.

$$\mathbf{X} = \begin{bmatrix} 1 & x_{1,1} & \dots & x_{1,p-1} \\ \vdots & \vdots & \ddots & \vdots \\ 1 & x_{i,1} & \dots & x_{i,p-1} \\ \vdots & \vdots & \ddots & \vdots \\ 1 & x_{n,1} & \dots & x_{n,p-1} \end{bmatrix} = \begin{bmatrix} 1 & \frac{\Delta\vartheta_1}{G} & \frac{\Delta\vartheta_1^2}{G} \\ \vdots & \vdots & \vdots \\ 1 & \frac{\Delta\vartheta_i}{G} & \frac{\Delta\vartheta_i^2}{G} \\ \vdots & \vdots & \vdots \\ 1 & \frac{\Delta\vartheta_n}{G} & \frac{\Delta\vartheta_n^2}{G} \end{bmatrix} \tag{7.6}$$

In the case of Eq. (2.1) these parameters are the constant 1 and the experimental results for $\Delta\vartheta_1/G$ and $\Delta\vartheta_1^2/G$. $\mathbf{Y}$ is also a vector of observations containing the experimental results of the collector efficiency η.

$$\mathbf{Y} = \begin{bmatrix} y_1 \\ \vdots \\ y_i \\ \vdots \\ y_n \end{bmatrix} = \begin{bmatrix} \eta_1 \\ \vdots \\ \eta_i \\ \vdots \\ \eta_n \end{bmatrix} \tag{7.7}$$

Apart from the regular fit, the 95 %-confidence region has been calculated in order to analyze the accuracy of the fit and see how far the 8-point and 9-point fit are statistically apart. The 95 %-confidence margin of a regression parameter is defined as

$$\beta_i^{conf} = \beta_i \pm t^*_{n-p,1-\alpha/2}\sqrt{\hat{\mathbf{V}}(\mathbf{b})_{ii}} \tag{7.8}$$

with α as the confidence parameter; $\alpha = 0.05$. $t^*_{n-p,1-\alpha}$ is the t-value of the Student's t-distribution and $\hat{\mathbf{V}}(\mathbf{b})_{ii}$ are the diagonal elements of the estimated variance-covariance matrix. The variance-covariance matrix is defined as

$$\mathbf{V}(\mathbf{b}) = MSE(\mathbf{X}^T\mathbf{X})^{-1} \tag{7.9}$$

where MSE is the mean square error of the error ε_i:

$$MSE = \sum_{i=1}^{n}(\mathbf{Y} - \mathbf{X}\mathbf{b})^2 \tag{7.10}$$

7.3 Results

For the discussion in this section both efficiency curves, the 8-point fit and 9-point fit have been plotted together with the 95 %-confidence interval of the regression coefficient vector **b**.

The SPF database already provides all efficiency curve parameters as well as the measured stagnation temperature. It was therefore not necessary to apply a MLR fit and it was not possible to analyze the 95 % confidence interval of the curve. Instead, only the difference between the measured stagnation temperature and the stagnation temperature suggested by the efficiency curve were compared with each other. This comparison also forms part of the discussion of the results obtained by the CENER data evaluation.

7.3.1 CENER database

The CENER database comprises 81 FPCs of different design. The collectors were tested according to the ISO 9806:2013 standard regulations. Data therefore includes eight observations at four different temperature levels as well as the stagnation temperature. Based on this information one representative example has been chosen to compare two different efficiency curve fits with each other. One efficiency curve is based on the eight regular observations, while the other one also includes the stagnation point as an additional node point.

Fig. 7.2 shows the results for the 8-point (not including the stagnation point) and 9-point fit (including the stagnation point) of the selected collector. Besides the efficiency curves, the 95 %-confidence region is indicated by dashed lines. The confidence range was determined according to Eq. (7.8). Interestingly, the extrapolated stagnation temperature ϑ_{fit} differs significantly from the measured stagnation temperature ϑ_{stg}. In this specific example the difference $\vartheta_{stg} - \vartheta_{fit}$ is 48.5 °C.

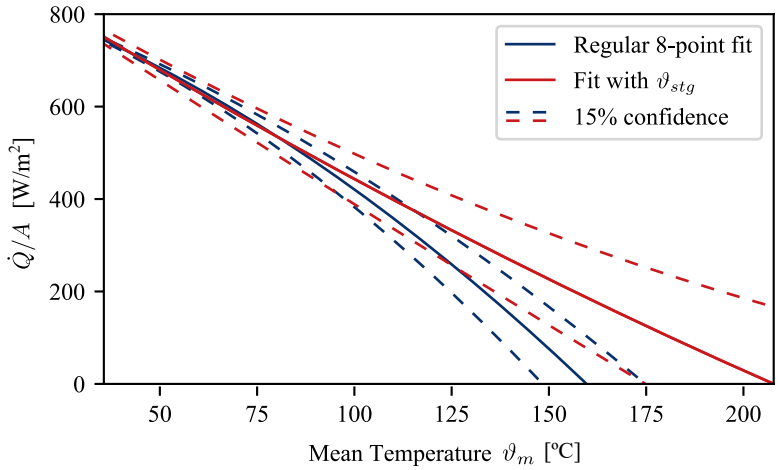

Fig. 7.2 Comparison of a regular 8-point fit with a 9-point fit that includes the stagnation temperature.

The 95 %-confidence margin also indicates that the difference between both values is too large as to be explained by statistical accuracy of the fit. ϑ_{stg} lies far outside the 95 %-

confidence region. In some parts an overlap can be observed between the 95 %-confidence uncertainty margins of both curves. At this stage of research it is not possible to say which of the two curves represents the real collector behavior better. What should be noted regarding the 9-point fit is a less-realistic shape of the curve. It shows a reversed curvature to the one obtained by the regular collector efficiency behavior. The most probable solution to the real collector efficiency curve is somewhere in-between the two presented curves. In order to validate the suggested 9-point fit it is essential to obtain observations for the medium and high temperature range.

Fig 7.3 shows the distribution of temperature differences $\vartheta_{stg} - \vartheta_{fit}$ as they were found for all collectors of the database. Extrapolated stagnation temperature ϑ_{fit} from the 8-point fit is constantly underestimating the measured one. While the average gap is 39.47 °C in one case it even reaches 83 °C.

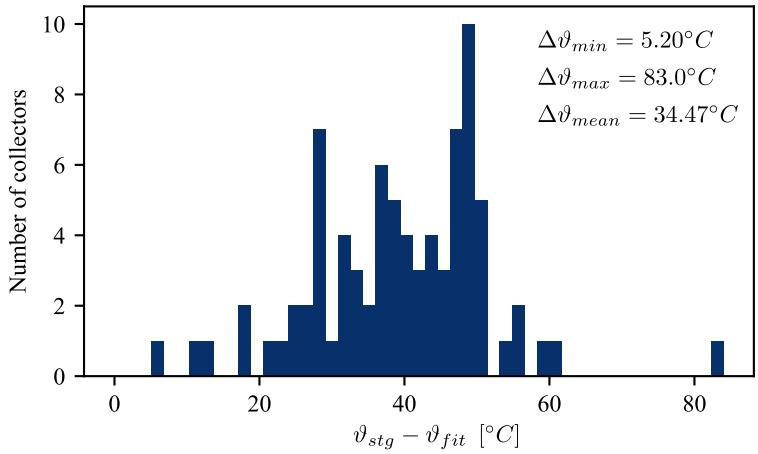

Fig. 7.3 Distribution of the difference between the actually measured stagnation temperature ϑ_{stg} and the estimated stagnation temperature ϑ_{fit} - based on data from CENER.

7.3.2 SPF database

SPF provides an extensive, publicly available database of test results of FPCs and ETCs. Two sets from this database have been evaluated in this study. The datasets consist of 24 FPCs and 23 ETCs respectively.

As can be seen in Fig 7.4, results for FPCs show almost constantly positive temperature differences $\vartheta_{stg} - \vartheta_{fit}$, same as was reported for the CENER database. The maximum temperature difference is 26.30 °C . However, in three cases the measured stagnation temperature seems to be well represented by the extrapolated one.

As an interesting fact, it could be shown that in the case of ETCs the gap $\vartheta_{stg} - \vartheta_{fit}$ is negative in most of the cases. The extrapolated value is consequently overestimating the measured stagnation temperature. A very large difference of $-159.74\,°C$ could be found in two cases. It should be noted that one of the reasons for this negative temperature difference could be the way in which the stagnation temperature is measured for ETCs. Since it is often complicated to attach temperature sensors to the absorber surface inside the evacuated tube, the sensor is placed at the head of the tube. Taking into consideration the temperature gradient along the tube as a result of heat transport mechanisms, a lower temperature can be expected at the tip of the tube than further down towards the bottom.

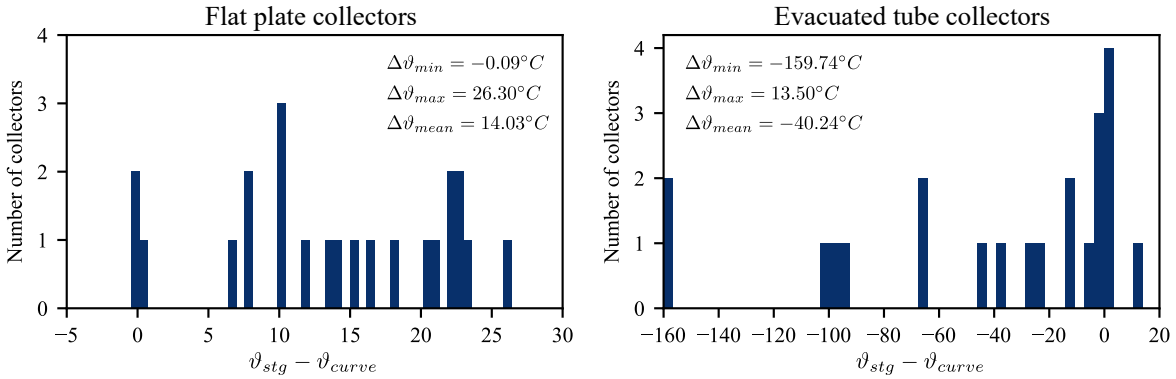

Fig. 7.4 Absolute distribution of the difference between the actually measured stagnation temperature ϑ_{stg} and the estimated stagnation temperature ϑ_{fit} - based on data from CENER.

7.4 Conclusion

The conventional data fitting approach according to the ISO 9806:2013 standard constantly underestimates the actual stagnation temperature in the case of FPCs and overestimates it in the case of ETCs. The reason for these differences is most likely due to the way the stagnation temperature is measured. Stagnation temperature assessment methods differ for every type of technology. In addition, the accuracy of the measured stagnation temperature might depend on a couple of other effects such as the temperature dependency of optical properties and non-linear effects of convectional heat transfer.

An exemplary sample from the CENER database showed that since ϑ_{stg} was found outside the 95 %-confidence interval of the fit; in this case statistical errors of the prediction could be excluded. In some parts an overlap was observed between the 95 %-confidence uncertainty margins of both curves. Whether a 9-point fit could yield more accurate results within the high temperature range of the efficiency curve is not straight forward to say. It

would be necessary to validate this approach with experimental data at higher operating temperatures.

Chapter 8

Conclusion and outlook

For many years, solar thermal collectors have provided heat for households and other smaller facilities. The industrial sector, however, despite its high potential for integration of solar heat, is still untapped. This potential and the specific requirements in an industrial setting gave rise to the development of many new collector technologies which are now competing with each other for market penetration. It is necessary to update leading performance testing standards accordingly in order to accommodate all possible collector designs and thereby provide a common basis of comparison.

In essence, this dissertation conducts four studies scrutinizing possible limitations of the current quasi-dynamic testing procedure, which is still primarily applicable to conventional low-temperature solar collectors. Shortcomings have been found when dealing with the optical characterization of collectors, especially for those with complex biaxial IAM characteristics. It is important to be aware of the different definitions and methods to apply the commonly used factorization; otherwise, the approach could lead to unexpectedly high errors in the predicted optical performance. The question has been raised whether IAM factorization is an appropriate approach in general, or whether it would be more accurate to include ray-tracing analyses in the testing procedure. For this purpose, a short study has been carried out to try to pinpoint the most important features of a ray-tracing code.

The thermal characterization of solar collectors has also been briefly touched on. An evaluation of efficiency curve results provided by two testing laboratories has revealed the necessity to extend testing to higher temperature ranges.

8.1 Summary and implications

The principle objective of this thesis was to learn whether the standardized collector performance testing procedure (recommended by ISO 9806) still holds for solar process heat collectors.

Especially when dealing with concentrating collectors, the most critical part of the performance assessment is expected to be the optical characterization. A powerful ray-tracing code has been developed, building on the previous in-house software, OTSun. What makes this code special is that it is able to import information about more complex surface reflectance patterns, allowing the modeling of advanced surface structures such as those of thin-film treated materials. Coated surfaces are not only prevalent in solar thermal materials but have also become common practice.

The developed ray-tracing code with its many implemented functions has been used to carry out a parameter sensitivity analysis. The analysis has led to a number of conclusions. First, a complete spectral analysis is not necessary, as using solar-weighted parameters yields sufficiently accurate results. Second, the angle dependency of the surface reflectance is very important. Even though it seems obvious, the surface reflectance curve is not always provided by the manufacturer, and cannot be included by most ray-tracing software. Third, as already indicated by the study of Osório et al. [105], ray-tracing results seem to be most sensitive to the way the refractive material is modeled. As a final conclusion, it should be mentioned that, in general, open source ray-tracing software often lacks the ability to import more accurate material data, such as complex reflectance and scattering patterns, incidence angle dependent reflectance, or coating compositions.

When dealing with collectors with biaxial IAM characteristics, which is not unusual among solar process collectors, ISO 9806:2013 dictates the use of the IAM factorization approach. What has passed unnoticed so far is that there exist different ways to apply this approach. This dissertation is the first study to examine this issue by applying the factorization for different collector designs, with different reference irradiance, and in different angle spaces. The factorization error has been depicted in an intuitive and praxis-related manner by plotting it over the latitude of the installation. What could be concluded from the results is that the factorization in the θ_i-θ_T angle space, in general, yields better results. This is because it better represents end and cosine losses. The factorization could also be applied to θ_L-θ_T space, but experience is required in order not to misrepresent end losses. At the moment, the current standard does not mention this pitfall of different IAM factorization definitions.

Related to this topic is the thermal dependency of the factorization error. As a purely optical effect, it could have been expected that the factorization error gains in importance at higher temperatures of operation. This, however, is not the case. It could be shown that the relative annually integrated factorization error is indeed increasing with higher process temperatures, but is not doing so before reaching a temperature range which is actually not relevant for practical cases.

What distinguishes solar process collectors from conventional ones is that they usually operate at higher temperatures. This can bring about challenges to the thermal characterization of such collectors. Although the standard mentions the necessity to construct the collector efficiency curve by means of observations for temperatures over the entire operating range of the collector, hardly any literature can be found on such high-temperature measurements. An exception to this is the study of Hess [99]. This thesis evaluated conventional low-temperature measurement data of two renowned certification laboratories: CENER and SPF. By analyzing the difference between the extrapolated and measured stagnation temperature, an indicator has been established for the misrepresentation of the mid- to high-temperature range of the efficiency curve. While a series of high-temperature measurements are still missing to validate the results of this work, it could be shown that the extrapolated area of the second term efficiency curve quickly becomes unreliable if not supported by high-temperature observations.

8.2 Suggestions for future research

Chapter 2 showed that the efficiency of solar thermal collectors (Eqs. (2.1) and (2.2)) can strongly depend on the incidence angle of the collector aperture. This sensibility regarding the incidence angle is mainly due to optical effects and is included in the incidence angle modifier. In practice, it can be very difficult or impossible to determine the IAM factor for all possible angles of incidence. The McIntire model (Eq. (2.8)) reduces this effort significantly but is still far from solving all testing problems.

One issue might be the orientation of the collector to ensure a possible range of incidence angles from 0 to 90° during the measurement period. In a laboratory setting, for example, this would require an adjustable measurement platform. Depending on the collector size, it can be difficult and expensive to provide such a platform. On the other hand, for field measurements, no matter the type or dimension of the collector, there are always incidence angle regions on the collector hemisphere that are not covered over the course of the year. This is an issue which has been completely unaddressed by ISO 9806. So far, the only existing method that

successfully conducted QDT under in-situ conditions is an iterative procedure proposed by [42].

Regardless of the practical issues, it is questionable whether the existing incidence angle modifier functions actually constitute an accurate optical model of the collector. This is especially true for the simplified factorization model. Using the factorization approach, the entire IAM surface is constructed from a limited set of experimental observations along the collector symmetry planes. Consequently, the accuracy of any arbitrary IAM value of this surface is subject to both interpolation errors and errors introduced by the simplified assumption of factorization. Alternatively, a ray-tracing simulation of the collector not only represents a much more complex optical model but also provides a comprehensive set of physically meaningful design parameters[1] to adjust this model to the experimental observations. Figure 8.1 shows a possible procedure to include ray-tracing simulations in the current collector testing procedure.

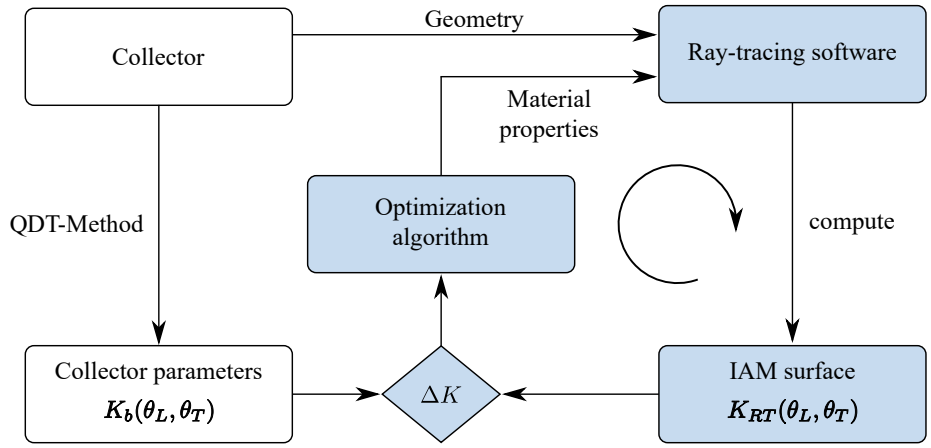

Fig. 8.1 A possible procedure to include ray-tracing simulations in the current collector testing procedure.

This method has been presented and included in the official agenda of Task 57 and its possible succeeding task. One of the principle challenges will be to create a ray-tracing optical model which is generic enough to mirror the optical characteristics of most collectors, but not so generic that it causes an overfit and excessive computation time. The parametric reflectance functions presented in Chapter 3.2.3 will present a good starting point. Furthermore, the discussion on IAM factorization in Chapter 5 will provide a good basis for this type of study.

Finally, the ray-tracing program presented in Section 3 will also be developed further. This work will be continued within the framework of the OTSun project [103]. Possible candidates for implementation are those optical models shown in gray in Table 3.2

[1] Transparency, absorptivity, reflectivity, specularity, mirror shape, alignment errors etc.

References

[1] F. Sallaberry, R. Pujol-Nadal, V. Martínez-Moll, and J.-L. Torres, "Optical and thermal characterization procedure for a variable geometry concentrator: A standard approach," Renewable Energy **68**, 842–852 (2014).

[2] S. Kalogirou, "The potential of solar industrial process heat applications," Applied Energy **76**, 337–361 (2003).

[3] A. K. Sharma, C. Sharma, S. C. Mullick, and T. C. Kandpal, "Solar industrial process heating : A review," **78**, 124–137 (2017).

[4] S. H. Farjana, N. Huda, M. A. P. Mahmud, and R. Saidur, "Solar process heat in industrial systems – A global review," Renewable and Sustainable Energy Reviews **82**, 2270–2286 (2018).

[5] Solar Payback, "SOLAR HEAT FOR INDUSTRY," http://www.solrico.com/fileadmin/solrico/media/doc/Solar_payback/Solar_Heat_for_Industry_Solar_Payback_April_2017.pdf (2017).

[6] IRENA, "Renewable Energy Options for the Industry Sector: Global and Regional Potential until 2030," http://www.irena.org/-/media/Files/IRENA/Agency/Publication/2014/Aug/IRENA_RE_Potential_for_Industry_BP_2015.pdf?la=en&hash=F9B495F78DB624BC6A546F15D90C216FDE09DBAD, Tech. rep. (2015).

[7] IEA, "Technology Roadmap: Solar Heating and Cooling," https://www.iea.org/publications/freepublications/publication/Solar_Heating_Cooling_Roadmap_2012_WEB.pdf, Tech. rep. (2012).

[8] S. A. Kalogirou, *Solar Energy Engineering: Processes and Systems* (Academic Press, 2013), 2nd ed.

[9] H. Schweiger, J. F. Mendes, N. Benz, K. Hennecke, G. Prieto, M. Cusí, and H. Gonçalves, "The potential of solar heat in industrial processes. A state of the art review for Spain and Portugal," in "Proceedings of the EuroSun 2000 Conference," (Kopenhagen, 2000).

[10] C. Lauterbach, "Potential , system analysis and preliminary design of low-temperature solar process heat systems," Ph.D. thesis, University of Kassel (2014).

[11] E. Frank, S. Hess, and C. Zahler, "IEA Task 49 Deliverable A 1.1: General requirements and relevant parameters for process heat collectors and specific collector loop components," http://task49.iea-shc.org/Data/Sites/1/publications/Deliverable_A1-1_v07.pdf, Tech. rep., SPF (2012).

[12] IEA, "Key world energy statistics," https://www.iea.org/publications/freepublications/publication/KeyWorld2017.pdf (2017).

[13] IEA, "Key world energy statistics," www.iea.org/statistics/ (2016).

[14] V. van de Pol and L. Wattimena, "Onderzoek naar het potentieel van zonthermische energie in de industrie," Tech. rep., Bedrijfsadviseurs B.V. (2001).

[15] P. Kovacs and H. Quicklun, "Solenergi i industriell processvärme—Enförstudie av svenska möjligheter, SP Rapport 2003," Tech. rep., SP, Boras, Sweden (2003).

[16] T. Müller, H. Schnitzer, C. Brunner, U. Begander, and O. Themel, "Produzieren mit Sonnenenergie: Potenzialstudie zur thermischen Solarenergienutzung in österreichischen Gewerbe- und Industriebetrieben," Tech. rep., Bundesministerium für Verkehr, Innovation und Technologie, Wien, Austria (2004).

[17] C. Vannoni, R. Battisti, and S. Drigo, "Potential for Solar Heat in Industrial Processes. Report within IEA SHC Task 33/IV," Tech. rep., Rome, Italy (2008).

[18] C. Lauterbach, B. Schmitt, U. Jordan, and K. Vajen, "The potential of solar heat for industrial processes in Germany," Renewable and Sustainable Energy Reviews **16**, 5121–5130 (2012).

[19] W. Platzer, B. Schmitt, C. Lauterbach, S. Hess, and P. Delmas, "IEA Task 49 Deliverable C 5: Potential studies on solar process heat worldwide," http://task49.iea-shc.org/Data/Sites/1/publications/151031_IEA_Task49_Deliverable_C5_Potential%20studies.pdf, Tech. rep. (2015).

[20] APPSOL, "WP1: APLICACIÓN Y POTENCIAL, CARACTERIZACIÓN INDUSTRIA, Rseumen Ejecutivo," http://appsol.cl/wp-content/uploads/2018/04/APPSOL.WP1_.-Caracterizacio%CC%81n-Industria.pdf, Tech. rep. (2014).

[21] S. Hoffmann, K. Kogler, and I. Krofak, "Market study of Solar Thermal Energy for Industrial / Commercial Use in Pakistan, Egypt and Morocco," http://www.solarthermalworld.org/sites/gstec/files/news/file/2015-02-27/ifc_study_executive_summary.pdf, Tech. rep., International Financ. Corp. (IFC) (2014).

[22] IRENA, "Solar Heat for Industrial Processes, Technology Brief E21," https://www.solarthermalworld.org/sites/gstec/files/news/file/2015-02-27/irena-solar-heat-for-industrial-processes_2015.pdf, Tech. Rep. January (2015).

[23] E. Taibi, D. Gielen, and M. Bazilian, "The potential for renewable energy in industrial applications," Renewable and Sustainable Energy Reviews **16**, 735–744 (2012).

[24] UNIDO, "Renewable Energy in Industrial Applications - An assessment of the 2050 potential," https://www.solarthermalworld.org/sites/gstec/files/unido_renewables_industrial_applications.pdf, Tech. rep. (2011).

[25] IEA, *Energy Technology Perspectives 2012* (2012).

[26] AEE INTEC, "Task 49 SHIP database," http://ship-plants.info/ (2015).

[27] IEA SHC, "Task 49 - Solar Heat Integration in Industrial Processes," http://task49.iea-shc.org/ (2017).

[28] F. Mauthner, W. Weiss, and M. Spörk-Dür, "Solar Heat Worldwide - Markets and Contribution to the Energy Supply 2014," http://www.iea-shc.org/data/sites/1/publications/solar-heat-worldwide-2016.pdf, Tech. rep. (2016).

[29] W. Weiss and F. Mauthner, "Solar Heat Worldwide: Markets and Contribuition to the Energy Supply 2012," Tech. rep., AEE Intec, Gleisdorf (2014).

[30] A. Eisentraut and A. Brown, "IEA Report: Heating without global warming - Market Developments and Policy Considerations for Renewable Heat," https://www.iea.org/publications/freepublications/publication/FeaturedInsight_HeatingWithoutGlobalWarming_FINAL.pdf, Tech. rep., IEA (2014).

[31] SolRico, "Solar Thermal Process Heat: Surprisingly popular," http://www.solrico.com/fileadmin/solrico/media/doc/Sun___Wind_Energy_Article/SWE_world_map_article_January_2017.pdf (2017).

[32] S. Fahr, K. Kramer, P. Delmas, A. Heimsath, A. Fernández-García, L. Valenzuela, F. Sallaberry, A. Hofer, D. W. van Rooyen, S. Mehnert, T. Osório, and P. Horta, "IEA Task 49 Deliverable A 3.1: Guideline on testing procedures for collectors used in solar process heat," http://task49.iea-shc.org/Data/Sites/1/publications/160519_IEA_Task_49_D3_1.pdf, Tech. Rep. May (2015).

[33] CEN, "EN 12975-2. Thermal solar systems and components – Solar collectors – Part 2: Test methods. European Committee for Standardisation." (2006).

[34] ANSI/ASHRAE, "ASHRAE Standard 93 Methods of Testing to Determine Thermal Performance of Solar Collectors." (2003).

[35] ISO, "ISO 9806: International Standard Solar energy — Solar thermal collectors — Test methods," (2013).

[36] IEA, "Task 57 - Solar Standards and Certification," http://task57.iea-shc.org/.

[37] S. Fischer, W. Heidemann, and H. Müller-Steinhagen, "Collector parameter identification - Iterative methods versus multiple linear regression," in "Proceedings of the ISES Solar World Congress 2003," (International Solar Energy Society (ISES), Göteborg, Sweden, 2003).

[38] J. A. Duffie and W. A. Beckman, *Solar Engineering of Thermal Processes* (WILEY, 2013), 4th ed.

[39] A. Hofer, L. Valenzuela, N. Janotte, J. I. Burgaleta, J. Arraiza, M. Montecchi, F. Sallaberry, T. Osório, J. Carvalho, F. Alberti, K. Kramer, and A. Heimsath, "State of the Art of Performance Evaluation Methods for Concentrating Solar Collectors," in "21th Solar Power And Chemical Energy Systems International Symposium," (2015).

[40] T. Osório and M. J. Carvalho, "Testing of solar thermal collectors under transient conditions," Solar Energy **104**, 71–81 (2014).

[41] S. Fischer, W. Heidemann, H. Müller-Steinhagen, B. Perers, P. Bergquist, and B. Hellström, "Collector test method under quasi-dynamic conditions according to the European Standard EN 12975-2," Solar Energy **76**, 117–123 (2004).

[42] A. Hofer, D. Büchner, K. Kramer, S. Fahr, A. Heimsath, W. Platzer, and S. Scholl, "Comparison of Two Different (Quasi-) Dynamic Testing Methods for the Performance Evaluation of a Linear Fresnel Process Heat Collector," Energy Procedia **69**, 84–95 (2015).

[43] W. Kong, Z. Wang, J. Fan, P. Bacher, B. Perers, Z. Chen, and S. Furbo, "An improved dynamic test method for solar collectors," Solar Energy **86**, 1838–1848 (2012).

[44] L. Xu, Z. Wang, G. Yuan, X. Li, and Y. Ruan, "A new dynamic test method for thermal performance of all-glass evacuated solar air collectors," Solar Energy **86**, 1222–1231 (2012).

[45] C. Wittwer, W. Hube, P. Schossig, A. Wagner, C. Kettner, M. Mertins, and K. Rittenhofer, "ColSim- A new simulation environment for complex system analysis and controllers," in "Proceedings of the 7th IBPSA Conference," (Rio de Janeiro, 2001).

[46] S. Fischer, P. Frey, and H. Drück, "A comparison between state-of-the-art and neural network modelling of solar collectors," Solar Energy **86**, 3268–3277 (2012).

[47] A. Neumann, A. Witzke, S. A. Jones, and G. Schmitt, "Representative Terrestrial Solar Brightness Profiles," Journal of Solar Energy Engineering **124**, 198–204 (2002).

[48] A. Souka and H. Safwat, "Optimum orientations for the double exposure flat-plate collectors and its reflectors." Solar Energy **10**, 170 (1966).

[49] W. R. McIntire, "Factored approximations for biaxial incident angle modifiers," Solar Energy **29**, 315–322 (1982).

[50] Schott, "Optical Glass - Data Sheets," https : / / www . schott . com / d / advanced _ optics / ac85c64c-60a0-4113-a9df-23ee1be20428 / 1 . 3 / schott-optical-glass-collection-datasheets-english-17012017 . pdf, Tech. rep. (2014).

[51] R. Bader, A. Pedretti, and A. Steinfeld, "A 9-m-aperture solar parabolic trough concentrator based on a multilayer polymer mirror membrane mounted on a concrete structure," Journal of Solar Energy Engineering **133**, 031016 (2011).

[52] R. French, J. Rodríguez-Parada, M. Yang, R. Derryberry, and N. Pfeiffenberger, "Optical properties of polymeric materials for concentrator photovoltaic systems," Solar Energy Materials and Solar Cells **95**, 2077–2086 (2011).

[53] M. Köhl, M. G. Meir, P. Papillon, G. M. Wallner, and S. Saile, *Polymeric Materials for Solar Thermal Applications* (Wiley-VCH, 2012).

[54] N. Selvakumar and H. C. Barshilia, "Review of physical vapor deposited (PVD) spectrally selective coatings for mid- and high-temperature solar thermal applications," Solar Energy Materials and Solar Cells **98**, 1–23 (2012).

[55] H. A. Macleod, *Thin-Film Optical Filters* (CRC Press, 2010), 4th ed.

[56] J. Choi, K. Han, and J. H. Kim, "Enhanced near infrared reflectance of TiO2/SiO2/TiO2 multilayer structure using a base-catalyzed SiO2 film," Thin Solid Films **569**, 100–103 (2014).

[57] S.-H. Jeong, J.-K. Kim, B.-S. Kim, S.-H. Shim, and B.-T. Lee, "Characterization of SiO2 and TiO2 films prepared using rf magnetron sputtering and their application to anti-reflection coating," Vacuum **76**, 507–515 (2004).

[58] F. Sutter, S. Ziegler, M. Schmücker, P. Heller, and R. Pitz-Paal, "Modelling of optical durability of enhanced aluminum solar reflectors," Solar Energy Materials and Solar Cells **107**, 37–45 (2012).

[59] M. Mazur, D. Wojcieszak, D. Kaczmarek, J. Domaradzki, S. Song, D. Gibson, F. Placido, P. Mazur, M. Kalisz, and A. Poniedzialek, "Functional photocatalytically active and scratch resistant antireflective coating based on TiO2 and SiO2," Applied Surface Science **380**, 165–171 (2015).

[60] C. Atkinson, C. L. Sansom, H. J. Almond, and C. P. Shaw, "Coatings for concentrating solar systems – A review," Renewable and Sustainable Energy Reviews **45**, 113–122 (2015).

[61] R. Prado, G. Beobide, A. Marcaide, J. Goikoetxea, and A. Aranzabe, "Development of multifunctional sol-gel coatings: Anti-reflection coatings with enhanced self-cleaning capacity," Solar Energy Materials and Solar Cells **94**, 1081–1088 (2010).

[62] F. Sutter, P. Heller, S. Meyen, R. Pitz-paal, C. E. Kennedy, A. Fernández-garcía, M. Schmücker, A. Fernández, P. Heller, A. Fernández García, P. Heller, C. E. Kennedy, S. Meyen, R. Pitz-paal, and M. Schmücker, "A new method to characterize degradation of first surface aluminum reflectors," Proceedings of the SolarPACES 2010 Conference pp. 1–8 (2010).

[63] C. Xin, C. Peng, Y. Xu, and J. Wu, "A novel route to prepare weather resistant, durable antireflective films for solar glass," Solar Energy **93**, 121–126 (2013).

[64] A. Soum-Glaude, I. Bousquet, L. Thomas, and G. Flamant, "Optical modeling of multilayered coatings based on SiC(N)H materials for their potential use as high-temperature solar selective absorbers," Solar Energy Materials and Solar Cells **117**, 315–323 (2013).

[65] L. An, S. T. Ali, T. Søndergaard, J. Nørgaard, Y. C. Tsao, and K. Pedersen, "Optimization of TiAlN/TiAlON/Si3N4 solar absorber coatings," Solar Energy **118**, 410–418 (2015).

[66] H. C. Barshilia, N. Selvakumar, K. S. Rajam, and A. Biswas, "Optical properties and thermal stability of TiAlN/AlON tandem absorber prepared by reactive DC/RF magnetron sputtering," Solar Energy Materials and Solar Cells **92**, 1425–1433 (2008).

[67] L. Rebouta, A. Pitães, M. Andritschky, P. Capela, M. F. Cerqueira, A. Matilainen, and K. Pischow, "Optical characterization of TiAlN/TiAlON/SiO 2 absorber for solar selective applications," Surface and Coatings Technology **211**, 41–44 (2012).

[68] D. Hernández-Pinilla, A. Rodríguez-Palomo, L. Álvarez-Fraga, E. Céspedes, J. Prieto, A. Muñoz-Martín, and C. Prieto, "MoSi2–Si3N4 absorber for high temperature solar selective coating," Solar Energy Materials and Solar Cells **152**, 141–146 (2016).

[69] C. Prahl, B. Stanicki, C. Hilgert, S. Ulmer, and M. Ro, "Airborne shape measurement of parabolic trough collector fields," Solar Energy **91**, 68–78 (2013).

[70] S. A. Jones, J. K. Gruetzner, R. M. Houser, R. M. Edgar, and T. J. Wendelin, "VSHOT measurement uncertainty and experimental sensitivity study," (1997).

[71] S. Ulmer, B. Heinz, K. Pottler, and E. Lüpfert, "Slope Error Measurements of Parabolic Troughs Using the Reflected Image of the Absorber Tube," Journal of Solar Energy Engineering **131**, 11014 (2009).

[72] Skyfuel Inc., "ReflecTech Mirror Film Brochure," http://www.skyfuel.com/wp-content/uploads/Brochure-SF-ReflecTech_EN.pdf, Tech. rep. (2017).

[73] Almeco Group, "Vega Energy Brochure," http://www.almecogroup.com/uploads/5922-ALMECO_vegaEnergy_ENG_S302_01_2015-mail.pdf, Tech. rep. (2015).

[74] S. Meyen, M. Montecchi, C. Kennedy, G. Zhu, M. Gray, J. Crawford, and S. Hiemer, "Guidelines: parameters and method to evaluate the solar reflectance properties of reflector materials for concentrating solar power technology," in "Proceedings of the SolarPACES Conference," (2013), June.

[75] M. Montecchi, "Approximated method for modelling hemispherical reflectance and evaluating near-specular reflectance of CSP mirrors," Solar Energy **92**, 280–287 (2013).

[76] P. Good, T. Cooper, M. Querci, N. Wiik, G. Ambrosetti, and A. Steinfeld, "Spectral reflectance, transmittance, and angular scattering of materials for solar concentrators," Solar Energy Materials and Solar Cells **144**, 509–522 (2015).

[77] A. Heimsath, T. Schmid, and P. Nitz, "Angle Resolved Specular Reflectance Measured with VLABS," in "Energy Procedia," , vol. 69 (Elsevier B.V., 2015), vol. 69, pp. 1895–1903.

[78] R. B. Pettit, "Characterization of the reflected beam profile of solar mirror materials," Solar Energy **19**, 733–741 (1977).

[79] R. Gee, R. Brost, G. Zhu, and G. Jorgensen, "An improved method for characterizing reflector specularity for Parabolic Trough Concentrators," in "Proceedings of the SolarPACES Conference," (Perpignan (France), 2010), p. 2124.

[80] F. Sutter, S. Meyen, A. Fernández-García, and P. Heller, "Spectral characterization of specular reflectance of solar mirrors," Solar Energy Materials and Solar Cells **145**, 248–254 (2016).

[81] T. Tesfamichael and E. Wäckelgård, "Angular solar absorptance of absorbers used in solar thermal collectors," Appl. Opt. **38**, 4189–4197 (1999).

[82] Á. Moreno, J. Marín-Sáez, A. Riverola, D. Chemisana, J. Atencia, and M. V. Collados, "Holographic photovoltaic-thermal module for window louvre integration: Design and simulation," Proceedings of the EuroSun 2016 Conference pp. 11–14 (2016).

[83] Breault Research Organization, "ASAP," http://www.breault.com/software/asap-nextgen.

[84] Opticad Cooperation, "OptiCAD," http://www.opticad.com/.

[85] Fraunhofer ISE, "RayTrace3D," https://www.ise.fraunhofer.de/en.html.

[86] ENEA, "SimulTrough," http://www.solaritaly.enea.it/StrSimulTrough/SimulTroughIn.php.

[87] T. Wendelin, "SolTRACE: A New Optical Modeling Tool for Concentrating Solar Optics," Solar Energy pp. 253–260 (2003).

[88] R. Buck, "Solar Power Raytracing Tool, SPRAY, User Manual. Version 2.6, 20.3.2010. Technical report, DLR," Tech. rep. (2010).

[89] J. M. Blanco, M. J. Amieva, and A. Mancilla, "The Tonatiuh software development project: An open source approach to the simulation of solar concentrating systems," (ASME International Mechanical Engineering Congress and Exposition, Florida USA, 2005).

[90] LAMBDA, "TracePro," https://www.lambdares.com/.

[91] V. Martínez, R. Pujol, and A. Moià, "Assessment of Medium Temperature Collectors for Process Heat," Energy Procedia **30**, 745–754 (2012).

[92] CEN, "Solar Keymark," http://www.estif.org/solarkeymarknew/ (2018).

[93] RISE - Research Institutes of Sweden, "ScenoCalc," http://www.sp.se/en/index/services/solar/ScenoCalc/Sidor/default.aspx (2018).

[94] RISE, "Research Institutes of Sweden," https://www.sp.se/en/Sidor/default.aspx.

[95] ICC-SRCC, "Solar Rating and Certification Corporation," http://www.solar-rating.org/.

[96] SPF, "Institute for Solar Technology," http://www.spf.ch/Home.44.0.html?&L=6 (2015).

[97] NREL, "SAM - System Advisor Model," https://sam.nrel.gov/.

[98] S. Hess and B. Schmitt, "IEA Task 49 Deliverable C 4: "Best practice " Series of Case Study Reports from Demonstration Projects," http://task49.iea-shc.org/Data/Sites/1/publications/IEA_Task49_Deliverable_C4_Best%20Practice-final-160528.pdf, Tech. rep. (2016).

[99] S. Hess, "Low-Concentrating, Stationary Solar Thermal Collector for Process Heat Generation," Ph.D. thesis, Freiburg (2014).

[100] R. Pujol-Nadal and V. Martinez-Moll, "Optical Analysis of the Fixed Mirror Solar Concentrator by Forward Ray-Tracing Procedure," Journal of Solar Energy Engineering **134**, 031009 (2012).

[101] R. Pujol-Nadal, "Optical characterization of a fixed mirror solar concentrator prototype by the ray- tracing procedure," Journal of Renewable and Sustainable Energy **6**, 1–14 (2014).

[102] R. Pujol-Nadal, V. Martínez-Moll, F. Sallaberry, and A. Moià-Pol, "Optical and thermal characterization of a variable geometry concentrator using ray-tracing tools and experimental data," Applied Energy **155**, 110–119 (2015).

[103] R. Pujol-Nadal, V. Martínez-Moll, A. Moià-Pol, G. Cardona, J. D. Hertel, and F. Bonnin, "OTSun Project: Development of a Computational Tool for High-resolution Optical Analysis of Solar Collectors," in "Proceedings of the EuroSun 2016 Conference," (Palma de Mallorca, Spain, 2016).

[104] Wikipedia, "STL (file format)," https://en.wikipedia.org/wiki/STL_(file_format).

[105] T. Osório, P. Horta, M. Larcher, R. Pujol-Nada, J. Hertel, and D. W. Van Rooyen, "Ray-tracing software comparison for linear focusing solar collectors," AIP Conference Proceedings **1734**, 020017 (2016).

[106] F. Abelés, "Recherches sur la propagation des ondes électromagnétiques sinoïdales dans les milieurs stratifiés. Applications aux couches minces," Annales de Physique **12**, 596–640 (1950).

[107] N. Sahouane and A. Zerga, "Optimization of antireflection multilayer for industrial crystalline silicon solar cells," Energy Procedia **44**, 118–125 (2014).

[108] S. Saylan, T. Milakovich, S. A. Hadi, A. Nayfeh, E. A. Fitzgerald, and M. S. Dahlem, "Multilayer antireflection coating design for GaAs0.69P0.31/Si dual-junction solar cells," Solar Energy **122**, 76–86 (2015).

[109] U. Sikder and M. A. Zaman, "Optimization of multilayer antireflection coating for photovoltaic applications," Optics and Laser Technology **79**, 88–94 (2016).

[110] J. F. Cardenas, "Modelling the spectral selective solar absorption properties of graphite-silica composite/aluminium structures," Thin Solid Films **586**, 76–81 (2015).

[111] R. Yang, J. Liu, L. Lin, Y. Qu, W. Zheng, and F. Lai, "Optical properties and thermal stability of colored solar selective absorbing coatings with double-layer antireflection coatings," Solar Energy **125**, 453–459 (2016).

[112] R. Grena, "Optical simulation of a parabolic solar trough collector," International Journal of Sustainable Energy **29**, 19–36 (2010).

[113] C. Schlick, "An Inexpensive BRDF Model for Physically - based Rendering," Computer Graphics Forum **13**, 233–246 (1994).

[114] I. Lazányi and L. Szirmay-Kalos, "Fresnel Term Approximations for Metals," in "Proceedings of the WSCG 2005," (Plzen, Czech Repbulic, 2005), pp. 77–80.

[115] NREL, "Reference Solar Spectral Irradiance: Air Mass 1.5," https://www.nrel.gov/grid/solar-resource/spectra-am1.5.html (2016).

[116] T. Wendelin, A. Lewandowski, and A. Dobos, "SolTrace - Manual," (2017).

[117] R. Montes and C. Ureña, "An Overview of BRDF Models," http://digibug.ugr.es/bitstream/handle/10481/19751/rmontes_LSI-2012-001TR.pdf?sequence=1&isAllowed=y, Tech. rep. (2012).

[118] SolarPACES, "Solar Paces Guideline: Parameters and Method to Evaluate the Solar Reflectance Properties of Reflector Materials for Concentrating Solar Power Technology, VERSION 2.5," Tech. rep. (2013).

[119] J. C. Stover, *Optical Scattering: Measurement and Analysis* (SPIE Press, 2012), 3rd ed.

[120] M. Montecchi, "Proposal of a new parameter for the comprehensive qualification of solar mirrors for CSP Applications," in "AIP Conference Proceedings," (2016), p. 130014.

[121] Q. Cai, H. Ye, and Q. Lin, "Analysis of the optical and thermal properties of transparent insulating materials containing gas bubbles," Applied Thermal Engineering **100**, 468–477 (2016).

[122] G. M. Wallner, W. Platzer, and R. W. Lang, "Structure-property correlations of polymeric films for transparent insulation wall applications. Part 1: Solar optical properties," Solar Energy **79**, 583–592 (2005).

[123] P. Good, T. Cooper, M. Querci, N. Wiik, G. Ambrosetti, and A. Steinfeld, "Spectral reflectance, transmittance, and angular scattering of materials for solar concentrators," Data in Brief **6**, 184–188 (2015).

[124] R. Pujol-Nadal, "Comportamiento Óptico y Térmico de un Concentrador Solar Lineal con Re ector Estacionario y Foco Móvil," Ph.D. thesis, Universitat de les Illes Balears (2012).

[125] D. Buie, C. J. Dey, and S. Bosi, "The effective size of the solar cone for solar concentrating systems," Solar Energy **74**, 417–427 (2003).

[126] C. J. Winter, R. L. Sitzmann, and L. L. Vant-Hull, *Solar power plants* (Springer Verlag, 1991).

[127] S. El Alj, A. Al Mers, O. Merroun, A. Bouatem, N. Boutammachte, H. Ajdad, S. Benyakhlef, and Y. Filali Baba, "Optical Modeling and Analysis of the First Moroccan Linear Fresnel Solar Collector Prototype," Journal of Solar Energy Engineering **139**, 41009–41012 (2017).

[128] X. Li, M. Lin, Y. Dai, and C.-H. Wang, "Comparison-Based Optical Assessment of Hyperboloid and Ellipsoid Reflectors in a Beam-Down Solar Tower System With Linear Fresnel Heliostats," Journal of Solar Energy Engineering **139**, 61003–61014 (2017).

[129] R. Pujol Nadal and V. Martínez Moll, "Optical analysis of a curved-slats fixed-mirror solar concentrator by a forward ray-tracing procedure." Applied optics **52**, 7389–98 (2013).

[130] D. Chester, P. Bermel, J. D. Joannopoulos, M. Soljacic, and I. Celanovic, "Design and global optimization of high-efficiency solar thermal systems with tungsten cermets," Optics Express **19**, A245–A257 (2011).

[131] J. D. Hertel, V. Martínez-Moll, R. Pujol-Nadal, and F. Bonnín, "State of the art of radiation-matter interaction models applied for the optical characterization of concentrating solar collectors," in "Proceedings of the EuroSun 2016 Conference," (Palma de Mallorca, 2016).

[132] P. Horta and T. Osório, "Optical Characterization Parameters for Line-focusing Solar Concentrators: Measurement Procedures and Extended Simulation Results," in "Energy Procedia," , vol. 49 (Elsevier Ltd, 2014), vol. 49, pp. 98–108.

[133] G. Zhu and A. Lewandowski, "A New Optical Evaluation Approach for Parabolic Trough Collectors: First-Principle OPTical Intercept Calculation," Journal of Solar Energy Engineering **134**, 041005 (2012).

[134] G. Zhu, "Development of an analytical optical method for linear Fresnel collectors," Solar Energy **94**, 240–252 (2013).

[135] Filmetrics, "Refractive indices database," http : / / www . filmetrics . com / refractive-index-database (2017).

[136] RefractiveIndex, "Refractive indices database," http://refractiveindex.info/?shelf=main&book=Al&page=Rakic (2017).

[137] G. Zhu, "Development of an analytical optical method for linear fresnel collectors," Solar Energy **94**, 240–252 (2013).

[138] A. Heimsath, P. Lindner, E. Klimm, T. Schmid, K. O. Moreno, Y. Elon, M. Am-Shallem, and P. Nitz, "Specular reflectance of soiled glass mirrors - Study on the impact of incidence angles," AIP Conference Proceedings **1734** (2016).

[139] M. Rönnelid, B. Perers, and B. Karlsson, "On the factorisation of incidence angle modifiers for CPC collectors," Solar Energy **59**, 281–286 (1997).

[140] M. Mertins, "Technische und wirtschaftliche Analyse von horizontalen Fresnel-Kollektoren," Ph.D. thesis, University of Karlsruhe (TH) (2009).

[141] R. Bernhard, S. Hein, J. de LaLaing, M. Eck, M. Eickhoff, M. Pfänder, G. Morin, and A. Häberle, "Linear Fresnel Collector Demonstration on the PSA Part II - Commissioning and First Performance Tests," (2008).

[142] G. Morin, J. Dersch, W. Platzer, M. Eck, and A. Häberle, "Comparison of Linear Fresnel and Parabolic Trough Collector power plants," Solar Energy **86**, 1–12 (2012).

[143] A. Helgesson, *Optical Characterization of Solar Collectors from Outdoor Measurements Incidence Angle Dependence of Asymmetric Collectors* (2004).

[144] M. Adsten, a. Helgesson, and B. Karlsson, "Evaluation of CPC-collector designs for stand-alone, roof- or wall installation," Solar Energy **79**, 638–647 (2005).

[145] R. Pujol-Nadal, V. Martínez-Moll, and A. Moià-Pol, "Parametric Analysis of the Fixed Mirror Solar Concentrator for Medium Temperature Applications," Journal of Solar Energy Engineering **136**, 011025 (2013).

[146] VariCAD, "VariCAD," https://www.varicad.com/en/home/.

[147] T. Tesfamichael and E. Wäckelgård, "Angular Solar Absorptance and Incident Angle Modifier of Selective Absorbers for Solar Thermal Collectors," Solar Energy **68**, 335–341 (2000).

[148] F. Sallaberry, R. Pujol-Nadal, A. García-de Jalón, and V. Martínez-Moll, "Toward a standard testing methodology for solar thermal collectors with variable-geometry: The direct radiation incidence angle modifier issue," Solar Energy **121**, 31–40 (2015).

[149] A. Meinel and M. Mainel, *Applied Solar Energy, An Introduction* (Addison-Wesley, 1976).

[150] F. Karsten and A. T. Young, "Revised Optical Air-Mass Tables and Approximation Formula," Applied Optics **28**, 4735–4738 (1989).

[151] Industrial Solar, "Industrial Solar linear Fresnel collector LF-11, Technical Data Sheet," http://www.industrial-solar.de/CMS/fileadmin/user_upload/IS_Technical_Data_EN.pdf (2015).

[152] DOE - U.S. Department of Energy, "Energy Plus Weather Database," https://energyplus.net/weather (2015).

[153] J. D. Hertel, V. Martínez-Moll, and R. Pujol-Nadal, "Estimation of the Influence of Different Incidence Angle Modifier Models on the Biaxial Factorization Approach," Energy Conversion and Management **106**, 249–259 (2015).

[154] CENER, "National Renewable Energy Centre, Spain (CENER)," http://www.cener.com/en/ (2015).

Appendix A

Multi-layer glass model

Duffie and Beckman provided an equation to calculated the transparency of a glazing with multiple covers [38].

$$\tau = \frac{1}{2}\left[\frac{1-r_{\parallel}}{1+(2N-1)r_{\parallel}} + \frac{1-r_{\perp}}{1+(2N-1)r_{\perp}}\right] \tag{A.1}$$

where N is the number of glass covers. Eq. A.1 was shown to yield different results from ray-tracing simulations. These differences are increasing with the number of covers taken into account. A self-developed analytical expression for the transmittance is provided. Here, the transmittance for s-polarized radiation is given as

$$\begin{aligned}\tau_{\perp} =&(1-r_{\perp})^{k} \\ &\left(\sum_{n=0}^{\infty}[1+n(k-2)]r_{\perp}^{2n} + \sum_{m=3}^{k}\sum_{n=0}^{\infty}[1+n(k-m)](1-r_{\perp})^{2(m-2)(n+1)}r_{\perp}^{2(n+1)}\right)\end{aligned} \tag{A.2}$$

while the transmittance for p-polarized radiation is

$$\begin{aligned}\tau_{\parallel} =&(1-r_{\parallel})^{k} \\ &\left(\sum_{n=0}^{\infty}[1+n(k-2)]r_{\parallel}^{2n} + \sum_{m=3}^{k}\sum_{n=0}^{\infty}[1+n(k-m)](1-r_{\parallel})^{2(m-2)(n+1)}r_{\parallel}^{2(n+1)}\right)\end{aligned} \tag{A.3}$$

To solve these equations for a case of a multi-layered glass with k interfaces it is helpful to recall the solutions of the following geometric series

$$\sum_{n=0}^{\infty} r^{2n} = \frac{1}{1-r^2} \tag{A.4}$$

and

$$\sum_{n=0}^{\infty} n r^{2n} = \left(\frac{r}{1-r^2} \right)^2 \tag{A.5}$$

Thus, the total transmittance is the mean of both results

$$\tau = \frac{1}{2} \left(\tau_{\perp} + \tau_{\parallel} \right) \tag{A.6}$$

Eqs. (A.2) and (A.3) follows the principle of Fig. A.1.

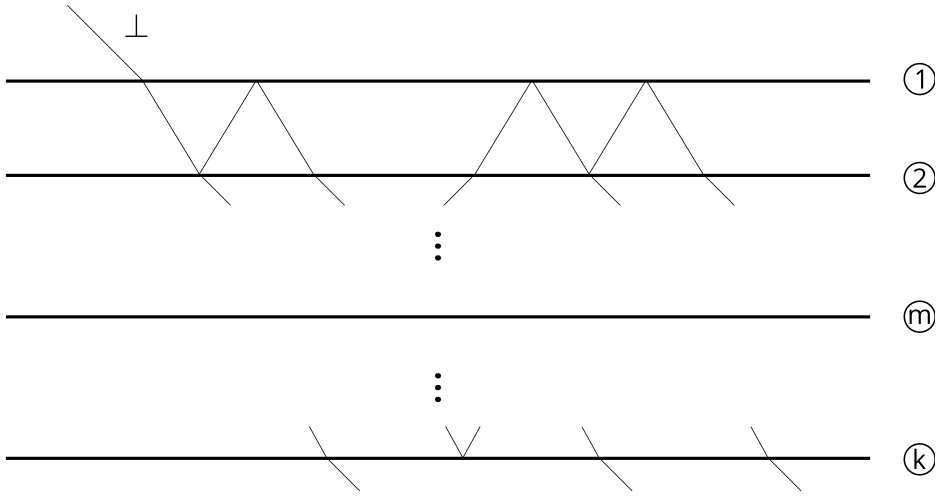

Fig. A.1 k-interfaces scheme.

Fig. A.2 represents the simulated values of the transmittance over the angle of incidence for covers with an increasing number of glass layers.

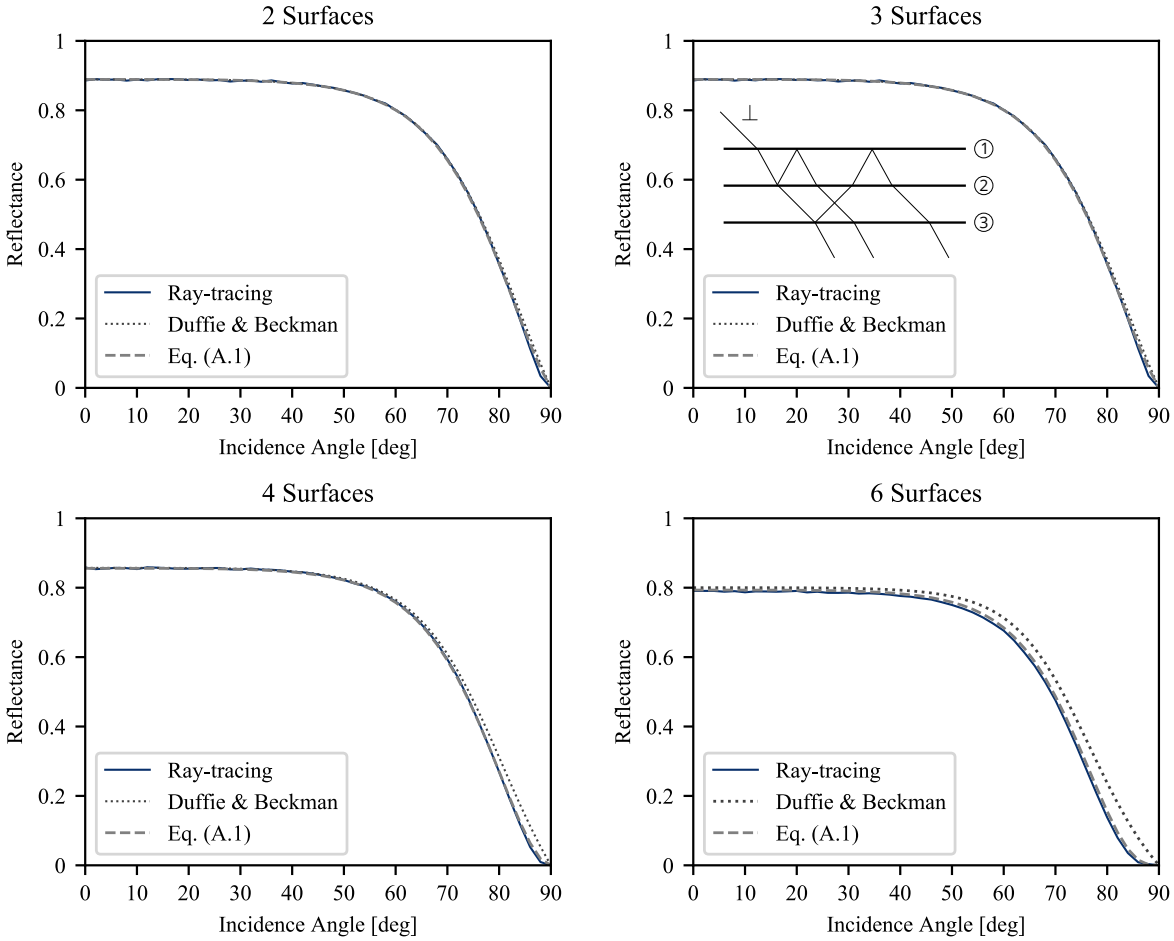

Fig. A.2 The transmittance of a covers with an increasing number of layers

Appendix B

Implementation of Gaussian scattering

From the source code point of view Eq. (3.26) has been implemented using the law of total probability.

$$Pr(A) = \sum_n Pr(A|B_n)Pr(B_n) \tag{B.1}$$

where $Pr(B_n)$ is the probability of event B_n and $Pr(A|B_n)$ is the conditional probability of event A given B_n. If we set up a case with two random variables X and Y Eq. (B.1) simplifies to

$$Pr(X \leq x) = Pr(X \leq x|Y \leq y)Pr(Y \leq y) + Pr(X \leq x|Y > y)P(Y > y) \tag{B.2}$$

or when expressed with cumulative distribution functions as common for Monte-Carlo algorithms the following equation is obtained

$$Pr(X \leq x) = F_1(x)p_1 + F_2(x)p_2 \tag{B.3}$$

Comparing this correlation of probabilities to the Gaussian scattering profile (Eq. (3.26)), the partitions p_1 and p_2 can be interpreted as K and $(1-K)$ respectively and the the probability density functions $F_1(x)$ and F_2 are the Gaussian distributions with respect to σ_2 and σ_1 respectively. The correlation of Eq. (B.3) has been illustrated in Fig. B.1

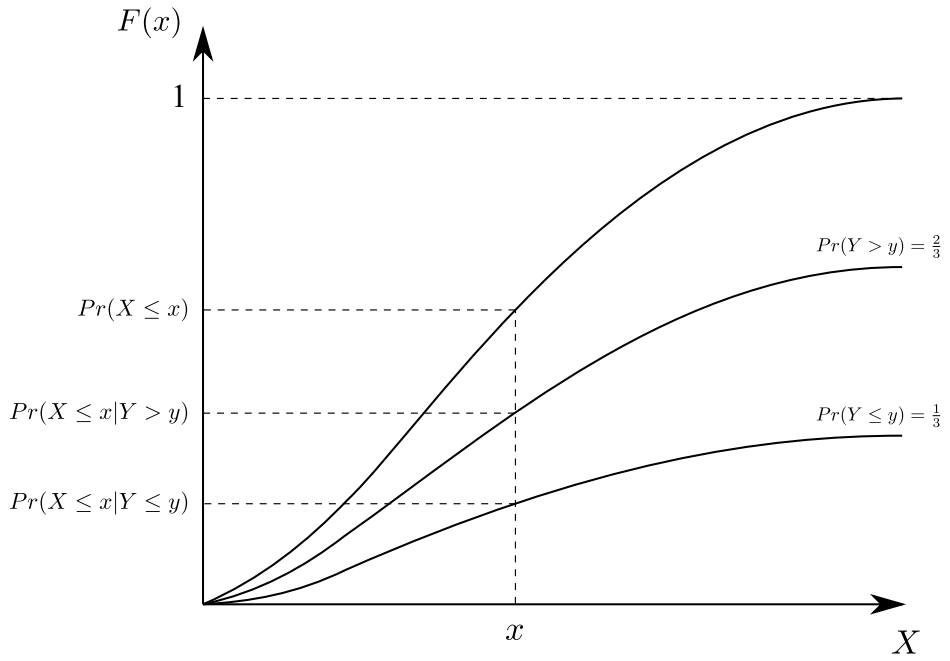

Fig. B.1 Law of total probability

In the end, the double Gaussian distribution can be reproduced in a Monte-Carlo manner using three random variables *ran1*, *ran2* and *ran3* within the interval $[0,1]$. *ran1* one defines the scattering angle ϕ distributed according to the Gaussian curves and *ran2* defines the azimuth angle of the reflected ray, which is evenly distributed. *ran3* defines the energy share *K*.

```
*       White data (Box-Mueller-Transform)
        ran1      = aleatori(sem)
        ran2      = aleatori(sem)
        ran3      = aleatori(sem)
        R         = sqrt(-2*log(ran1))
        th_dist   = 2*pi*ran2
        th_x_ran  = R*cos(th_dist)
        th_y_ran  = R*sin(th_dist)

*       transform random data
        if (ran3.gt.K) then
           th_x = sigma11*cos(phi_roll)*th_x_ran -
     +            sigma12*sin(phi_roll)*th_y_ran
           th_y = sigma11*sin(phi_roll)*th_x_ran +
```

```
+            sigma12*cos(phi_roll)*th_y_ran
  else
     th_x = sigma21*cos(phi_roll)*th_x_ran -
+            sigma22*sin(phi_roll)*th_y_ran
     th_y = sigma21*sin(phi_roll)*th_x_ran +
+            sigma22*cos(phi_roll)*th_y_ran
  endif
```

The validation of this approach is shown in Fig. B.2 which compares the analytical model with the cumulative distribution produced by ray-tracing simulations. Some demonstrations

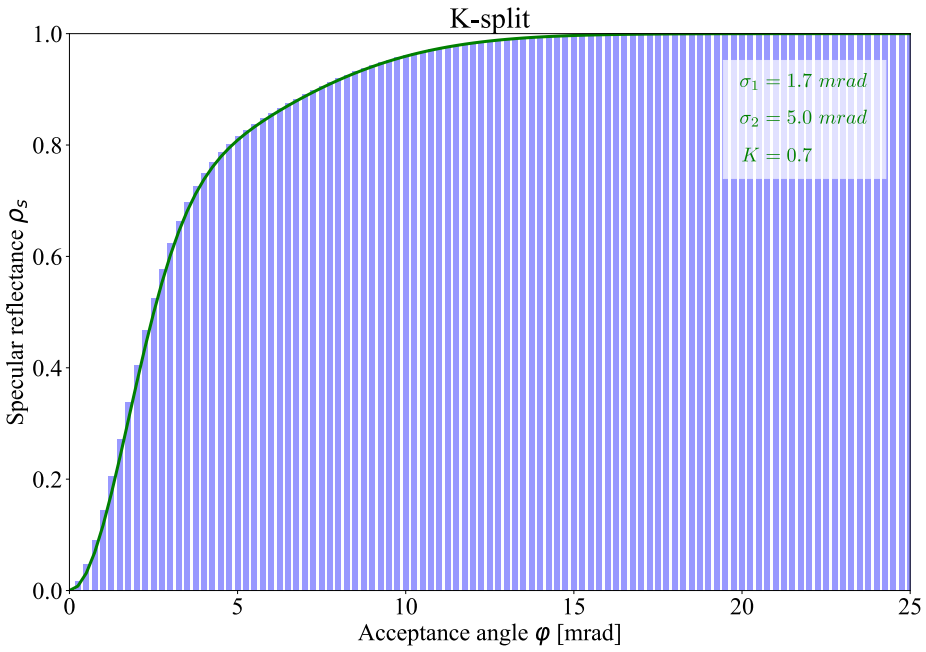

Fig. B.2 Validation of the Gaussian scattering function. Green: analytical scattering function. Blue: histogram of generated ray directions.

for different scattering settings are shown in Fig. B.3.

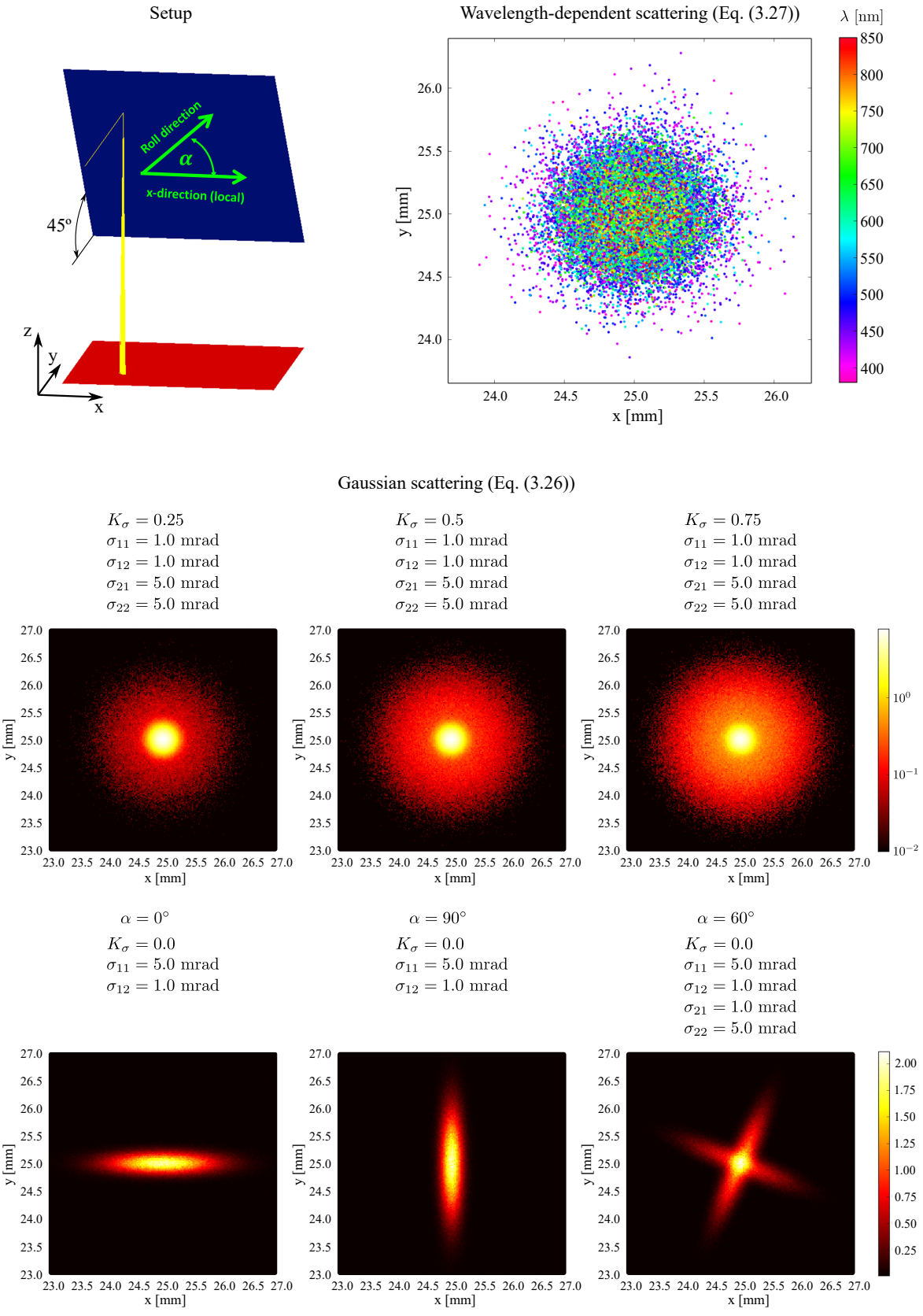

Fig. B.3 Visualization of different scattering models implemented in OTSun.

Appendix C

Angle space conventions

Fig. C.1 illustrates different angles, which define the sun vector in the collector coordinate system.

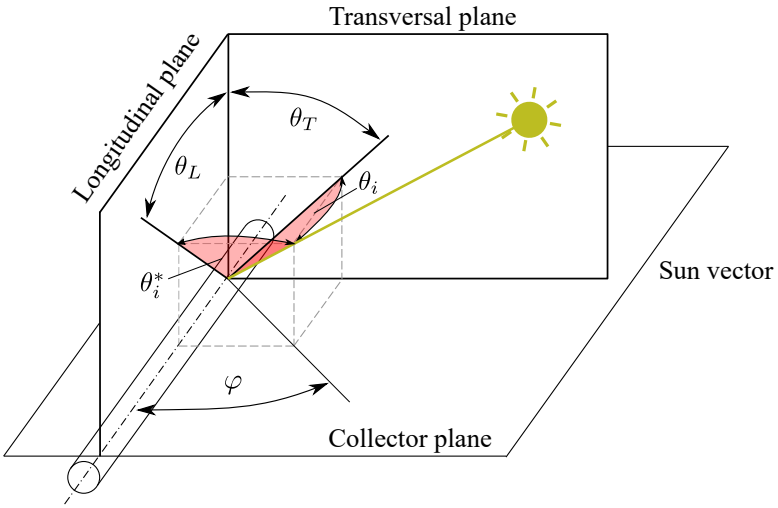

Fig. C.1 Different angle definitions for biaxial collector geometries.

The following list of equations summarizes some formula which relate different spaces of angle.

$$\tan\theta_T = \tan\theta\sin\varphi \tag{C.1}$$

$$\tan\theta_L = \tan\theta\cos\varphi \tag{C.2}$$

$$\tan^2\theta = \tan^2\theta_T + \tan^2\theta_L \tag{C.3}$$

$$\sin\theta_i = \sin\theta\cos\varphi \tag{C.4}$$

$$\sin\theta_i^* = \sin\theta\sin\varphi \tag{C.5}$$

$$\tan\theta_i = \tan\theta_L\cos\theta_T \tag{C.6}$$

$$\cos\theta = \cos\theta_i\cos\theta_T \tag{C.7}$$

$$\sin\theta_i^* = \cos\theta_i\sin\theta_T \tag{C.8}$$

$$\sin^2\theta = \sin^2\theta_i + \sin^2\theta_i^* \tag{C.9}$$